# UNIVERSITÀ DEGLI STUDI DI TRENTO

## FACOLTÀ DI SCIENZE MATEMATICHE FISICHE E NATURALI

Dottorato di Ricerca in Fisica, 28 ciclo

**Fabrication and characterization of Phosphate-based planar waveguides activated by Er$^{3+}$ ions**

Promoter:

Dr. Maurizio Ferrari

Dr. Alessandro Chiasera

Candidata:

Iustyna Vasilchenko

ANNO ACADEMICO 2015-2016

*To my family*

*In loving memory of my grandfather*

# Acknowledgements

# Content

# List of acronyms

AFM *Atomic Force Microscopy*

APTE *Addition de photons par transferts d'energie*

ARS *Angle-resolved scattering*

CRT *Cathode ray tube*

CW *Continuous wave*

DC *Direct current*

DMF *Dimethylformamide*

EDFA *Erbium Doped Fiber Amplifier*

EXAFS *Extended X-Ray Absorption Fine Structure*

FDC *Fast decay component*

FHD *Flame hydrolysis deposition*

FLN *Fluorescence line narrowing*

HT *Heat treatment*

IR *Infrared*

LITD *Laser-induced damage threshold*

LMCT *Ligand-to-metal charge transfers*

MCVD *Modified chemical vapor deposition*

MIR *Mid infrared*

MLS *M-line spectroscopy*

MFP *Mean free path*

MPTS *3-methacryloxypropyltrimethoxysilane*

MWMLS *Multiwavelength M-line spectroscopy*

PECVD *Plasma-enhanced chemical vapor deposition*

PG *Parent glass*

PIQ *Pair-induced quenching*

PL *Photoluminescence*

PP *Phosphorous precursor*

ppm *Parts per million*

PZT *Lead Zirconate Titanate*

R *Reflectance*

RE *Rare earth*

RF *Radio frequency*

SDC *Slow decay component*

SEM  *Scanning Electron Microscope*

SZM *Structure zone model*

T *Transmittance*

TE *Transverse electric polarization*

TM *Transverse magnetic polarization*

TS *Total scattering*

WKB *Wentzel-Kramer-Brilloin*

# Introduction

It's well recognized that phosphate glasses fabricated by melting possess good chemical durability, excellent optical properties, ion exchangeability and fiber-shaping ability. The fantastic review article of Prof. Doris Ehrt of Otto-Schott-Institut clearly describe the state of art, including pros and cons of phosphate-based photonic systems [DorisEhrt2015]. Furthermore they allow for a very high rare-earth ions loading with limited clustering effect and reduced photo-darkening, which leads to the possibility of fabricating compact optical gain devices. However, all these glasses are characterized by complex multi-composition which is not suitable for fabrication of planar structures, useful for integrated optics application by chemical or physical methods. Moreover fabrication of planar structures by ion-exchange and especially by fs laser machining is not immediate and some problems of reproducibility are still present. Sol-gel technique is a suitable method to overtake several constraints given by the melting approach and the phase diagram limits could be not so strict. So I tried to exploit the opportunities of phosphate and the skills of my group in order to develop a detailed study concerning the fabrication of $P_2O_5$ based planar waveguides having in mind to strongly reduce the complexity of the phosphate glass composition and, when possible, to limit the system to max three components. The structure and properties of these very interesting optical glasses depend mainly on the molar relation between components, and really few works report experimental data especially on the range of composition (binary or ternary). This compositional aspect is one of the main reasons suggesting us to move on parallel approach, i.e. chemical and physical deposition techniques. For these reasons we developed by RF-sputtering and sol-gel dip-coating techniques planar waveguides activated by $Er^{3+}$ ions and based on Phosphorous system. The preliminary results on the fabricated planar waveguides are reported.

This research is a step toward the crucial outcome to develop photonic glasses allowing for a very high rare-earth ions loading, with limited clustering effect and reduced photo-darkening, which lead to the possibility of fabricating compact optical gain devices. The structure of this thesis is as follows:

Chapter 1 introduces the clustering issues of RE- doped systems and its effect on spectroscopic properties in glass matrices, also this chapter is providing an historical overview.

Chapter 2 provides an overview on classes of sol-gel chemistry and description of $SiO_2$-$HfO_2$-$P_2O_5$ system, and two the most popular techniques used for sol-gel derived films fabrication.

Chapter 3 is focused on sol-gel fabrication of Erbium activated $SiO_2$-$HfO_2$-$P_2O_5$ planar waveguides, prepared with different Phosphorous precursors, then investigation of their spectroscopic properties is reported.

Chapter 4 provides a description of a sputtering process for planar waveguides fabrication, and spectroscopic tenchiques used for their characterization.

Chapter 5 introduces the experimental work on Phosporous based planar waveguides produced by RF-technique. Results of spectroscopic measurements are reported.

Chapter 6 is focused on reconstruction of dispersion curve in a multilayered $SiO_2$-$HfO_2$-$P_2O_5$ system, from an experimentally obtained values of transmittance.

Chapter 7 reports on morphological investigation of sol-gel and RF-fabricated planar waveguides using SEM and AFM measurents.

Chapter 8 provides a general description of stress and strain formation in thin films and calculation of stress in silica hafnia system.

The main objectives for this work were:

• optimisation of sol-gel fabrication protocol for $Er^{3+}$-doped $SiO_2$-$HfO_2$-$P_2O_5$ planar waveguides: choice of matrix composition, precursors, technological performance, heat treatment conditions. Investigation of the spectroscopic properties of $Er^{3+}$-doped

$SiO_2$-$HfO_2$-$P_2O_5$ planar waveguides depending on the type of Phosphorous precursors.

• optimisation of the magnetron RF technique for Phosphorous based planar waveguides fabrication: deposition rate and time, power, pressure, etc. spectroscopic investigation of prepared waveguides.

• characterisation of Phosphorous doped planar waveguides for understanding their morphological, structural properties

• dispersion curve reconstruction for sol-gel derived waveguides.

• stress investigation into the planar waveguides for better control of technological performance during the waveguides fabrication process.

[DorisEhrt2015] Doris, E. "Phosphate and fluoride phosphate optical glasses- properties, structure and applications", Phys. Chem. Glasses: Eur. J. Glass Sci. Technol. B, 56 (2015), pp. 217-234

## 1. Review of literature

## 1.1. The lanthanides

The history of lanthanides started in 1787 year with discovery of a new mineral by a Swedish lieutenant Carl Axel Arrhenius in a quarry in the village of Ytterby [Chapter_11].

Rare-earths are the elements of Periodic table with the atomic number from 57 to 71 are known as the lanthanides. These trivalent ions are characterized by a gradual filling of the 4f orbitals, from $4f_0$ (for $La^{3+}$) to $4f_{14}$ (for $Lu^{3+}$). Originally the name rare-earth ions were used for any rare-element oxides. At the present time situation is blear, some authors include only 14 elements, and others include Lanthanum, Scandium and Yttrium (Table 1.1.1) [Chapter_11].

**Table 1.1.1.** The lanthanides historical overview [Chapter_11].

| Rare-earth elements | Symbol | Origin or the name | Discoverer | Year of Discovery |
|---|---|---|---|---|
| Cerium | Ce | Roman god of corn; first asteroid discovered in 1801 | C.G. Mosander | 1803 |
| Lanthanum | La | An ancient Greek word meaning "to-lurk" | C.G. Mosander | 1839 |
| Erbium | Er | The village of Ytterby | C.G. Mosander | 1843 |
| Terbium | Tb | The village of Ytterby | C.G. Mosander | 1843 |
| Holmium | Ho | Holmia is the Latin name of Stockholm, where Holmium was discovered | P.T.Cleve | 1878 |
| Ytterbium | Yb | The village of Ytterby | J.C.G. de Marignac | 1878 |
| Samarium | Sm | The mineral samarskite was named af- | L. de Boisbaudran | 1879 |

| | | | | |
|---|---|---|---|---|
| | | ter Russian engineer Vasili Samarsky-Bykhovets (1803-1870) | | |
| Thulium | Tm | Thule is the Greek name for the north European region, including Scandinavia, where the element was discovered | P.T.Cleve | 1879 |
| Gadolinium | Gd | From the mineral gadonilite, which was named after chemist Johan Gadolin | J.C.G. de Marignac | 1880 |
| Praseodymium | Pr | Word meaning "lime-green didymium", because it was discovered in the form of green compounds | C.A. von Welbach | 1885 |
| Neodymium | Nd | Word meaning "new didymium" | C.A. von Welbach | 1885 |
| Dysprosium | Dy | Meaning "difficult to get", it is complicated to separate this metal from Holmium oxide | L. de Boisbaudran | 1886 |
| Europium | Eu | Named for the continet of Europe | E.A.Demarcay | 1901 |
| Lutetium | Lu | Lutetia is the Latin name for Paris, where it was discovered | G.Urbain | 1907 |
| Promethium | P | Promethius is the Greek god who brought the fire to mankind | J.A.Marinsky L.E.Glendenin C.D.Coryell | 1947 |

The interesting property of rare-earths is their PL ability in the wide spectral range. Depending on the RE ion the emission color is different that could be a charac-

teristic feature of the particular ion. For instance, $Eu^{3+}$ emits red light, $Tb^{3+}$ green light, $Sm^{3+}$ orange light, and $Tm^{3+}$ blue light. Such an ions as $Yb^{3+}$, $Nd^{3+}$, and $Er^{3+}$ are shows luminescence in the near-infrared. $Pr^{3+}$, $Sm^{3+}$, $Dy^{3+}$, $Ho^{3+}$, and $Tm^{3+}$ also demonstrate transitions in the near-infrared region.

All RE ions, except Lanthanum are f-shell elements. Luminescence properties of RE are explained by its electronic configuration and emission is caused due to transitions inside the 4f shell (f-f transitions). The 4f orbitals are gradually filled when moving from $Ce^{3+}$ to $Lu^{3+}$.

The partially filled 4f shell is shielded from the chemical environment by the $5s^2$ and $5p^6$ shells. This shielding is responsible for the narrowband emission and for the long lifetimes of the excited states. The general electronic configuration of lanthanides is denoted as $[Xe]4f^n5d^16s^2$, where [Xe] is the electronic configuration of Xenon, and $n$ represents the number of electrons from 0 to 14. Furthermore, two types of electronic configurations $[Xe]4f^n6s^2$($Ce^{3+}$, $La^{3+}$, $Er^{3+}$, $Ho^{3+}$, $Yb^{3+}$, $Sm^{3+}$, $Tm^{3+}$, $Gd^{3+}$, $Pr^{3+}$, $Nd^{3+}$, $Dy^{3+}$, $Eu^{3+}$, $Lu^{3+}$ and $[Xe]4f^{n-1}5d^16s^2$ (n=1-14, $La^{3+}$, $Ce^{3+}$, $Gd^{3+}$, $Lu^{3+}$) for the lanthanide atoms is possible depending on the relative energy levels. For Terbium are both configurations are energetically close [Binnemans 2009].

Cerium is an exceptional element that exhibits intense broadband emission due to f-d transitions. The emission maximum of the $Ce^{3+}$ depends on the ligand environment [Binnemans 2009].
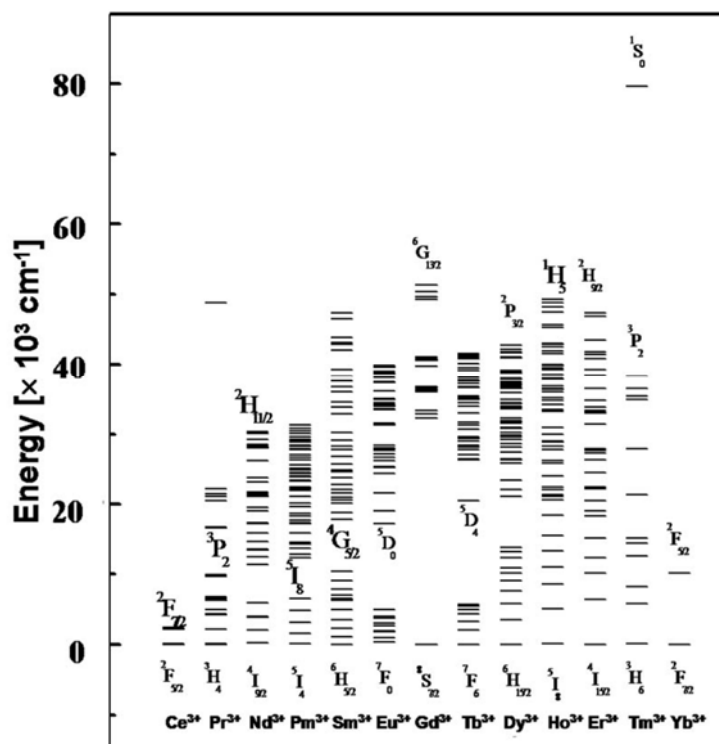
**Figure 1.1.1.** A diagram depicting the approximate energy levels for aqueous lanthanide ions [Carnall 1968].

An energy levels for the triple-charged ions of each of the 13 lanthanides from Cerium to Ytterbium with unpaired electrons on 4f orbitals (Fig.1.1.1). The observed absorption and luminescence is because of the intraconfigurational f-f transitions.

Various luminescence is occurred depending on the method of excitation, for example, photoluminescence (emission after excitation by irradiation with electro-magnetic radiation), electroluminescence (emission by recombination of electrons and holes under the influence of an electric field), chemiluminescence (nonthermal production of light by a chemical reaction), or triboluminescence (emission observed by applying mechanical stress to crystals or by fracture of crystals). In general the lanthanide compounds can be divided on inorganic compounds (lanthanide phos-phors) and molecular lanthanide compounds (i.e. diketonate complexes). A molecular lanthanide complex is embedded in an inorganic matrix (sol-gel materials) or an in-organic lanthanide compound is embedded in an organic matrix. Such materials are defined as lanthanide-based organic-inorganic hybrid materials [Binnemans 2009].

## 1.2 Non-radiative and radiative relaxation of excited lanthanide ions

In spite of efficient PL the RE are tends to show weak light absorption. For the most of transitions in the absorption spectra have the molar absorption coefficients $\varepsilon$ smaller than 10 L mol$^{-1}$ cm$^{-1}$, and only a very limited amount of radiation is absorbed by direct excitation in the 4f orbitals. Since the luminescence intensity is not only proportional to the luminescence quantum yield but also to the amount of light absorbed, weak light absorption results in weak luminescence. However, the problem of weak light absorption can be overcome form antenna effect (or sensitization). It was observed that lanthanide complexes with organic ligands upon excitation in an absorption band of the organic ligand have demonstrated an intense metal-centered luminescence. More light can be absorbed by the organic ligands than by lanthanide because of the intense absorption bands of organic chromophores. The excitation energy from the organic ligands to the lanthanides is transferred by intramolecular energy transfers. The phenomenon of the the Eu$^{3+}$ complexes of salicylaldehyde, benzoylacetone, debenzoylacetone, debenzoylmethane, and meta-nitrobenzoylacetoen was described in the work of Weissman and then proved by experiments of Sevchenko and Trofimov [Binnemans 2009, Carnall 1968, Weissman 1942].

The mechanism of the energy transfer from the organic ligand to the RE ion were investigated in 1960s, and research in the field of luminescent materials based on molecular lanthanide complexes is in progress.

The energy transfer mechanism from the organic ligands to the lanthanide was studied by Crosby and Whan [Binnemans 2009, Whan 1962, Crosby 1961, Crosby 1962].

Lanthanide complex with organic ligands are excited to a vibrational level of the first singlet state upon irradiation with ultraviolet radiation. The molecule undergoes fast internal conversion to lower vibrational levels of the S1 state. When the excited singlet state are relaxed to the ground state or undergo nonradiative crossing from the singlet state S1 to the triplet state T1 occurs molecular phosphorescence.

The complex can undergo a nonradiative transition from the triplet state to an excited state of the RE ion. The RE ion can undergo a radiative transition to a 4f state or relaxed by nonradiative processes. The explanation of nonradiative relaxation of the lanthanide ion by its vibronic coupling with the ligand and solvent molecules were explained by Whan and Crosby. The typical example of such process is $Tb^{3+}$ and $Eu^{3+}$ ions which are not efficient due to the short lifetime of the singlet excited state. The work of Veggel and co-workers showed the direct excitation 4f levels of a $Nd^{3+}$ ion for dansyl- and lissamine-functionalized $Nd^{3+}$ complexes from a singlet state [Binnemans 2009, Kleinerman 1964, Misra 2008, Yang 2004, Hebbink 2002].

The RE ion luminescence is possible from the resonance levels characteristic for different lanthanide ions. When the lanthanide ion is excited directly by 4f levels excitation or by energy transfer, the excitation energy is dissipated via non-radiative process until a resonance level is achieved [Binnemans 2009].

The population of the resonance level can be achieved when the lowest triplet state of the complex is placed at an energy level equal or above the resonance level of the RE ion. Molecular fluorescence or phosphorescence of the ligand is observed when the energy levels of the organic ligands are below of the resonance level of the lanthanide ion and no light emission occurs [Binnemans 2009].

Changing the ligand is possible to control the luminescence intensity of the lanthanide because the position of the triplet level depends on the type of ligand. Some remaining ligand emission combined with the lanthanide-centered emission can be also observed [Binnemans 2009].

If the ligand-to-metal charge transfers (LMCT) lays at low energy levels its quench the luminescence in some extent. For instance, $Er^{3+}$ sensitization through a LMCT state exhibit metal-centered luminescence, if the energy of the LMCT is higher than 25 000 $cm^{-1}$ [Binnemans 2009, Lazarides 2008A, Ward 2007, Ronson 2005, Lazarides 2008B, Shavaleev 2003, Chen 2008].

The efficiency of the emission process in RE doped materials can be evaluated through the luminescence quantum yield $\Phi$ (Eq.1), which means the ratio of the emit-

ted photons to the absorbed photons per time unit [Binnemans 2009, Fery-Forgues 1999].

$$\Phi = \frac{N_{emp}}{N_{absp}} \qquad (1)$$

where $N_{emp}$ is the number od emitted photons and $N_{absp}$ is the number of absorbed photons.

Sensitization of the RE ion depends on the level can go through several migration paths, for this reason the quantum yield of the lanthanide complexes depends on the excited state of the ligand (metal ion).

The total luminescence quantum yield $\Phi_{tot}$ of lanthanide complexes (Eq.2) is determined by the efficiency of sensitization or energy transfer ($\eta_{sens}$) and by the quantum yield of the lanthanide luminescence step ($\Phi_{Ln}$) [Binnemans 2009, Werts 2004].

$$\Phi_{tot} = \eta_{sens}\Phi_{Ln} \qquad (2)$$

The direct excitation in the 4f levels of the RE ion gives the intrinsic quantum yield ($\Phi_{Ln}$). $\Phi_{Ln}$ is defined as the rate constants for radiative relaxation ($k_r$) and non-radiative relaxation ($k_{nr}$) by the following relationship, Eq. 3:

$$\Phi_{tot} = k_r /(k_r + k_{nr}) \qquad (3)$$

The intrinsic quantum yield ($\Phi_{Ln}$) shows how efficient is the radiative process compete with non-radiative processes. $K_r$ is a factor independent from temperature.

Quench of the energy transfer and OH-, NH- vibrations contribute to $k_r$ and has strong influence of the RE luminescence. The nonradiative processes have an influence on the observed luminescence lifetime, and do not the radiative lifetime [Binnemans 2009, Haas 1971].

The physical meaning of the radiative lifetime is the time of an excited state in the absence of nonradiative transitions. The temperature-dependent element contributes the rate constant of the nonradiative processes when upper-lying short-lived excited states are thermally reached. The temperature-independent element is accounted when relaxation to the ground state occurs.

The intrinsic quantum yield can be obtained using the Eq.4:

$$\Phi_{Ln} = \frac{\tau_{obs}}{\tau_{rad}} \qquad (4)$$

where the observed lifetime can be derived from intensity decay curves.

Radiative lifetime of $Nd^{3+}$, $Er^{3+}$, and $Ho^{3+}$ can be calculated with the experimentally derived Judd-Ofelt intensity parameters, which can be obtained from the RE optical absorption spectra. For $Pr^{3+}$ ions is complicated to apply Judd-Ofelt theory. Radiative lifetime of $Eu^{3+}$ can be determined using Einstein coefficient for spontaneous emission A of the magnetic dipole transition $D_0^5 \to F_1^7$, the refractive index n, and the ratio of the total integrated intensity to the integrated intensity of the $n$, and the ratio of the total integrated intensity to the integrated intensity of the $D_0^5 \to F_1^7$ transition. The total quantum yield $\Phi_{tot}$ can be experimentally measured [Binnemans 2009, Werts 2004].

The relative quantum yield is determined by comparison of the unknown and reference sample, Eq.5:

$$\Phi_X = \left(\frac{A_R}{A_X}\right)\left(\frac{E_X}{E_R}\right)\left(\frac{n_R}{n_X}\right)^2 \Phi_X \qquad (5)$$

where $\Phi$ is the luminescence quantum yield, A is the absorbance at the excitation wavenumber, E is the area under the corrected emission curve , and n is the refractive index of the solvents used. The preferable variant is when the sample and the reference have the same absorbance at the excitation wavelength. The recommended absorbance value is up to 0.5. The emission intensity can no longer be assumed proportional to the sample concentration when this value is above 0.5. If the absorbance is too low the presence of impurities in the medium can be crucial.
The ratio $(n_x/n_r)^2$ is equal to unity when is the same solvent is used for the reference and the unknown sample [Binnemans 2009].

Cresyl violet 54 % in methanol, rhodamine 101 ($\Phi$=100 % in ethanol) can be used as standards for the measurements of luminescence quantum yield of $Eu^{3+}$ complexes.

For $Tb^{3+}$ complexes, quinine sulfate $\Phi$=54.6 % in 0.5 M aqueous $H_2SO_4$ and 9,10-diphenylanthracene $\Phi$=90 % in cyclohexane can be used. The absolute quantum

yield of the Eu$^{3+}$ thenoyltrifluoroacetonate complex [Eu(tta)$_3$] in acetone was directly measured in the work of Gudmundsen. The luminescence quantum yield characterizes the luminescence quenching in the whole system, while the luminescence decay time indicates the extent of quenching only at the emitting site. Bauhmik has studied the temperature dependence of the quantum yield and the decay time for the different Eu$^{3+}$-diketonate complexes in various solvents [Binnemans 2009, Eaton 1988, Gudmundson 1963, Bhaumik 1964].

The similar luminescence decay time at 77 K (ca.450 µs) was observed for various complexes, whereas in contrast the values were different at room temperature.

The presence of fluorine in the ligands results in decrease of quenching and in an increase of the decay time at room temperature. Luminescence decay times of the Eu$^{3+}$ complexes were equal at 77 K, and the luminescence quantum yields were different. What means that quenching occurs also in the ligand and not only at the lanthanide ion site [Binnemans 2009].

## 1.3 Chemical limitations of RE ions concentration in the vitreous medium

The influence of chemical limitations becoming more significant when the RE ions concentration is increasing. The concentration is limited up to $0.7 \cdot 10^{18}$ cm$^3$ because one glass-constituent in silica glass is smaller than RE ion and leaves too small space for large RE ions.

However, the RE ions works in glass matrix as glass-modifiers and not as glass-forming compounds. That fact leads to devitrification of glass when a high RE concentrations are used.

Al-codoping of silica matrix makes easier the homogeneous introduction of the RE ions at low concentrations. High doping level of glass matrix could be also limited by physical factors.

\

## 1.4 Physical limitations of RE ions concentration in the vitreous medium

The physical concentration limitation takes place before chemical concentration is achieved. This limitation arises from an independent ion-ion interactions lead to concentration quenching. The excitation energy is diffused undergo ion-ion interactions until it collected by hydroxyl groups. Clusters reveals by energy transfers between two excited ions that are placed close to each other, what results in APTE upconversion. Energy transfer occurs by dipole-dipole interactions at the distance about 30 Å while the chemical clustering rises when the distance between the neighboring ions is less than a few Å. The radiative energy transfer can take place at the macroscopic distances when ions are in resonance.

## 1.5 Physical clustering in RE-doped glasses

At high RE ions concentration in Erbium-doped fibers not only self-quenching arise, also non-saturable absorption of excitation level with a relative gain reduction occurs. This leads to so-called pair-induced quenching (PIQ). Clustering is caused by pair of ions connected by up-conversion energy transfer. This clustering process involves two ions in intermediate excited state which relax quickly. Then one ion stay in ground state (so-called non-saturable absorption), and the second ion is relaxing from the double excited state. Physical process is common for clusters with millimeter or at least of several tens of Å size, that is far from chemical limitations and should be called "interaction clusters".

## 1.6 Chemical clusters and their physical signature by a co-operative luminescence probe.



APTE effect
YF$_3$:Yb:Er
η=10$^{-3}$ cm$^2$/W

Cooperative luminescence
YbPO$_4$
η=10$^{-8}$ cm$^2$/W
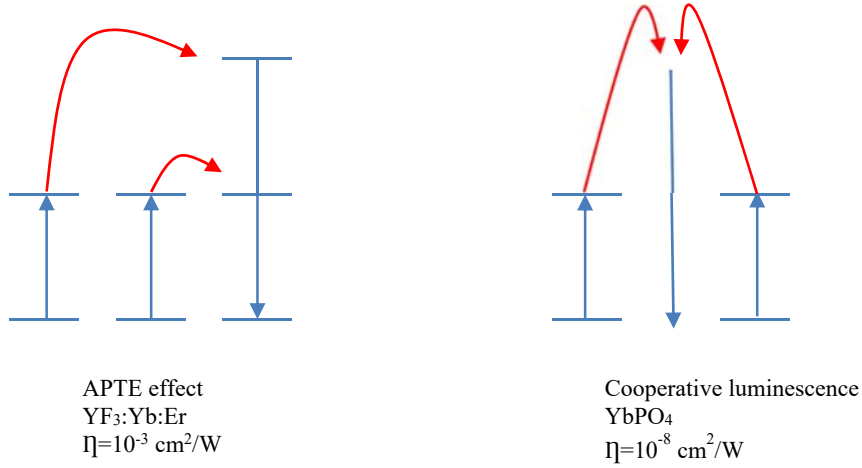
**Figure 1.6.1.** Energy diagram of APTE and cooperative upconversion process for Tb-Er and Yb ion system with their efficiencies, respectively [arranged by Auzel 2001, Auzel 1999].

In the Figure 1.6.1 is presented the energy scheme and up-conversion for APTE effect and co-operative luminescence. On the assumption that ion-ion interactions between the two RE ions caused by the dipole-dipole process, co-operative luminescence and APTE could be observed with the same detectivity if the distance between the ions is long. The ratio of the critical distances ($R_0$) for APTE and cooperative luminescence can be derived from the Eq. 5:

$$\frac{\text{Ro}_{\text{coop}}}{\text{Ro}_{\text{APTE}}} \approx \left(\frac{\eta_{\text{APTE}}}{\eta_{\text{coop}}}\right)^{\frac{1}{6}} \approx (10^5)^{\frac{1}{6}} \approx 6.8 \qquad (5)$$

where it is assumed that the ion-ion interaction is of dipole-dipole type with R$^{-6}$ distance dependence. In this case $R_0$ ranges from 6 to 30 Å, and the $R_{0(\text{coop})}$ is around 4.5 Å.

RE-doped glasses prepared by chemical incorporation of RE ions into the glass matrix in the form of RE$_2$O$_3$ oxides, for fluoride in the form of REF$_3$, and RE$_2$O$_3$/ REF$_3$ for fluorophosphates glasses. This approach works very well up to the $10^{20}$ cm$^3$ RE ions concentration, then during the glass preparation process at the mel-

ting step some ions are aggregated at the minimum interionic distances 3.5 Å for $Re_2O_3$ and 3.6 Å for $REF_3$. From the literature is known that at the $10^{20}$ $cm^3$ RE ions concentration the average distance between the ions should be about 13.4 Å. Effectively this distance is much greater than it was reported for doping species [Auzel 2001, Auzel 1999, Auzel 1994].

In order to minimize the clustering a new doping principle has been proposed by Auzel and Goldner. The backbone of the idea is to introduce precursor crystallites with already large minimum RE-RE distances. This approach ensure that if even during the melting process of glass preparation not all of the species will be dissolved the large minimum RE-RE distance is constant. RE crystallites were introduced into the phosphate glass of the following composition:

$P_2O_5$=80,99 %, MgO=7,65 %, $Li_2O$=11,36 %. Phosphate glass was doped with various $Yb^{3+}$ precursors with fixed concentration at $5.2 \times 10^{20}$ $cm^3$ [Auzel 2001].

Obtained glass has slightly different composition when $Yb^{3+}$ precursor contains ions which are not present in glass composition. It is true of $YbLaO_3$, YbOF, $YbF_3$. Auzel and Goldner show that using co-operative luminescence excitation the shape and the intensity of the absorption spectra is modified by the doping procedure. An IR spectrum was not dependent from the doping procedure. The corresponding co-operative luminescence is changing by the type of the doping precursor. The $YbP_3O_9$ precursor with the largest $Yb^{3+}$-$Yb^{3+}$ minimum distance 5.2 Å presents the less normalized intensity. High intensity was observed for the $Yb_2O_3$ precursor with the smallest $Yb^{3+}$-$Yb^{3+}$ minimum distance (3.5 Å) [Auzel 2001]. This observation is due to the fact that the concentration of RE introduced by the precursors was high and not present in the glass initially.

The same effects of the RE precursors minimum distance on the intensity of co-operative luminescence has been observed for fluorophosphates glasses. For fabrication of $Nd^{3+}$- doped phosphate glasses was proposed to choose the glass composition close to ultraphosphate region which is near to the pentaphosphate crystal composition. This composition is characterized by low $Nd^{3+}$ concentration quenching. It

was expected that during the first steps of phosphate glass preparation, quasi-pentaphosphate Nd-microcrystals are present in the matrix which guarantee the minimum $RE^{3+}$-$RE^{3+}$ distance. Self-quenching can be reduced by introducing into the glass $REP_2O_5$ or $REP_3O_9$ instead of $RE_2O_3$ [Auzel 2001, Denker 1981].

## 1.7 RE clustering reduction by introduction of lanthanide molecular complexes

The clustering of RE ions in sol-gel glasses can be reduced by using lanthanide acetate salts [Binnemans 2009, Chakrabarti 1994, Sahu 1996]. The weak light absorption by the lanthanide ions because of clustering can be solved by replacing the lanthanide salt precursors by molecular lanthanide complexes. In a such molecular complexes, the RE ions are surrounded by a shell of absorbing organic ligands, which transfer the excitation energy to the lanthanide ion. These organic ligands act as a shield preventing the lanthanide ion from interaction with the hydroxyl groups in the matrix. It was observed the thermal stability of the lanthanide complex was also improved after incorporation in a silica xerogel. The first attempts of incorporation of the molecular lanthanide complexes in a sol-gel matrix were performed by Matthews and Knobbe. They incorporated $Eu^{3+}$-diketonate complexes in a silica sol-gel glass and studied the luminescence behavior of the $[Eu(tta)_3(H_2O)_2]$ and $(pipH)[Eu(tta)_4]$ complexes [Binnemans 2009, Matthews 1993]. The choice of these complexes is explained by their intense photoluminescence and high solubility in DMF. The adding of DMF to the starting solution prevents the sol-gel glass from cracking during the drying process [Binnemans 2009, Adachi 1988]. The spontaneous emission cross sections for the glass doped with $Eu^{3+}$-diketonate complexes were 2-3 orders of magnitude more intense than those for glasses doped with hydrated $EuCl_3$. Yan et al. studied the luminescence lifetime of the $[Eu(dbm)_3(phen)]$ and $[Tb(acac)_3(phen)]$ complexes into a silica sol-gel glass. The luminescence lifetime of the complexes was found to be longer than that for the pure complexes in the solid state [Binnemans 2009, Matthews 1994, Yan 1997].

The preparation of compact silica glass based on a xerogel doped with molecular lanthanide complexes is limited by their thermal stability and prevents heating the samples to 800 °C and higher temperatures. The luminescence intensity decrease rapidly due to the thermal decomposition of the complex.

Lanthanide complexes can be dissolved in the sol-gel solution, but they are often not stable in the acidic precursor solution. Instead of the complex, the ligands and a lanthanide salt can be added to the precursor solution. The complex formation occurs in situ during the transformation of the gel into a xerogel [Binnemans 2009, Sun 2005A, Qian 1997, Sun 2005B].

For instance, a [Eu(tta)$_3$]-doped sol-gel film made of a sol codoped with EuCl$_3$ and Htta, where the Europium(III) -diketonate complex was gradually formed upon heat treatment. At the temperatures above 130 °C, the luminescence intensity reduced due to the decomposition of lanthanide complexes [Binnemans 2009, Hao 1999].

Another way to absorb efficiently the light and transfer the excitation energy to the lanthanide ion is to replace the organic ligands by inorganic nanoparticles. Tb$^{3+}$-containing glasses codoped with Ce$^{3+}$ shows enhanced luminescence due to intense absorption in the ultraviolet region, and the excitation energy can be transferred to the energy levels of Tb$^{3+}$ [Binnemans 2009, Gutzov 2006, Malashkevich 2004, Jia 2006].

The enhancement of Eu$^{3+}$ luminescence in sol-gel glasses can be achieved by Bi$^{3+}$ codoping. Eu$^{3+}$ ions can be also sensitized via Eu$^{2+}$ ions that are present in the sample. It is also possible to prepare sol-gel glasses that contain only Eu$^{2+}$ ions. It was notices that the emission intensity of Eu$^{2+}$ in a silica sol-gel glass was increased by about 250 times by cooping of the glass with 1 % of Alumina [Binnemans 2009, Kim 2001, Biswas 2000, Nogami 1996].

The increase of luminescence intensity in Tb$^{3+}$ doped silica glasses was observed when Germanium was incorporated into the matrix, probably due to energy transfer from Germanium-related defects in silica [Binnemans 2009, Bredol 2002, Bredol 2003].

Sol-gel derived glasses are usually composed of silica ($SiO_2$). The silicon alkoxide precursors can be replaced by other metal alkoxides that will allow to obtain other types of oxide materials like Germania ($GeO_2$), Titania ($TiO_2$), Zirconia ($ZrO_2$), Alumina ($Al_2O_3$), Hafnia ($HfO_2$), Tantalum ($Ta_2O_5$) [Binnemans 2009, Kojima 2000, Lecomte 1991, Kiisk 2005, Gapotenko 2001, Palomino-Merino 2001, Reisfeld 2001, Reisfeld 2003, Bucella 2004, Reisfeld 2000, Ciuffi 2002, Kurokawa 1998, Kiisk 2005, Chacon-Roa 2008, Villanueva-Ibanez 2003, Li 2000]. These metal and transition-metal alkoxides are more reactive in hydrolysis and condensation reactions than the Silicon alkoxides. It is possible to obtain mixed silica-metal oxide gels by mixing these metal alkoxides with Silicon alkoxides. Silicon substitution by other metals in the sol-gel glasses allows tuning of the physical-chemical properties such as refractive index, and reaching a more homogeneous dispersion of the lanthanide ions in the glass matrix. Mixed oxide systems are characterized by formation of discrete crystalline phases during synthesis, for instance, $Er_2Ti_2O_7$ formation in the Erbium-doped $SiO_2$-$TiO_2$ system. Zirconia and hafnia active planar waveguides are very interesting due to their similar properties: chemical and photochemical stability, high refractive index, and low phonon energy. Hafnia and Titania coating can undergo photochemical damage after long-term exposure. Zirconia sol-gel glasses are a suitable medium for near-infrared lanthanide ions. The luminescence intensity of $Eu^{3+}$ and $Tb^{3+}$ ions is higher in Zirconia host matrix than in silica sol-gel glasses. The high refractive index and the high dielectric constant of the Zirconia matrix allow the higher luminescence intensity. Some of the lanthanide ions exhibit luminescence in Zirconia glasses and not in silica glasses. This phenomenon was explained by the clustering formation of $Sm^{3+}$ ions in silica glasses, resulting in cross relaxation [Binnemans 2009, Koslova 1993, Coutier 2000, Strohhofer 1998, Zevin 1997, Goncalves 2004].

The preferred method of Alumina films preparation is not via an alkoxide precursor but via an aqueous sol-gel route through the hydrolysis of an aqueous $AlCl_3$ solution by an aqueous $NH_3$ solution [Binnemans 2009, Ishizaka 2001].

The reason for incorporation of the spectroscopically active lanthanide ions in sol-gel xerogels and glasses is to use these ions as spectroscopic probes for studying structural changes in the sol-gel matrix during transformation of gel into a xerogel [Binnemans 2009].

One of the interesting systems was a sol-gel glasses doped with $Yb^{3+}$, $Er^{3+}$. $Yb^{3+}$ absorbs the light and transfer the excitation energy to the $Er^{3+}$, which has near-infrared luminescence [Binnemans 2009, Orignac 1999].

Codoping is usually used to prepare near-infrared emitting glasses. Cerium-doped sol-gel glasses show strong broadband light absorption in the visible spectral region. The intense absorption bands were attributed to the presence of $Ce^{4+}$-O-$Ce^{3+}$ and $Ce^{4+}$-O-$Fe^{3+}$ clusters [Malashkevich 2002].

Codoping of porous xerogel by lanthanide ions or lanthanide complexes could be performed by impregnation, where the xerogel is placed in a solution containing a lanthanide-based complex or salt. This method has been used to absorb lanthanide ions or complexes on porous Vycor glass. Another researchers obtained luminescent material when soaked the xerogels in the solution of benzoic acid with $TbCl_3$ [Binnemans 2009, Hazenkamp 1990, Mack 1983, Gerasimova 2006, Bredol 1998].

Less rich information is about near-infrared emitting lanthanide complexes incorporated into sol-gel silica glasses. Dang et al. introduced [Ln(tta)$_3$(phen)], [Ln(tta)$_3$(bipy)], and [Ln(tta)$_3$(tppo)$_2$] complexes via an in situ synthesis, where Ln - Ho, Tm, into sol-gel silica glasses. The Holmium and Thulium complexes show near-infrared emission. The luminescence intensities of the complexes in the sol-gel glasses were weaker than in pure solid complexes. This effect can be connected with the quenching of the excited states by residual OH groups. The luminescence lifetime in sol-gel glasses are shorter than in the solid complexes [Binnemans 2009].

The lanthanide-doped sol-gel glasses present an upconversion. Upconversion is a process which occurs when the emission energies larger than the excitation energy. An example, $Tb^{3+}$/$Yb^{3+}$- codoped sol-gel glasses, where $Tb^{3+}$ is excited via energy transfer processes by $Yb^{3+}$ ions. Two near-infrared photons absorbed by $Yb^{3+}$ ion can

be transformed into a green photon emitted by $Tb^{3+}$ ion [Binnemans 2009, Auzel 1966, Martin 2001]. Yellow upconversion was observed in a glass codoped with $Yb^{3+}$ and $Eu^{3+}$. Sol-gel silica glass codoped with 1 mol. % $Yb^{3+}$ shows blue cooperative upconversion [Maciel 2000].

Red-to-blue upconversion was observed for a $Tm^{3+}$-doped glass and red-to-green upconversion was observed for an $Er^{3+}$- doped sol-gel glasses [Xu 1995, Otto 2000].

### 1.8 The effect of Aluminum co-doping. Theoretical approach

The influence of $Er^{3+}$- $Al^{3+}$ complexes on clustering formation process were investigated by three structural models (Fig.1.8.1) [Laegsgaard 2002].
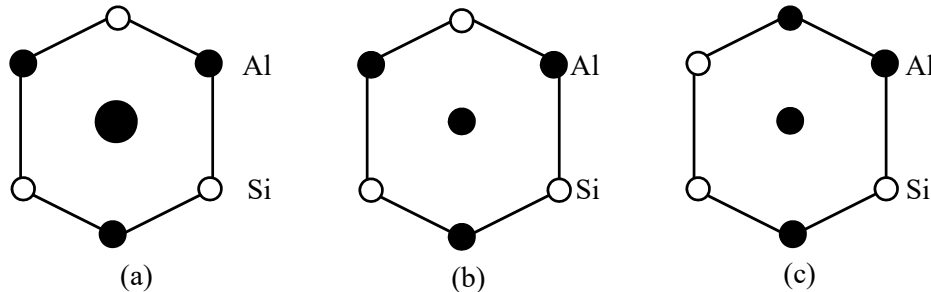


**Figure 1.8.1.** Schematic representations of various $Er_2O_3$ and $Al_2O_3$ states in a silica network [Laegsgaard 2002].

The first model (a) includes only $Er^{3+}$ clusters without any codopants. The second structural model (b) shows $Er^{3+}$ - $Al^{3+}$ complex. In the third model only $Al^{3+}$ is present in the absence of $Er^{3+}$ ions. $Er^{3+}$ clusters formation in the solid is improbable in the presence of sufficient O to oxidize all the cations. As development model for clusters $Er_2O_3$ and $Er_2Si_2O_7$ can be used. These structural models doesn't consider the kinetics of cluster growth, but thermodynamic balance between large Er clusters

and dispersed  Er-Al complexes can be modeled and studied. $ErAl_3O_6$ clusters formed in six-membered ring structure where every second silica atom is substituted with Al ions, and the missing valence electrons are delivered by Er ion in the center of ring. In the $ErAl_3O_6$ state the Al are surrounded with four O ions at an average distance of 1.75Å, and a second coordination shell of four Si atoms at an average distance of 3.2 Å. At this state the Er atom is at a distance of 2.78 - 3.26 Å from the Al ions. Sen and al. obtained by EXAFS the similar distance values of 1.77 and 3.12 Å, respectively. The valence of Al and Er is equal and in absence of Er the interstitial Er can be replaced by Al ion (Fig. 1.8.1), and $Al_4O_6$ is formed. The Al bond length in the structure depicted in Fig.1.8.1 (b) is 1.77 Å and 1.80 Å for the structure shown in Fig. 1.8.1 (c). The slight increase in the bond length is explained that the interstitial Al ion has longer bonds than the substitutional Al ions. The structures with interstitial Al ions are presented in Fig.1.8.1(b) and (c) [Laegsgaard 2002, Sen 2000].

The role of thermodynamic parameters in glassy systems depends on the fabrication process of the glass. The silica glasses prepared by melting quenching technique can be considered a frozen-in state corresponding to temperature frictions below the melting point (1736 °C).  The Er clustering is observed during the annealing steps. Assuming the annealing time sufficiently long for local distributions (through diffusion process), therefore the impurity state distribution over lattice corresponds to a thermodynamical equilibrium at the anneal temperature [Laegsgaard 2002].

Heat treatment of RE -doped glass obtained by sol-gel and PECVD methods is used to increase the glass transparency. Increase of the RE ions concentration into the glass matrix without RE diffusion and clustering is possible by limitation of duration and heat treatment temperature.

Long-term annealing at high temperatures can be also reasonable from thermodynamic point of view as a way to attain thermodynamic equilibrium at a temperature high enough to favor dissolved RE ions.

## 1.9 The effect of Al on the RE clustering in the glass

Each RE ion dissolved in the glass requires three non-bridging oxygens to compensate a charge. A quite large number of non-bridging oxygens are needed to screen the electric field of RE ions. The RE ions into a rigid silicate glass matrix cannot induce the necessary coordination number of non-bridging oxygen atoms and the clustering becomes energetically favorable with formation of the general non-bridging oxygen atoms environment. The Aluminum ions embedded in the silicate glass matrix forms $AlO_{4/2}^-$ which surround RE cations and then reduce the free energy of RE solution, increasing the solubility of them into the silica glass.

In the several works were reported that $Al^{3+}$ codoping is effective for RE ions dispersion in silica gel and silicate glass [Nogami 1996, Kurokawa 1998, Arai 1986 Wang 1993, Lochhead 1994, Kurokawa 1994, Biswas 1994, Pasquale 1995, Ryu 1995, Lochhead 1995, Nogami 1996, Hehlen 1997, Benatsou 1997, Nogami 1997, Zhou 1997, Pucker 1998, Almeida 1998, Orignac 1999, Armellini 1999, Nogami 2000, Jin 2000, Xiang 2000, Rocca 2001, Ishizaka 2002]. Conclusive explication how the RE ion isolation occurs is still under investigation. A general point of view is that Al-O-RE bonds are forming instead of RE-O-RE when RE ions partitioned by $Al^{3+}$. In the several papers the fluorescence decay has been studies to investigate the $Al^{3+}$ effect on the luminescence quantum yield in RE-doped materials [Lochhead 1995, Nogami 1997, Pucker 1998, Orignac 1999, Armellini 1999, Xiang 2000, Stone 1996, Chiasera 2003]. In the Figures 1.9.1 (a) and (b) illustrated two monolithic bulk silica-gel glasses (EY1 and EYA3), containing 0 and 30 000 Al/Si ppm, respectively. Both glasses were doped by the same $Er^{3+}$ and $Yb^{3+}$ concentrations, i.e. 10 000 Er/Si (ppm) and 20 000 Yb/Si (ppm) [Chiasera 2003].
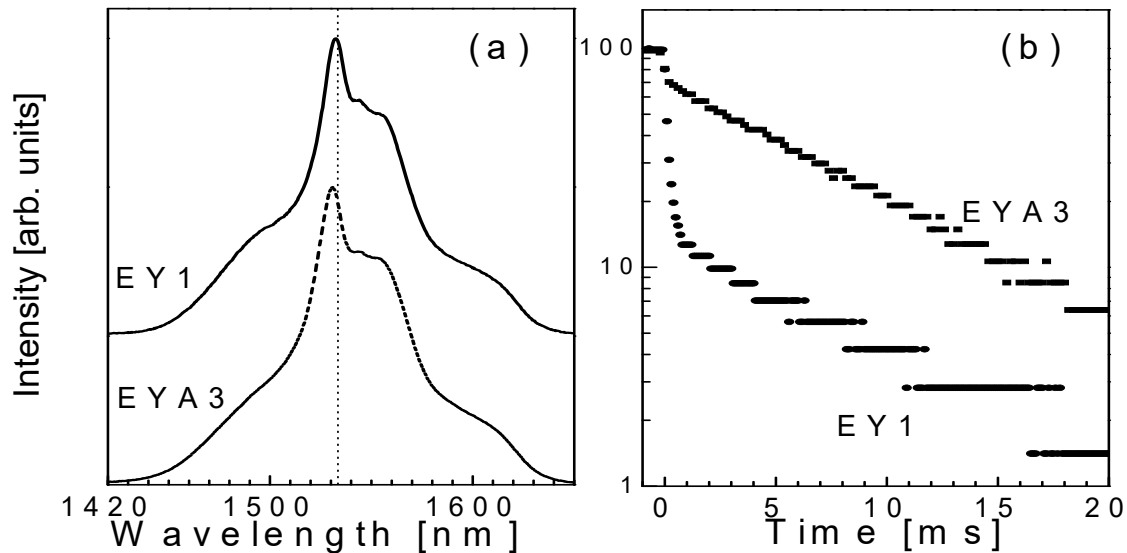
**Figure 1.9.1.** Room temperature PL spectra of the $^4I_{13/2} \rightarrow \, ^4I_{15/2}$ transition (a) and decay curves from the $^4I_{13/2}$ level of $Er^{3+}$ ions (b) under excitation at 514.5 nm, for the 10 000 Er/Si ppm, 20 000 Yb/Si ppm $SiO_2$ gel-derived glasses with 30 000 (EYA3) and 0 (EY1) Al/Si ppm [Chiasera 2003].

In the Figure 1.9.1 (a) observed a slight rise in the flatness and in the band width in the Al-doped glass (bandwidth of 55 nm for the Al-doped sample, versus 51 nm for the one without Al). Obtained values are similar to the results in Al-doped silica glasses and larger than those in silicate glasses [Duverger 2001]. The peak position shifts from 1532.5 nm were fixed for EY1 sample to 1531 nm for EYA3. Similar shifts have been reported in literature for melted and sol-gel glasses codoped with Al [Stone 1996]. Whereas both decay curves in Fig. 1.9.1 (b) are not single exponential, but the sample (EY1) without Al exhibits a faster initial decay, indicating that $Er^{3+}$-$Er^{3+}$ energy transfer is effective: $\tau_{1/e}$ is about 0.1 ms for the sample EY1 and 5.6 ms, for the sample EYA3. It confirms the role of Al in the minimization of the RE clustering.

Aluminum codoping of $Er^{3+}$-activated silicate matrix ensure complete cluster dissolution of $Er^{3+}$ up to $10^{19}$ $cm^{-3}$ ion concentration when the Al/Er ratio is around 10 and higher.

Arai and co-workers introduced the "solvation shell" model based on the RE ions introduced in Alumina. Using the electron-spin-echo envelope modulation

method to detect the interaction of the magnetic moments of the $Al^{3+}$ nuclei and the 4f shell of Nd in Nd/Al-doped silica glass showed that the $Al^{3+}$ is correlated to $Nd^{3+}$, at a distance of about 3Å. In Al doped silica clustering of $Al^{3+}$ was not detected. Moreover, EXAFS study of Nd/Al-doped glass found no prominent change in the local $Al^{3+}$ environment between Nd/Al and pure Al doping. In particular, the local environment of the $Al^{3+}$ does not changed significantly during the complex formation with RE ions. Only a fraction of the $Al^{3+}$ is close to the RE ions. In such a way, the solvation shells of Arai et al. are clusters of Aluminum.

Sen reported that for charge balancing each RE ion is correlated to three $Al^{3+}$ ions. This fact confuse keeping an atomic Al/RE ratio of about 10 and no less to guarantee good dissolution of RE in silica glass. The low solubility of RE ions in silica matrix is explained by mismatch in size and valence between the RE ions and the constituents of the silica network. For instance, $Er^{3+}$ ions in $Er_2O_3$ and $Er_2Si_2O_7$ bonded to six O atoms. Assuming purely ionic bonding, an $Er^{3+}$ ion donate half an electron to each of neighboring Oxygen anions. Moreover, a tetrahedrally coordinated Si ion donates one electron to each $O^{2-}$ neighbor. The $ErO_6$ unit fits poorly into a silica network and energy gained by forming clusters. When $Al_2O_3$ oxide is added into a silica glass the difference in valence electron number is compensated. If three substitutional $Al^{3+}$ ions are placed close to each other, the compensating charge may be provided by and $Er^{3+}$ ion accommodated into the silica network. It is important to mark that an $Al_2O_3$ content exceeding 4 mol. % leads to glass matrix devitrification.

Hafnium oxide can be used as an alternative to $Al^{3+}$ ions as a high refractive index material with a transparency over a wide wavelength (0.3-10 μm). Hafnia and silica glass have been used to form high index-contrast multilayer structures with high laser damage threshold.

The Alumina codoping was efficient enough to reduce $Er^{3+}$ ions clustering in the following glass composition $1.0Er_2O_3 + 1.8Al_2O_3 + 97.2SiO_2$. The microscopic clustering of $Er^{3+}$ ions is caused by its large field strength what limits liquid immiscibility in the $Er_2O_3$ - $SiO_2$. Generally, when a RE ion is incorporated into the silica ma-

trix, it has to be co-ordinated to a high number of non-bridging oxygens to screen the electric charge of the cation. The addition of $Er_2O_3$ into the silicate glass generates a limited number of non-bridging oxygens to achieve electrical neutrality. Consequently, the Erbium ions form a cluster to share the limited number of non-bridging oxygens. Addition of $Al^{3+}$ into the silica matrix doped with $Er^{3+}$ allows sharing non-bridging oxygen with Erbium ion to reduce clustering and work as a mutual solvent for Erbium and silica.

Clustering of the RE in host glasses can be studied by spectroscopic or structural analysis. The RE clustering from structural point of view is the number of other RE ions linked to a given RE ion via oxygen. In the structural studies, the clustering is the coordination number of RE-RE partial correlation function.

In the work of Lochhead and Bray was shown the effect of $Al^{3+}$ on $Eu^{3+}$ ions dispersion in silica sol-gel matrix. Strong ionic field strength of $Al^{3+}$ allows interacting with the silica matrix and penetrating the RE clusters for a more uniform distribution. Aluminum ions works as a network former whereas more preferable to use the other ions which acts as network modifiers. For instance, the $Ga^{3+}$, $Sc^{3+}$,$Lu^{3+}$ cations with the strongest charge density acts as network modifiers are very effective in preventing clustering.

The samples without inorganic codopants present strong $Eu^{3+}$ clustering. In $SiO_2$ - $Al_2O_3$ the luminescence intensity of $Eu^{3+}$ was detected in two times higher than in the glasses without $Al_2O_3$. Aluminum co-doping of $Tb^{3+}$-containing sol-gel glasses show the dispersive action of Aluminum if the Al/Tb ratio is larger than 10. Sol -gel glasses codoped with Aluminum show a strong tendency to retain OH groups in the densified matrix after heat treatment. Thus, the use of Aluminum as a codopant is less beneficial for near-infrared application than for the visible spectral region.

The conventional sol-gel preparation was modified by mixing $NH_4OH$ solution with Er -salt solution. They consider that the partially hydrolyzed MPTS transformed to fully hydrolyzed reacting with $NH_4OH$ solution. After the mixing Er - containing

solution with NH$_4$OH they obtained milky white precipitate which after 10 h stirring becomes a clear solution.

The clear homogeneous solution was obtained by the following reactions:

$$3NH_4 + 3OH^- + Er^{3+} + 3NO_3 \rightarrow Er(NO)_3 + 3NH_4NO_3 \tag{1.9.2}$$

$$-Er(OH)_3 + 3[HO - (Al - O - Si - R)_n] \rightarrow Er[O - (Al - O - Si - R)_n]_3 \tag{1.9.3}$$
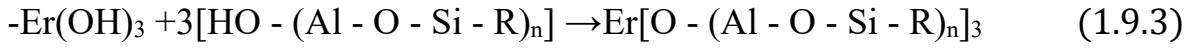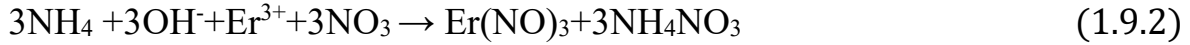
They observed that the lifetime of the samples prepared by modified synthesis route is longer than that of those prepared without Ammonium solution.

Alumina doped glasses show a strong tendency to retain hydroxyl groups in the densified matrix after heat treatment. Therefore, Aluminum codoping is less beneficial for near-infrared luminescing lanthanide ions than for lanthanide ions emitting in the visible spectral region. A less known codoping agent that improves the luminescent properties of lanthanide ions in sol-gel glasses is P$_2$O$_5$ [Binnemans 2009].

## 1.10 RE luminescence quenching by OH$^-$ groups

Planar optical waveguide amplifiers can integrate a plenty of active and passive optical elements reduced in the size and cost-efficient. The primary efforts of optical devices miniaturization has started with development of new Er$^{3+}$ -doped amplifiers. The cross section of the stimulated emission of RE ions is proportional to the RE ions concentration in the host matrix. Length reduction in planar optical waveguide amplifiers requires much higher Er$^{3+}$ concentrations than in the EDFAs to achieve sufficient absorption and high optical gain.

The use of lanthanide compounds is limited by their insolubility in apolar matrixes, which is connected with liquid-liquid immiscibility regions in the silica rich part of phase diagram. Molecular lanthanide complexes are soluble but they contain ligands with high energy vibrational modes, such as C-H or O-H functional groups. These groups can also invariably quench the RE luminescence.

Stretching vibration of O-H influence the fluorescence decay at 1.5 µm, two O-H bridge the gap at 6500 cm$^{-1}$ between the ground state, $^4I_{15/2}$ and the first excited state, $^4I_{13/2}$, of the Er$^{3+}$ ion [Stone 1996, Duverger 2001, Ebendorff-Heidepriem 1998,

Marques 2003]. The presence of OH species in the matrix leads to reduction of quantum efficiency at the first excited state of $Er^{3+}$ ions, and a limited process reproducibility.

The work of Marques et al. shows the fluorescence quenching of $Er^{3+}$-activated planar waveguides induced by OH species.

**Table 1.10.1.** PL quenching $80SiO_2$ - $20TiO_2$ - $0.5ErO_{1.5}$ waveguides as a function of different times of exposure to various atmospheres, following different heat treatment regimes [Marques 2003].

| Heat treatment parameters | Time of exposure | % PL quenching |
|---|---|---|
| 6 min at 670 °C in air | 6 days in lab atmosphere (air, RH ≈ 5 %,T≈ 21 °C) | 72 |
|  | 6 days in a desiccator charged with silica-gel | 28 |
|  | 6 days in a sealed container in liquid $N_2$ | 5 |
| 2 min at 700 °C in air | 5 days in a glove box (145 ppm$_{vol}$) | 17 |
| 7 min at 700 °C in air | 3 h in an ultrasonic water bath | 97 |
| 10 min 900 °C in air | 7 days in lab atmosphere (air) | 76 |
| 10 min 900 °C in vacuum | 7 days in lab atmosphere (air) | 34 |

They investigated PL spectra of the $^4I_{13/2} \rightarrow {}^4I_{15/2}$ transition and decay curves in $80SiO_2$ - $20TiO_2$ - $0.5ErO_{1.5}$ planar waveguides as a function of different times of exposure to various atmospheres. PL quenching obtained from the formula $\%decrease = \left(I_0^{1.5\,\mu m} - I_f^{1.5\,\mu m}\right)/I_0^{1.5\,\mu m}$, where $I_0^{1.5\,\mu m}$ and $I_f^{1.5\,\mu m}$ indicate the intensities at about 1.5 μm before and after the exposure. In the Table 1.10.1 indicated the 1/e fluores-

cence lifetimes, calculated as the 1/e decay time of the fluorescence intensity with the slow decay component lifetime (SDC).

**Table 1.10.2.** $Er^{3+}$ fluorescence lifetimes of $80SiO_2$-$20TiO_2$-$0.5ErO_{1.5}$ waveguide, prepared in different heat treatments in air and times of exposure to laboratory atmosphere [Marques 2003].

| Heat treatment of $80SiO_2$-$20TiO_2$-$0.5ErO_{1.5}$ waveguide | $\tau_{1/e}$ ($\pm$ 0.5 ms) | $\tau_{SDC}$ ($\pm$ 0.5 ms) |
|---|---|---|
| 40 days after a heat treatment of 25 min at 750 °C | 1.6 | 7.6 |
| 63 days after a heat treatment of 25 min at 750 °C | <1 | 4.3 |
| Additional heat treatment: 30 min at 200 °C | <1 | 4.6 |
| Additional heat treatment: 30 min at 400 °C | 3.5 | 6.6 |
| Additional heat treatment: 15 min at 900 °C | 6.6 | 7.2 |

These tables illustrate how spectroscopic properties of sol-gel samples can be modified by the fabrication protocol. Summarizing results from the Table 1.10.1 and Table 1.10.2 the increase of OH species in noncompletely densified system is associated with PL quenching process. The PL quenching is also attributed with the occurrence of a fast decay component (FDC) in the decay curves, while in fully densified system (HT at 900 °C for 15 min), the FDC is not present. Marques and al. explained the $Er^{3+}$ luminescence quenching by nonradiative de-excitation involving OH groups from atmospheric humidity, which interact with the $Er^{3+}$ ions present near the inner surface of pores in the sol-gel waveguides.

Moreover, high concentrations of $Er^{3+}$ ions initiate deleterious nonradiative energy exchanges between neighboring atoms [Ryu 1995, Orignac 1999]. Several of papers show that the OH - induced nonradiative relaxation is more effective at larger

Er$^{3+}$ concentrations [Hehlen 1997, Ishizaka 2002, Duverger 2001, Ebendorff-Heidepriem 1998, Houde-Walter 2001].

In bulk materials this effect is more prominent compared to thin films which allow a better densification with a lower amount of OH groups. Stable glass can be obtained under sufficient heat temperatures allowing elimination of any porosity and it has been suggested to use Aluminum oxide as efficient co-doping agent for reduction of OH concentration quenching [Iwasaki 1990, Fardad 1995, Orignac 1997, Pellegri 1998, Syms 1998, Seco 2000, Kinowski 2001, Harreld 2002, Yeatman 1999].

Starting from 1980s the study of ion-ion interactions resulting in concentration quenching in glasses have been the topic of several theoretical and experimental studies [Stokowski 1981, Miniscalco 1991, Blixt 1991, Federighi 1993, Nykolak 1993, Nykolak 1993, Snoeks 1996, Myslinski 1997, Philipsen 1997, Philipsen 1999, Maciel 2000, Ishizaka 2001, Feng 2001, Gonçalves 2002, Brecher 1976, Brecher 1980, Silversmith 2008, Hattori 1996].

As formerly it was discussed, the RE ions concentration is a critical parameter for planar waveguides in photonic applications. When RE concentration increase the average distance between Er$^{3+}$ ions decrease, and significance of electric dipole-dipole interactions between Er$^{3+}$ become more important. This results in process of energy migration and upconversion, which decline the fraction of excited Er$^{3+}$ ions at the related pump power is shown in the Equation 6. Decrease of the luminescence lifetime of the metastable $^4$I$_{13/2}$ state as a function of increasing Er$^{3+}$ concentration occurs, which described in the formula (Eq.6) [Stokowski 1981, Miniscalco 1991]:

$$\tau_{obs} = \frac{\tau_0}{1 + \left(\dfrac{\rho_{Er}}{Q}\right)^p} \tag{6}$$

where $\tau_{obs}$ is the observed luminescence lifetime, $\tau_0$ is the luminescence lifetime in the limit of zero RE concentration, $\rho_{Er}$ is the Er$^{3+}$ ion concentration, $Q$ is the quenching concentration and $p$ a phenomenological parameter characterizing the steepness of quenching curve. Phenomenological parameter p can be determined by the mecha-

nism of the energy transfer between the RE ions [Feng 2001]. At low RE doping level the electric dipole-dipole transition is the dominant energy transfer mechanism between $Er^{3+}$ ions, $p$ is close to 2. With increase of doping concentration the distance between $Er^{3+}$ becomes shorter, and the effect of electric dipole-and quadrupole-quadrupole transitions is important and $p$ is larger than 2.

Only Q is estimated from the fitting curve, at which concentration the lifetime becomes half of, because $\tau_{obs}$ is equal to half of $\tau_0$, when $\rho_{Er}$ is equal to $Q$. In the Equation 2, $\tau_0$ is the value of the PL lifetime of the RE ion in the material, in the limit of zero ion concentration. What means if the material has no multiphonon relaxation and if there no OH species, then then $\tau_0$ should approximately less than radiative lifetime $\tau_r$. The observed lifetime data performed on samples different from those obtained by sol gel route it is evident that for various measured lifetimes, different fitting parameters were obtained, in particular different concentration quenching parameter. Three different sets of measured lifetimes shown in the Figure 1.10.4 (a), considering a system characterized by a radiative lifetime of 3 and $\tau_0 = \tau_r$. The concentration quenching parameter Q is obtained using a parameter $p = 2$ for all the data, but different concentration quenching probabilities $Wcq$. Figure 1.10.4 (b) includes effect from OH groups. Considering the values of $Q = 1$, $p = 2$ and $\tau_r = 3$, with a different contribution of $W_{nr}$ (nonradiative process due to OH) groups: $W_{nr} = 0$, $0.1W_r$, $0.5W_r$, where the radiative transition probability $W_r$ is given by $\tau_r^{-1}$.

The total observed transition probability ($W_{obs}$) includes $W_{obs}=W_r+W_{cq}+W_{nr}$. After fitting with Eq. 2, the following parameters are obtained: $Q = 1$, $\tau_0 = 3$; $Q = 1.05$, $\tau_0 = 2.73$; $Q = 1.23$, $\tau_0 = 2$, for $W_{nr} = 0$, $0.1W_r$, and $0.5W_r$, respectively. The maximum observed variation of $Q$ was 23 %, when the estimated maximum variation of $\tau_0$ was about 33 %. The $W_{nr}$ giving a rise of $Q$ value at the low concentrations, because the lifetimes $\tau_0$ and $\tau_{obs}$ are strongly dependent on $W_{nr}$. Whereas $W_{cq}$ is dominant for high concentrations.
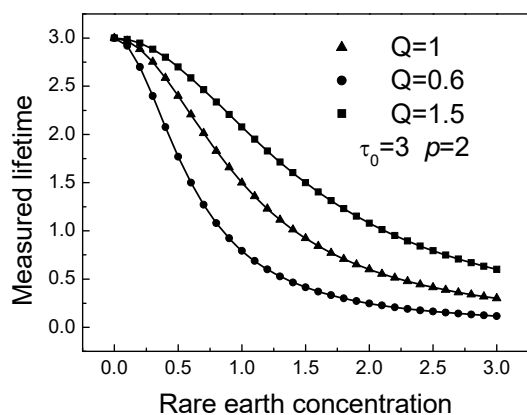
**Figure 1.10.4 (a).** Concentration quenching curves obtained for three different quenching probabilities, in the absence of processes other than Er-Er interactions.
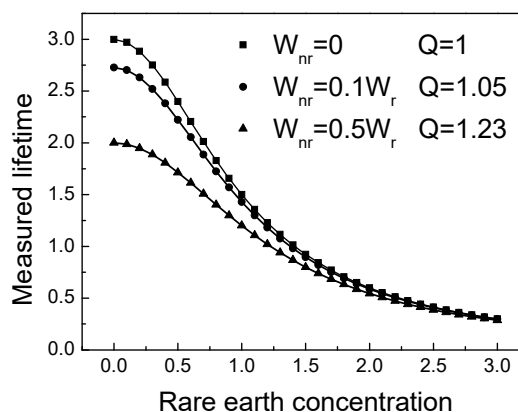
**Figure 1.10.4 (b.)** Concentration quenching curves obtained in the presence of different non-radiative contributions.

The use of Eq. 6 can be expressed in the Figure 1.10.5 of the measured lifetime of the metastable $^4I_{13/2}$ state of the $Er^{3+}$ ions, for $70SiO_2$ - $30HfO_2$ planar waveguides doped with 0.01, 0.03, 0.1, 0.3, 0.5, 1, 2, and 4 mol. % Er/(Si+Hf), respectively. The measured luminescence lifetime decreases with ion concentration increasing. The $70SiO_2$ - $30HfO_2$ system exhibits a higher quenching concentration than silicate glasses fabricated by melt-quenching technique.
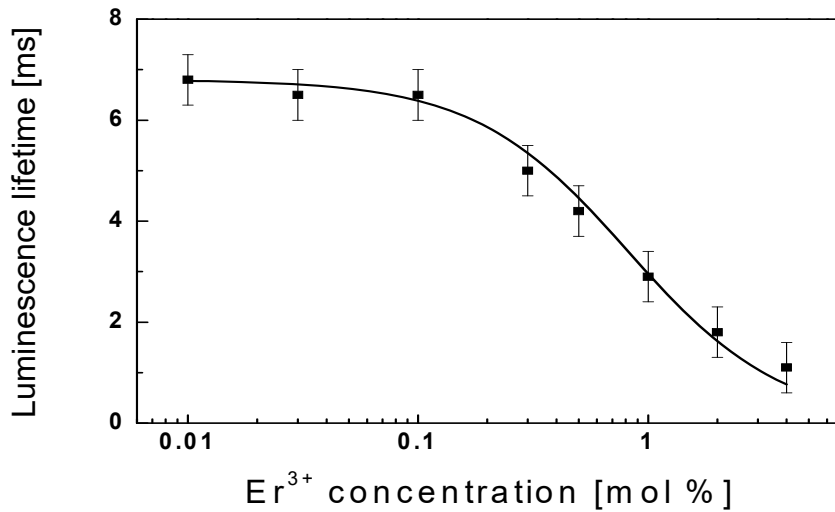
**Figure 1.10.5.** Luminescence lifetime of the $^4I_{13/2}$ metastable state for 70SiO$_2$ - 30HfO$_2$ planar waveguides doped with 0.01, 0.03, 0.1, 0.3, 0.5, 1, 2, and 4 mol. %. of the Er$^{3+}$ ions as a function of Er$^{3+}$ concentration.

However, the quenching concentration of 0.8 mol. % Er$^{3+}$ is higher than the value of 0.62 mol. % (p=1.27), reported for the 80SiO$_2$ - 20TiO$_2$ - AlO$_{3/2}$ system doped by Er/Yb [Orignac1999]. This can be explained that the introduction of hafnia in the silicate-oxygen network creates a non-bridging oxygens, enough for higher Er$^{3+}$ ions concentrations accommodated into the silicate network [Gonçalves 2002]. In the waveguide with the lowest Er$^{3+}$- doping level (0.01 mol. %), the lifetime is 6.7 ms. At this low concentration, no interaction between two or more Er$^{3+}$ ions occurs, so that, in the absence of OH, $\tau_0 = \tau_r$. Auzel and Goldner studied the self-quenching of Er$^{3+}$ ions in phosphate glass, the fluorophosphates and the tellurotungstate glasses with increase of Er$^{3+}$ doping concentration by fixing the reduction of the emission lifetime of $^4I_{13/2}$. The Er$^{3+}$ ions were introduced through Er$_2$O$_3$ or by the large minimum distance precursor ErP$_5$O$_{14}$ or NaEr(WO$_4$)$_4$. The obtained results show the improvement for large minimum distance precursors for fluorophosphates and tellurotungstate glasses. For phosphate glass no significant improvement was found. Comparing phosphate and fluorophosphate glass near-IR absorption spectra the fluorophosphate glasses contain less OH groups than phosphates one. The self-quenching mechanism in phosphate glasses is due to the energy diffusion by OH groups through

long distance Er-Er energy transfer more than through RE-RE clustering formation. Fluorophosphate glasses are well-known for their long lifetime of $Er^{3+}$ ions because during the glass preparation some of the hydroxyl groups undergo destruction through the following process [Auzel 2001]:

$$2(OH^-) + 2F^- = O_2 + HF \qquad (1.10.6)$$

## 1.11 Structural studies of the RE clustering

The standard technique for studying of RE ions clustering in sol-gel glasses is fluorescence line narrowing (FLN). This technique allows studying the local environment of lanthanide ions in glass matrix by observing of spectral fine structure even if emission bands in the luminescence spectra of glasses are broad. Inhomogeneous broadening can be eliminated because only a small amount of excited lanthanide ions are responsible for the broadening.

The difference in the crystal-field splitting pattern results in inhomogeneous spectral broadening of the emission bands that is explained that each RE ion in a glass is characterized by a slightly different local environment, resulting in slightly different crystal fields.

Using fluorescence line narrowing studies, only a small part of the lanthanides ions with a similar local environment are excited by a narrow laser line. Using this selective excitation of a part of the RE ions results in the elimination of inhomogeneous broadening. The luminescence spectra obtained by the FLN technique has a high resolution, and the fine structure in the luminescence spectra depends on the excitation energy. $Eu^{3+}$, $Nd^{3+}$, $Yb^{3+}$ are typical RE ions for FLN studies in glasses. For the selective excitation of a small portion of the lanthanide ions, the ions should be spatially separated. Selective excitation is not possible if the clustering is present. The small distance between the RE ions should be avoided because of the energy transfer processes between the neighboring ions [Binnemans 2009, Brecher 1976, Brecher 1980, Silversmith 2008].

## 1.12 The effect of P on the RE clustering in the glass matrix

Phosphorous pentoxide also can be used as codoping agent that improves the luminescent properties of RE ions in sol - gel glasses. Phosphate glass compared with silica have high $Er^{3+}$ ions solubility ($>1.2 \times 10^{21}$ ions/cm$^3$), low pumping power and a low cooperative upconversion coefficient of the $^4I_{11/2}$. Moreover, phosphates are most widely used for bulk laser glasses due to their low melting temperatures, good ultraviolet transmission and low dispersion. Phosphorous codoping is interesting because allows to induce larger emission cross sections and nonradiative energy transfers in Yb - Er codoped power amplifiers. Even at low $P_2O_5$ content ($<$ 1mol. %) the spectroscopic properties of $Nd^{3+}$ ions were also improved. It was proposed that Phosphorous co-dopants preferentially coordinate to $Nd^{3+}$ ions to form a solvation shell structure. Such ideas were reported two times for Erbium-activated optical fiber preforms fabricated by the Modified Chemical Vapor Deposition (MCVD) process [Binnemans 2009].

Some of the reports proposed to avoid any RE clustering by insertion of $Er^{3+}$ ions in a local ordered phase as $ErPO_4$. But the $Er^{3+}$ emission spectra in that case show broad emission bands what is typical for an amorphous matrix. Several results show that $P_2O_5$ codoping increases the gain of an $Er^{3+}$ $P_2O_5$ - $SiO_2$ planar waveguides. The refractive index was found to be proportional to the $P_2O_5$ concentration. The scattering loss of the waveguide with the low $P_2O_5$ cconcentration at 1.3 µm wavelength was higher than for the waveguide with the high concentration. That might be caused by the roughness of the etched sidewalls of the core. The increase of Phosphorous codoping at 1.49 µm can increase the absorption coefficient and fluorescence intensity. These investigations shows that Phosphorous codoping of $Er^{3+}$-activated $P_2O_5$ core glass affects the $Er^{3+}$ ions environment or the crystal field splitting, as well as intensities of the Stark transitions of $Er^{3+}$ ions. The $Er^{3+}$ ions environment is much influenced by surrounded $P^{5+}$ ions.

The SEM analysis shows that the glass with the high $P_2O_5$ concentration is more homogeneous than that with the low $P_2O_5$ content. The introduction of $P_2O_5$ can

increase RE ions solubility and their homogeneous distribution in silica-based glasses. From TEM study was observed the presence of spherical-shape clusters in the low-content $P_2O_5$ $Er^{3+}$ -doped silica glass. The diameter of these clusters were in average about 30-50 nm. In high-content $P_2O_5$ $Er^{3+}$-doped silica glass the microclusters were not detected. It was found that the concentration of $Er^{3+}$ and $P^{5+}$ in clusters were higher than in the glass matrix and they composed of $Er^{3+}$ and $P_2O_5$ rich phases in amorphous state. The reconstructed microscopic model presents the glass separated into two phases-cluster phase (rich of $Er^{3+}$ ions) and a matrix phase (glass). All the $Er^{3+}$ ions assumed to be incorporated in the clusters and to be optically active. The main difference for low and highly doped $P_2O_5$ silica glass is a difference in the size and density of $Er^{3+}$ ion rich phase. In highly $P_2O_5$ doped silica glass with more homogeneous $Er^{3+}$ ion distribution the average distance between $Er^{3+}$ ions is considered to be larger than for low-concentrated $P_2O_5$-$SiO_2$ glass. In the case of homogeneous glass the average distance between the $Er^{3+}$ is at an acceptable maximum and the rate of the upconversion energy transfer is shrinked. Assuming this hypothesis the homogeneous upconversion in the $Er^{3+}$ rich phase dominate the amplification process [Hattori 1996].

Jiin-Jyh Shyu et al. noticed that for $Er_2O_3$ content $\leq$ 2 mol. % the samples are amorphous. When the $Er_2O_3$ content is $\geq$ 4 mol. %, $Er_2O_3$ reacts almost completely with $P_2O_5$ with formation of $ErPO_4$ crystalline particle. $ErPO_4$ particles are crystallized during the glass quenching process and are homogeneously distributed in the $SnO_2$-$P_2O_5$ glass. Formation of $ErPO_4$ increases the absorption cross-section of the $Er^{3+}$ ions. The Er-Er distance in the crystallized glass is shorter than in in which $Er^{3+}$ ions are homogeneously distributed, the photoluminescence intensity increases with increasing of the crystallized $ErPO_4$ phase. The typical reduction of the PL in heavily doped materials does not happen due to the constant Er-Er distance in $ErPO_4$ allow not occurring the reduction of the PL [Binnemans 2009].

P-codoping improve also the spectroscopic properties of $Nd^{3+}$ ions in optical fiber preforms even at low $P_2O_5$ content (< 1 mol. %). Phosphorous codoping prefe-

rentially coordinate to $Nd^{3+}$ ions forming in such a way a solvation shell structure. In some reports about $Er^{3+}$ incorporation in the ordered phase such as $ErPO_4$ that can avoid any RE ions clustering [Binnemans 2009].

Brandel et al. prepared phosphate gels as a host for RE ions. The phosphate gels were doped with Thorium. Drying of a concentrated Thorium phosphate gels at room temperature led to the formation a transparent xerogel with a good optical quality. The luminescence properties of $Eu^{3+}$ in Thorium-based gels and xerogels were studied. Codoping of Thorium xerogels with Coumarin-460 and $Tb^{3+}$ ion resulting in an enhancement of the $Tb^{3+}$ luminescence. Coumarin 460 was used to sensitize $Eu^{3+}$ luminescence in a Thorium phosphate xerogels [Brandel 2001, Genet 1990A].

# Bibliography

[Adachi 1988] Adachi, T.; Sakka, S. "The role of N,N- dimethylformamide, a DCCA in the formation of silica-gel monoliths by sol-gel method", J. Non-Cryst. Solids, 99 (1988), pp. 118-128

[Almeida 1998] Almeida, R.M.; Vasconcelos, H.C.; Gonçalves, M.C.; Santos, L.F. "XPS and NEXAFS studies of rare-earth doped amorphous sol-gel films", J. Non-Cryst. Solids, 232 (1998), pp. 65-71

[Arai 1986] Arai, K.; Namikawa, H.; Kumata, K.; Honda, T.; Ishii, Y.; Handa, T. "Aluminum or phosphorus co-doping effects on the fluorescence and structural properties of neodymium doped silica glass", J. Appl. Phys., 59 (1986), pp. 3430-3436

[Armellini 1999] Armellini, C.; Ferrari, M.; Montagna, M.; Pucker, G.; Bernard, C.; Monteil, A. "Terbium (III) doped silica-xerogels: effect of aluminium (III) co-doping", J. Non-Cryst. Solids, 245 (1999), pp. 115-121

[Auzel 1966] Auzel, F. "Compteur quantique par transfert d'énergie entre deux ions de terres rares dans un tungstate mixte et dans un verre", C.R. Acad. Sci. Paris, (262) 1966, pp. 1016-1019

[Auzel 1994] Auzel, F.; Meichenin, D.; Pelle, F.; Goldner P. "Cooperative luminescence as a defining process for RE-ions clustering in glasses and crystals", Opt. Mater., 4 (1994), pp. 35-41

[Auzel 2001] Auzel, F.; Goldner, P. "Towards rare-earth clustering control in doped glasses", Optical Materials, 16 (2001), pp. 93-103

[Benatsou 1997] Benatsou, M.; Capoen, B.; Bouazaoui, M.; Tchana, W.; Vilcot, J.P. "Preparation and characterization of sol-gel derived Er3-$SiO_2$ planar waveguides ($Al_2O_3$)", Appl. Phys. Lett., 71 (1997), pp. 428-430

[Bhaumik 1964] Bhaumik, M.L. "Quenching and temperature dependence of fluorescence in rare-earth chelates", J.Chem.Phys., 40 (1964), pp. 3711-3715

[Binnemans 2009] Binnemans K. "Lanthanide-based luminescent hybrid materials", Chem.Rev., 109 (2009), pp. 4283-4374

[Biswas 1994] Biswas, A.; Acharya, H.N.; Das, B.N. "Nd-doped silica glasses by sol-gel method-effect of aluminum co-doping", Indian Journal of Pure & Applied Physics, 32 (1994), pp. 358-360

[Biswas 2000] Biswas, A.; Friend, C.S.; Maciel, G.S.; Prasad, P.N. "Optical properties of Europium doped gels during densification", J. Non-Cryst. Solids, 261 (2000), pp. 9-14

[Blixt 1991] Blixt, P.; Nilsson, J.; Carlnäs, T.; Jaskorzynska B. "Concentration- dependent upconversion in $Er^{3+}$-doped fiber amplifiers: Experiments and modeling", IEEE Transact. Photon. Technol. Lett., 3 (1991), pp. 996-998

[Brandel 2001] Brandel, V.; N. Dacheux, N.; M. Genet, M. "Studies on the Chemistry of Uranium and Thorium Phosphates. Thorium Phosphate Diphosphate: A Matrix for Storage of Radioactive Wastes", Radiochemistry, 43(2001), pp. 16-23

[Brecher 1976] Brecher, C.; Riseberg, L. A. "Laser-induced fluorescence line narrowing in Eu glass: a spectroscopic analysis of coordination structure", Phys. ReV. B, 13 (1976), pp. 81-93

[Brecher 1980] Brecher, C.; Riseberg, L. A. "Laser-induced line narrowing of $Eu^{3+}$ fluorescence in fluoroberyllate glass: site-dependent spectroscopic properties and their structural implications", Phys. ReV. B, 21 (1980), pp. 2607-2618

[Bredol 1998] Bredol, M.; Kynast, U.; Boldhaus, M.; Lau, C. "Luminescent inorganic networks", Ber. Bunsen-Ges., 102 (1998), pp. 1557-1560

[Bredol 2002] Bredol, M.; Gutzov, S. "Effect of Germanium codoping on the luminescence of Terbium doped silica xerogels", Opt. Mater., 20 (2002), pp. 233-239

[Bredol 2003] Bredol, M.; Gutzov, S.; Jüstel, T. "Highly efficient energy transfer from Ge-related defects to $Tb^{3+}$ ions in sol-gel derived Glasses", J. Non-Cryst Solids, 321 (2003), pp. 225-230

[Bucella 2004] Bucella, S.; Riello, P.; Scremin, B.F.; Calvelli, P.; Polloni, R.; Speghini, A.; Bettinelli, M.; Benedetti, A. "Synthesis and luminescence proper-

ties of $ZrO_2$ and $ZrO_2/SiO_2$ composites incorporating Eu(III)-phenanthroline complex prepared by a catalyst-free sol-gel process", Opt. Mater., 27 (2004), pp. 249-255

[Carnall 1968] Carnall W.T.; Fields P.R; Rajnak K. "Electronic Energy Levels in the Trivalent Lanthanide Aquo Ions. I. $Pr^{3+}$, $Nd^{3+}$, $Pm^{3+}$, $Sm^{3+}$, $Dy^{3+}$, $Ho^{3+}$, $Er^{3+}$, and $Tm^{3+}$", J.Chem. Phys., 49 (1968), pp. 4424-4442

[Chacon-Roa 2008] Chacon-Roa, C.; Guzman-Mendoza, J.; Aguilar-Frutis, M.; Garcia-Hipolito, M.; Alvarez-Fragoso, O.; Falcony, C. "Characterization of luminescent samarium doped $HfO_2$ coatings synthesized by spray pyrolysis technique", J. Phys. D, 41 (2008), pp. 015104.1-015104.7

[Chakrabarti 1994] Chakrabarti, S.; Sahu, J.; Chakraborty, M.; Acharya, H. N. "Monophasic silica glasses with large neodymia concentration", J. Non-Cryst. Solids, 180 (1994), pp. 96-101

[Chapter_11] http://131.104.156.23/Lectures/331/331_Chapter_11.html

[Chen 2008] Chen, F.F.; Bian, Z.Q.; Lui, Z.W.; Nie, D.B.; Chen, Z.Q.; Huang, C.H. "Highly efficient sensitized red emission from europium (III) in Ir-Eu bimetallic complexes by 3MLCT energy transfer", Inorg. Chem., 47( 2008), pp. 2507-2513

[Chiasera 2003] Chiasera, A.; Montagna, M.; Rolli, R.; Ronchin, S.; Pelli, S.; Righini, G.C.; Gonçalves, R.R.; Messaddeq, Y.; Ribeiro, S.J.L.; Armellini, C.; Ferrari, M.; Zampedri, L. "$Er^{3+}/Yb^{3+}$ Co-Activated Silica-Alumina Monolithic Xerogels", J. Sol-Gel Sci. Tech., 26 (2003), pp. 943-946

[Ciuffi 2002] Ciuffi, K.J.; de Lima, O.J.; Sacco, H.C.; Nassar, E.J. "$Eu^{3+}$ entrapped in alumina matrix obtained by hydrolytic and non-hydrolytic sol-gel routes", J. Non-Cryst. Solids, 304 (2002), pp. 126-133

[Coutier 2000] Coutier, C.; Audier, M.; Fick, J.; Rimet, R.; Langlet, M. "Aerosol-gel preparation of optically active layers in the system $Er/SiO_2-TiO_2$", Thin Solid Films, 372 (2000), pp. 177-189

[Crosby 1961] Crosby G.A.; Whan R.E.; Alire R.M. "Lanthanide acetylacetonates, energy transfer to triplet states of the ligands", J.Chem.Phys., 34 (1961), pp. 743-748

[Crosby 1962] Crosby G.A.; Whan R.E., Freeman J.J. "Spectroscopic studies of rare earth chelates" J. Phys. Chem., 66 (1962), pp. 2493-2499

[Denker 1981] Denker, B.I.; Osiko, V.V.; Pashinin P.P.; Prokhorov, A.M. "Concentrated neodymium laser glasses (review)", Sov.J.Quantum Electron., 11 (1981), pp. 289-297

[Duverger 2001] Duverger, C.; Montagna, M.; Rolli, R.; Ronchin, S.; Zampedri, L.; Fossi, M.; Pelli, S.; Righini, G.C.; Monteil, A.; Armellini, C.; Ferrari, M. "Erbium-activated silica xerogels: spectroscopic and optical properties", J. Non-Cryst. Solids, 280 (2001), pp. 261-268

[Eaton 1988] Eaton, D.F. "Reference materials for fluorescence measurements", Pure Appl.Chem., 60 (1988), pp. 1107-1114

[Ebendorff-Heidepriem 1998] Ebendorff-Heidepriem, H.; Ehrt D. "Relationship between local structure of glasses and spectroscopic properties of $Eu^{3+}$ and $Tb^{3+}$ ions", Glasstech. Ber. Glass. Sci. Technol., 71(1998), pp. 289-299

[Fardad 1995] Fardad, M.A.; Yeatman, E.M.; Dawnay, E.J.C.; Green, M.; Horowitz, F. "Effects of $HfO_2$ on structure of acid-catalysed $SiO_2$ sol-gel films", J. Non-Cryst. Solids, 183 (1995), pp. 260-267

[Federighi 1993] Federighi, M.; Massarek, I.; Trwoga, P.F. "Optical amplification in thin optical waveguides with high Er concentration", IEEE Photon. Technol. Lett., 5 (1993), pp. 227-229

[Feng 2001] Feng, X.; Tanabe, S.; Hanada, T. "Spectroscopic properties of erbium-doped ultraphosphate glasses for 1.5 μm amplification", J. Appl. Phys., 89 (2001), pp. 3560-3567

[Fery-Forgues 1999] Fery-Forgues, S.; Lavabre, D.J. "Are fluorescence quantum yields so tricky to measure? A demonstration using familiar stationery products", J. Chem.Educ., 76 (1999), pp. 1260-1264

[Gapotenko 2001] Gaponenko, N.V.; Sergeev, O.V.; Stepanova, E.A.; Parkun, V.M.; Mudryi, A.V.; Gnaser, H.; Misiewicz, J.; Heiderhoff, R.; Balk, L.J.; Thompson, G.E. "Optical and structural characterization of erbium-doped $TiO_2$ xerogel films processed on porous anodic alumina", J. Electrochem. Soc., 148 (2001), pp. H13-H16

[Genet 1990A] Genet, M.; Brandel, V.; Lahalle, M. P.; Simoni, E. "Transparent gel and xerogel of thorium phosphate. Optical spectroscopy with: $Nd^{3+}$, $Er^{3+}$, $Eu^{3+}$, $Cr^{3+}$ and rhodamine 6G", Proc. SPIE, 1328 (1990), pp.194-200

[Genet 1990B] Genet, M.; Brandel, V.; Lahalle, M. P.; Simoni, E. C. R. "Mise en evidence d'un transfert d'energie electronique entre la coumarine 460 et $Eu^{3+}$ dans le xerogel de phosphate de thorium", Acad. Sci. II, 311 (1990), pp. 1321-1325

[Gerasimova 2006] Gerasimova, V.I.; Zavorotnyi, Y.S.; Rybaltovskii, A.O.; Lemenovskii, D.A.; Timofeeva, V.A. "Photosensitivity of nanoporous glasses and polymers doped with Eu(fod)(3) molecules", Quantum Electron., 36 (2006), pp. 791-796

[Gonçalves 2002] Gonçalves, R.R.; Carturan, G.; Zampedri, L.; Ferrari. M.; Montagna, M.; Chiasera, A.; Righini, G.C.; Pelli, S.; Ribeiro, S.J.L.; Messaddeq,Y. "Sol-gel Er-doped $SiO_2$-$HfO_2$ planar waveguides: a viable system for 1.5 µm application", Appl. Phys. Lett., 81 (2002), pp. 28-30

[Goncalves 2004] Goncalves, R.R.; Carturan, G.; Montagna, M.; Ferrari, M.; Zampedri, L.; Pelli, S.; Righini, G.C.; Ribeiro, S.J.L.; Messaddeq,Y. "Erbium-activated $HfO_2$-based waveguides for photonics", Opt. Mat., 25 (2004), pp. 131-139

[Gudmundson 1963] Gudmundson, R.A.; Marsh, O.J.; Matovich, E. "Fluorescence of Europium Thenoyltrifluoroacetonate. II. Determination of Absolute Quantum Efficiency", J.Chem.Phys., 39 (1963), pp. 272-274

[Gutzov 2006] Gutzov, S.; Bredol, M. "Preparation and luminescence of terbium and cerium-doped silica xerogels", J. Mater. Sci. 41 (2006), pp. 1835-1837

[Haas 1971] Haas, Y.; Stein, G. "Pathways of radiative and radiationless transitions in europium (III) solutions. Role of solvents and anions", J.Phys.Chem., 75 (1971), pp. 3668-3677

[Hao 1999] Hao, X.P.; Fan, X.P.; Wang, M.Q. "Luminescence behavior of Eu(TTFA)(3) doped sol-gel films", Thin Solid Films, 353 (1999), pp. 223-226

[Harreld 2002] Harreld, J.H.; Ebina, T.; Tsubo, N.; Stucky, G. "Manipulation of pore size distributions in silica and ormosil gels dried under ambient pressure conditions", J. Non-Cryst. Solids, 298 (2002), pp. 241-251

[Hattori 1996] Hattori, K.; Kitagawa, T.; Oguma, M.; Okazaki, H.; Ohmori, Y. "Optical amplification in $Er^{3+}$-doped $P_2O_5$-$SiO_2$ planar waveguides", Journal of Applied Physics, 9 (1996), pp. 5301-5308

[Hazenkamp 1990] Hazenkamp, M.F.; Blasse, G. "Rare-earth ions adsorbed onto porous glass: luminescence as a characterizing tool", Chem. Mater., 2 (1990), pp. 105-110

[Hebbink 2002] Hebbink, G.A.; Klink, S.I.; Grave, L.; Alink, P.G. B.O.; van Veggel, F.C.J.M. "Singlet Energy Transfer as the Main Pathway in the Sensitzation of Near-Infrared $Nd^{3+}$ Luminescence by Dansyl and Lissamine Dyes", ChemPhysChem., 3 (2002), pp. 1014-1018

[Hehlen 1997] Hehlen, M.P.; Cockroft, N.J.; Gosnell, T.R. "Spectroscopic properties of $Er^3$-doped and $Yb^{3+}$-doped soda-lime silicate and aluminosilicate glasses", Rev. B, 59 (1997), pp. 9302-9318

[Houde-Walter 2001] Houde-Walter, S.N.; Peters, P.M.; Stebbins, J.F.; Zeng, Q. "Hydroxyl-contents and hydroxyl-related concentration quenching in erbium-doped aluminophosphate, aluminosilicate and fluorosilicate glasses", J. Non-Cryst. Solids, 286 (2001), pp. 118-131

[Ishizaka 2001] Ishizaka, T.; Kurokawa, Y. "Preparation conditions and optical properties of rare earth ion ($Er^{3+}$ and $Eu^{3+}$)-doped alumina films by the aqueous sol-gel method", Appl. Phys., 90 (2001), pp. 243-247

[Ishizaka 2002] Ishizaka, T.; Nozaki, R.; Kurokawa, Y. "Luminescence properties of Tb$^{3+}$ and Eu$^{3+}$-doped alumina films prepared by sol-gel method under various conditions and sensitized luminescence", J. Phys. Chem. Solids, 63 (2002), pp. 613-617

[Iwasaki 1990] Iwasaki, M.; Yasumori, A.; Kawazoe, H.; Yamane, M. "Thermal properties of gel-derived materials of $Al_2O_3$-$SiO_2$", J. Non-Cryst. Solids, 121 (1990), pp. 147-152

[Jia 2006] Jia, C.W.; Xie, E.Q.; Peng, A.H.; Jiang, R.; Ye, F.; Lin, H.F.; Xu, T. "Photoluminescence and energy transfer of terbium doped titania film", Thin Solid Films, 496 (2006), pp. 555-559

[Jin 2000] Jin, J.; Sakida, S.; Yoko, T.;Nogami, M. "The local structure of Sm-doped aluminosilicate glasses prepared by sol-gel method", J. Non-Cryst. Solids, 262 (2000), pp. 183-190

[Kiisk 2005] Kiisk, V.; Sildos, I.; Lange, S.; Reedo, V.; Tatte, T.; Kirm, M.; Aarik, J. "Photoluminescence characterization of pure and Sm$^{3+}$-doped thin metaloxide films", Applied Surface Science, 247 (2005), pp. 412-417

[Kim 2001] Kim, T.; Yoon, Y.; Kil, D.; Hwang, Y.; Chung, H.; Kim, I. N.;Ahn, Y. "Effects of surrounding ion on Eu$^{3+}$ luminescence in glass", Mater. Lett., 47 (2001), pp. 290-296

[Kinowski 2001] Kinowski, C.; Bouazaoui, M.; Bechara, R.; Hench, L.L.; Nedelec, J.M.; Turrell, S. "Kinetics of densification of porous silica gels: a structural and textural study", J. Non-Cryst. Solids, 291 (2001), pp. 143-152

[Kleinerman 1964] Kleinerman, M. "Intramolecular energy transfer in lanthanide chelates", Bull.Am.Phys.Soc., 9 (1964), pp. 265-273

[Kojima 2000] Kojima, K.; Tsuchiya, K.; Wada, N. "Sol-gel synthesis of Nd3+-doped $GeO_2$ glasses and their optical properties", Sol-Gel Sci. Technol., 19 (2000), pp. 511-514

[Koslova 1993] Koslova, N.I.; Viana, B.; Sanchez, C. "Rare-earth-doped hybrid si-loxane-oxide coatings with luminescent properties", J. Mater. Chem., 3 (1993), pp. 111-112

[Kurokawa 1994] Kurokawa, Y.; Kobayashi, Y.; Nakata, S. "Preparation of transparent alumina films by the sol-gel process and its application to photo functional films", Heterogeneous Chemistry Reviews, 1 (1994), pp. 309-328

[Kurokawa 1998] Kurokawa, Y.; Ishizaka, T.; Ikoma, T.; Tero-Kubota, S. "Photo-properties of rare earth ion ($Er^{3+}$, $Eu^{3+}$ and $Sm^{3+}$)-doped alumina films prepared by the sol-gel method", Chem. Phys.Lett., (287) 1998, pp. 737-741

[Laegsgaard 2002] Laegsgaard, J.L. "Dissolution of rare-earth clusters in $SiO_2$ by Al codoping: A microscopic model", Phys.Rev., B 65 (2002), p.1174114

[Lazarides 2008A] Lazarides, T.; Sykes, D.; Faulkner, S.; Barbieri, A.; Ward, M.D. "On the mechanism of d-f energy-transfer in RuII/LnIII and OsII/LnIII dyads: Dexter-type energy-transfer over a distance of 20 Å", Chem.- Eur. J., 14 (2008), pp. 9389-9399

[Lazarides 2008B] Lazarides, T.; Adams, H.; Sykes, D.; Faulkner, S.; Calorego, G.; Ward, M.D. "Heteronuclear bipyrimidine-bridged Ru-Ln and Os-Ln dyads: low-energy 3MLCT states as energy-donors to Yb(III) and Nd(III)", Dalton Trans., 5 (2008), pp. 691-698

[Lecomte 1991] Lecomte, M.; Viana, B.; Sanchez, C. "Propriétés optiques de sondes organiques (rhodamine 6G, coumarine 4) et inorganiques (Eu (III), Nd (III)) dans les gels à base d'oxyde de métaux de transitions", J. Chim. Phys., 88 (1991), pp. 39-53

[Li 2000] Li, H.; Inoue, S.; Machida, K.; Adachi, G. "Preparation and luminescence properties of inorganic-organic hybrid materials doped with lanthanide (III) complexes", J. Lumin., 87 (2000), pp. 1069-1072

[Lochhead 1994] Lochhead, M.J.; Bray, K.L. "Time-resolved fluorescence line - nar-rowing and lifetime studies of gel-derived $Eu_2O_3$-$Al_2O_3$-$SiO_2$ systems", SPIE, 2288 (1994), pp. 688-699

[Lochhead 1995] Lochhead, M.J.; Bray, K.L. "Rare-earth clustering and aluminum codoping in sol-gel silica-investigation using europium (iii) fluorescence spectroscopy", Chem. Mater., 7 (1995), pp. 572-577

[Maciel 2000] Maciel, G.S.; Biswas, A.; Kapoor, R.; Prasad, P.N. "Blue cooperative upconversion in $Yb^{3+}$-doped multicomponent sol-gel-processed silica glass for three-dimensional display", Appl. Phys. Lett., 76 (2000), pp. 1978-1980

[Mack 1983] Mack, H.; Resifeld, R.; Avnir, D. "Fluorescence of Rare Earth Ions Adsorbed on Porous Vycor Glass", Chem. Phys. Lett., 99 (1983), pp. 238-239

[Malashkevich 2002] Malashkevich, G.E.; Semkova, G.I.; Strek, W. "Influence of preparation redox conditions and composition of Ce-containing silica gel-glass on its absorption spectrum in the visible region", Journal of Alloys and Compounds, 341 (2002), pp. 244-246

[Malashkevich 2004] Malashkevich, G.E.; Semkova, G.I.; Stupak, A.P.; Sukhodolov, A.V. "Silica gel glasses with a high efficiency of luminescence sensitization in the $Ce^{3+}$-$Tb^{3+}$ system", Phys. Solid State, 46 (2004), pp. 1425-1431

[Marques 2003] Marques, A.C.; Almeida, R.M.; Chiasera, A.; Ferrari, M. "Reversible photoluminescence quenching in $Er^{3+}$-doped silica-titania planar waveguides prepared by sol-gel", J. Non-Cryst. Solids, 322 (2003), pp. 272-277

[Martin 2001] Martin, I.R.; Yanes, A.C.; Mendez-Ramos, J.; Torres, M.E.; Rodriguez, V.D. "Cooperative energy transfer in $Yb^{3+}$-$Tb^{3+}$ codoped silica sol-gel glasses", J. Appl. Phys., 89 (2001), pp. 2520-2524

[Matthews 1993] Matthews, L.R.; Knobbe, E.T. "Luminescence behavior of europium complexes in sol-gel derived host materials", Chemistry of materials, 5 (1993), pp. 1697-1700

[Matthews 1994] Matthews, L.R.; Wang, X.J.; Knobbe, E.T. "Concentration effects on the luminescence behavior of europium (III) chloride- and organoeuropium-doped silicate gels", J. Non-Cryst. Solids, 178 (1994), pp. 44-51

[Miniscalco 1991] Miniscalco, W.J. "Erbium-doped glasses for fiber amplifiers at 1500 nm", J. Lightwave Technol., 9 (1991), pp. 234-250

[Misra 2008] Misra, V.; Mishra, H. "Photoinduced proton transfer coupled with energy transfer: Mechanism of sensitized luminescence of terbium ion by salicylic acid  doped in polymer", J.Chem.Phys., 128 (2008), pp. 244701-1-244701-8

[Myslinski 1997] Myslinski, P.; Nguyen, D.; Chrostowski, J. "Effects of concentration on the performance of erbium-doped fiber amplifiers", J. Lightwave Technol., 15 (1997), pp. 112-120

[Nogami 1996] Nogami, M.; Abe, Y. "Properties of sol-gel derived $Al_2O_3$ - $SiO_2$ glasses using $Eu^{3+}$", J. Non-Cryst. Solids, 197 (1996), pp. 73-78

[Nogami 1997] Nogami, M.; Abe, Y. "Fluorescence spectroscopy of silicate-glasses codoped with $Sm^{2+}$ and $Al^{3+}$ ions", Appl. Phys., 81 (1997), pp. 6351-6356

[Nogami 2000] Nogami, M.; Nagakura, T.; Hayakawa, T. "Site-dependent fluorescence and hole-burning spectra of $Eu^{3+}$-doped $Al_2O_3$-$SiO_2$ glasses", Lumin., 86 (2000), pp. 117-123

[Nykolak 1993] Nykolak, G.; Becker, P.C.; Shmulovich, J.; Wong, Y.H.; Di Giovanni, D.J.; Bruce, A.J. "Concentration-dependent $^4I_{13/2}$ lifetimes in $Er^{3+}$-doped fibers and $Er^{3+}$-doped planar waveguides", IEEE Phot. Technol. Lett., 5 (1993), pp. 1014-1016

[Orignac 1997] Orignac, X.; Vasconcelos, H.C.; Du, X.M.; Almeida, R.M. "Influence of solvent concentration on the microstructure of $SiO_2$-$TiO_2$ sol-gel films", J. Sol-Gel Sci. and Technol., 8 (1997), pp. 243-248

[Orignac 1999] Orignac, X.; Barbier, D.; Du, X. M.; Almeida, R.M.; McCarthy, O.; Yeatman, E. "Sol-gel silica/titania-on-silicon Er/Yb-doped waveguides for optical amplification at 1.5 μm," Opt. Mater., 12 (1999), pp.1-18

[Otto 2000] Otto, A.P.; Brewer, K.S.; Silversmith, A.J. "Red to blue upconversion in Tm-doped sol-gel silicate glasses", J.Non-Cryst. Solids, 265 (2000), pp. 176-180

[Palomino-Merino 2001] Palomino-Merino, R.; Conde-Gallardo, A.; Garcia-Rocha, M.; Hernandez-Calderon, I.; Castano, V.; Rodriguez, R. "Photoluminescence of $TiO_2$: $Eu^{3+}$ thin films obtained by sol-gel on Si and Corning glass substrates", Thin Solid Films, 401 (2001), pp. 118-123

[Pasquale 1995] Pasquale, F.D.; Federighi, M.J. "Modelling of Uniform and Pair-Induced Upconversion Mechanisms in High-Concentration Erbium-Doped Silica Waveguides", Lightwave Technol., 13(1995), pp. 1858-1864

[Pellegri 1998] Pellegri, N.; Dawnay, E.J.C.; Yeatman, E.M. "Multilayer $SiO_2$-$B_2O_3$-$Na_2O$ films on Si for optical applications", J. Sol- Gel Sci. and Technol., 13 (1998), pp. 783-787

[Philipsen 1997] Philipsen, J.L.; Bjarklev, A. "Monte Carlo simulations of homogeneous upconversion in erbium-doped silica glasses", IEEE J. Quant. Electr., 33 (1997), pp. 845-854

[Philipsen 1999] Philipsen, J.L.; Broeng, J.; Bjarklev, A.; Helmfrid, S.; Bremberg, D.; Jaskorzynska, B.; Pálsdóttir, B. "Observation of strongly nonquadratic homogeneous upconversion in $Er^{3+}$-doped silica fibers and reevaluation of the degree of clustering", IEEE J. Quant. Electr., 35 (1999), pp. 1741-1749

[Pucker 1998] Pucker, G.; Parolin, S.; Moser, E.; Montagna, M.; Ferrari, M.; Del Longo, L. "Raman and luminescence studies of $Tb^{3+}$ doped monolithic silica xerogels", Spectrochimica Acta Part A, 54 (1998), pp. 2133-2142

[Qian 1997] Qian, G.D.; Wang, M.Q.; Wang, M.; Fan, X.P.; Hong, Z.L. "Synthesis in-situ of 2,2'-dipyridyl-tb(iii) complexes in silica-gel", J. Mater. Sci. Lett., 16 (1997), pp. 322-323

[Quimby 1994] Quimby, R.S.; Miniscalco, W.J.; Thompson, B. "Clustering in erbium-doped silica glass fibers analyzed using 980-nm excited-state absorption", J. Appl. Phys., 76 (1994), pp. 4472-4478

[Reisfeld 2000] Reisfeld, R.; Zelner, M.; Patra, A. "Fluorescence study of zirconia films doped by $Eu^{3+}$, $Tb^{3+}$, and $Sm^{3+}$", J. Alloys Compd., 300 (2000), pp. 147-151

[Reisfeld 2001] Reisfeld, R.; Saraidarov, T.; Pietraszkiewicz, M.; Lis, S. "Luminescence of europium(III) compounds in zirconia xerogels", Chem. Phys.Lett., 349 (2001), pp. 266-270

[Reisfeld 2003] Reisfeld, R.; Saraidarov, T.; Gaft, M.; Pietraszkiewicz, M.; Pietraszkiewicz, O.; Bianketti, S. "Rare earth ions, their spectroscopy of cryptates and related complexes in sol-gel glasses", Opt. Mater., 24 (2003), pp. 1-13

[Rocca 2001] Rocca, F.; Ferrari, M.; Kuzmin, A.; Dal Dosso, N.; Duverger, C.; Monti, F. "EXAFS studies of the local structure of $Er^{3+}$ ions in silica xerogels co-doped with aluminium", J. Non-Cryst. Solids, 293 (2001), pp. 112-117

[Ronson 2005A] Ronson, T.K.; Lazarides, T.; Adams, H.; Pope, S.J.A.; Sykes, D.; Faulkner, S.; Coles, S.J.; Hursthouse, M.B.; Clegg, W.; Harrington, R.W.; Ward, M.D. "Luminescent Pt(II)(bipyridyl)(diacetylide) chromophores with pendant binding sites as energy donors for sensitised near-infrared emission from lanthanides: structures and photophysics of Pt(II)/Ln(III) assemblies", Chem.-Eur. J., 12 (2005), pp. 9299-9313

[Ryu 1995] Ryu, C.K.; Choi, H.; Kim, K. "Fabrication of highly concentrated Er3-gel processing (doped aluminosilicate films via sol)", Appl. Phys. Lett., 66 (1995), pp. 2496-2498

[Sahu 1996] Sahu, J.; Biswas, A.; Chakrabarti, S.; Acharya, H. N. "Studies on Nd-doped colloidopolymeric silica xerogel", J. Non-Cryst. Solids, 197 (1996), pp. 129-135

[Seco 2000] Seco, A.M.; Gonçalves, M.C.; Almeida, R.M. "Densification of hybrid silica-titania sol-gel films studied by ellipsometry and FTIR", Mater. Science Engin. B, 76 (2000), pp. 193-199

[Sen 2000] Sen, S. "Atomic environment of high-field strength Nd and Al cations as dopants and major components in silicate glasses: a Nd L III-edge and Al K-edge X-ray absorption spectroscopic study", J. Non-Cryst. Solids, 261 (2000), pp. 226-236

[Shavaleev 2003] Shavaleev, N.M.; Moorcraft, L.P.; Pope, S.J.A.; Bell, Z.R.; Faulkner, S.; Ward, M.D. "Sensitised near-infrared emission from lanthanides using a covalently-attached Pt(II) fragment as an antenna group", Chem.Commun., (2003), pp. 1134-1135

[Silversmith 2008] Silversmith, A. J.; Nguyen, N. T. T.; Sullivan, B. W.; Boye, D. M.; Ortiz, C.; Hoffman, K. R. "Rare-earth ion distribution in sol-gel glasses co-doped with $Al^{3+}$", J. Lumin., 128 (2008), pp. 931-933

[Snoeks 1996] Snoeks, E.; van den Hoven, G.N.;  Polman, A. "Measuring and modifying the spontaneous emission rate of erbium near an interface",  IEEE J. Quant. Elect., 32 (1996), pp. 1680-1684

[Stokowski 1981] Stokowski, S.E.; Saroyan, R.A.; Weber, M.J. "Nd-doped laser glass spectroscopic and physical properties", Lawrence Livermore National Laboratory Rev. 2, Report M-095 (1981)

[Stone 1996] Stone, B.T; Bray, K.L. "Fluorescence properties of Er3-doped sol-gel glasses", J. Non-Cryst. Solids, 197 (1996), pp. 136-144

[Strohhofer  1998] Strohhofer, C.; Fick, J.; Vasconcelos, H.C.; Almeida, R.M. "Active optical properties of erbium nanocrystals in sol-gel derived glass films", J. Non-Cryst. Solids, 226 (1998), pp. 182-191

[Sun  2005A] Sun, L.- N.; Zhang, H.- J.; Meng, Q.- G.; Liu, F.- Y.; Fu, L.-S.; Peng, C.- Y.; Yu, J.- B.; Zheng, G.- L.; Wang, S.- B. "Near-infrared luminescent hybrid materials doped with lanthanide (Ln) complexes (Ln = Nd, Yb) and their possible laser application", J. Phys. Chem. B, 109 (2005), pp. 6174-6182

[Sun 2005B] Sun, L.N.; Zhang, H.J.; Fu, L.S.; Liu, F.Y.; Meng, Q.G.; Peng, C.Y.; Yu, J.B. "A new sol-gel material doped with an erbium complex and its potential optical-amplification application", Adv. Funct. Mater., (15) 2005,  pp. 1041-1048

[Syms 1998] Syms, R.R.A.; Holmes, A.S.; Huang, W.; Schneider, V.M.; Green M. "Development of the SC-RTA process for fabrication of sol-gel based silica-on-silicon integrated optic components", J. Sol-Gel Sci. and Technol., 13 (1998), pp. 509-516

[Villanueva-Ibanez 2003] Villanueva-Ibanez, M.; Le Luyer, C.; Marty, O.; Mugnier, J. "Annealing and doping effects on the structure of europium-doped HfO2 sol -gel material", Opt.Mater., 24 (2003), pp. 51-57

[Wang 1993] Wang, J.; Brocklesby, W.S.; Lincoln, J.R.; Townsend, J.E.; Payne, D.N. "Local structures of rare-earth ions in glasses: the "crystal-chemistry" approach", J. Non-Cryst. Solids, 163 (1993), pp. 261-267

[Ward 2007] Ward, M.D. "Transition-metal sensitised near-infrared luminescence from lanthanides in d-f heteronuclear arrays", Coord.Chem.Rev., 251 (2007), pp. 1663-1677

[Weissman 1942] Weissman, S.I. "Sensitized emission", J.Chem.Phys., 10 (1942), pp. 214-217

[Werts 2004] Werts, M.H.V.; Jukes, R.T.F.; Verhoeven, J.W. "The emission spectrum and the radiative lifetime of $Eu^{3+}$ in luminescent lanthanide complexes", Phys.Chem., 4 (2004), pp. 1542-1548

[Whan 1962] Whan R.E.; Crosby G.A. " Luminescence studies of rare earth complexes: benzoylacetonate and dibenzoylmethanate chelates", J.Mol.Spectrosc., 8 (1962), pp. 315-320

[Xiang 2000] Xiang, Q.; Zhou, Y.; Ooi, B.S.; Chan, Y.C.; Kam, C.H. "Optical Properties of $Er^{3+}$-doped $SiO_2$-$GeO_2$-$Al_2O_3$ Planar Waveguide Fabricated by Sol-Gel Processes", Thin Solid Films, 370 (2000), pp. 243-247

[Xu 1995] Xu, W.; Dai, S.; Toth, L.M.; Delcul, G.D.; Peterson, J.R. "Green upconversion emission from Er3-gel silica glasses under red-light (647.1 nm) excitation (ion doped into sol)", Journal of physical chemistry, 99 (1995), pp. 4447-4450

[Yan 1997] Yan, B.; Zhang, H.J.; Wang, S.B.; Ni, J.Z. "Lumineseenee properties of the ternary rare earth complexes with β-diketones and 1,10-phenanthroline incorporated in silica matrix by a sol-gel method", Mater. Chem. Phys., 51 (1997), pp. 92-96

[Yang 2004] Yang, C.; Fu, L.M.; Wang, Y.; Zhang, J.P.; Wong, W.T.; Ai, X.C.; Qiao, Y.F.; Zou, B.S.; Gui, L.L. "A highly luminescent europium complex showing visible-light-sensitized red emission: direct observation of the singlet pathway", Angew.Chem., Int.Ed., 43 (2004), pp. 5010-5013

[Yeatman 1999] Yeatman, E.M.; Ahmad, M.M.; McCarthy, O.; Vannucci, A.; Gastaldo, P.; Barbier, D.; Mongardien, D.; Moronvalle, C. "Optical gain in $Er^{3+}$-doped $SiO_2$-$TiO_2$ waveguides fabricated by the sol-gel technique", Opt. Comm., 164 (1999), pp. 19-25

[Zevin 1997] Zevin, M.; Reisfeld, R. "Preparation and properties of active waveguides based on zirconia glasses", Chem. Mater., 8(1997), pp. 37-41

[Zhou 1997] Zhou, Y.; Lam, Y.L.; Wang, S.S.; Liu, H.L.; Kam, C.H.; Chan, Y.C. "Fluorescence enchanesement of $Er^{3+}$-doped sol-gel glass by aluminium codoping", Appl. Phys. Lett., 71 (1997), pp. 587-589

# Chapter 2

## 2. Sol-gel synthesis

Among the different wet chemical synthesis techniques, the most suitable method for bulk metal oxides and nanoparticles fabrication is a sol-gel approach. The number of oxide nanopratilces obtained by sol-gel route is smaller compared to the wide range of materials prepared via powder techniques.

Moreover, sol-gel method is a convenient way to coat large-scale and complex geometries substrates using quite simple deposition techniques to obtain homogeneous coatings. Sol-gel technique can be easily applied for multilayered films fabrication. Different types of sol-gel layers for various applications can be produced, such as adhesive coatings, conductive coatings, biocompatible coating. The sol-gel techniques are low-temperature approach for synthesis of different class of materials inorganic, organic or hybrid materials. Two chemical reactions are on the base of sol-gel approach - hydrolysis and condensation of molecular inorganic (metallo-organic) precursors in alcoholic solutions. Besides simplicity of sol-gel synthesis, it allows many benefits for films fabrication, such as precise stoichiometry control of precursor solutions, tailored microstructure, ease composition control, possibility to incorporate various functional groups and elements, low annealing temperatures, ease incorporation of different functional groups and elements, simple equipment. This makes sol-gel method such popular in nanomaterials preparation by spinning, dip-coating or impregnation techniques [Brinker 1990, Hench 1990, Livage 1988].

However sol-gel approach has some limitations for application in industry because of weak bonding, low wear-resistance, and difficulties with porosity control. The thickness of sol-gel coating is also terminated to achieve coatings without cracks. The presence of organic compounds in thick layers often leads to failure during thermal treatment process. Sol-gel approach is strongly dependent on the substrate, and the thermal expansion coefficient must be accurately considered.

Different structures can be obtained, using different type of the catalyst in sol-gel synthesis.
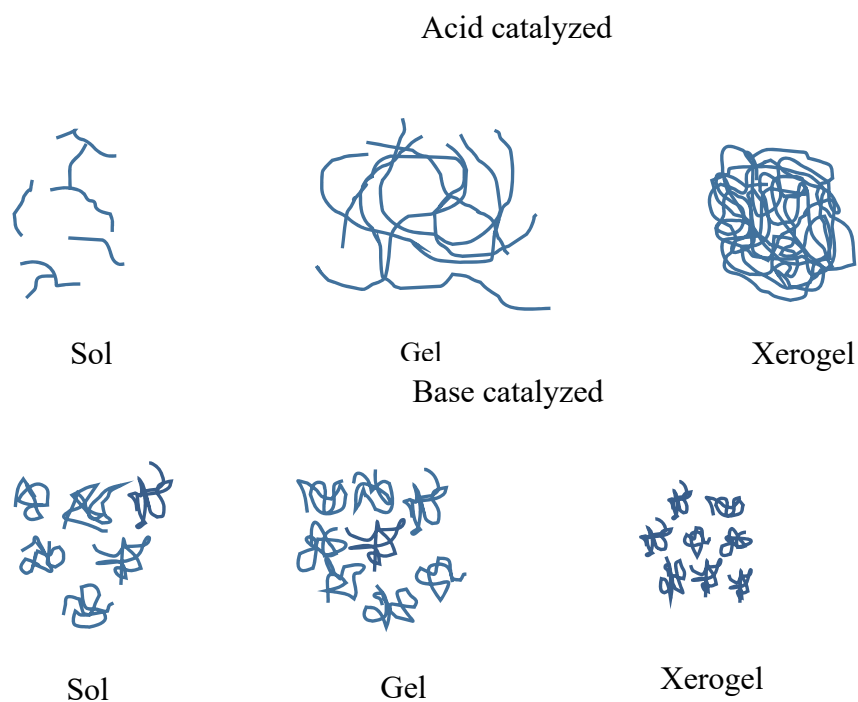
Acid catalyzed



Sol                    Gel                    Xerogel

Base catalyzed



Sol                    Gel                    Xerogel

**Figure 2.1.** Sol-gel synthesis in acidic and basic conditions.

In acidic sol-gel synthesis conditions, the silica forms linear cross linked molecules, Figure 2.1. Gelation occurs when these molecular chains form branches and enlace.

Sol-gel synthesis in basic conditions is described by more highly branched clusters, and when the clusters are linked gelation take place (Fig.2.1). In course of time colloidal particles link and 3-dimensional network is formed. After the sol-gel transition, the solvent phase is removed from the interconnected pore.

One of the sol-gel modifications of sol-gel chemistry can be marked as aqueous and non-aqueous synthesis. Aqueous sol-gel chemistry is complex process because of the high reactivity of the metal oxide precursors towards water, and due to the important control of hydrolysis and condensation rate of the precursors, temperature, oxidation rate, pH, the nature and concentration of anions, mixing method and etc. It is important to note that the products of the reactions in aqueous sol-gel chemistry are

mostly amorphous. As a mandatory step after sol-gel synthesis is annealing [Livage 1988].

As an alternative to aqueous sol-gel processes is nonaqueous sol-gel synthesis in organic solvents without presence of water. The role of organic components is multifunctional, because they are not only solvents but also organic ligands of the precursor molecule. Organic species participate in Oxygen formation and affects on the shape and size of the particle, as well as the surface properties. During non-aqueous synthesis all these parameters give a possibility to obtain the metal oxide nanoparticles with uniform morphologies and the crystallites sizes of a few nanometers easily soluble in organic solvents. In conjunction with inorganic particle formation, the initial organic components during the reactions following elementary mechanisms of organic chemistry [Jun 2006, Niederberger 2007A, Niederberger 2007B, Park 2007, Pinna 2008].

## 2.1 Aqueous sol-gel chemistry

The aqueous sol-gel process is the conversation of precursors into an organic solid via inorganic polymerization reactions induced by water. The precursor is an inorganic (Carbon free) metal salt (sulfates, nitrates and etc.) or metal organic compounds such as an alkoxides. Occurrence of hydrolysis reactions which convert the ions to new ionic species or to precipitates [Livage 1988, Hubert-Pfalzgraf 1998].
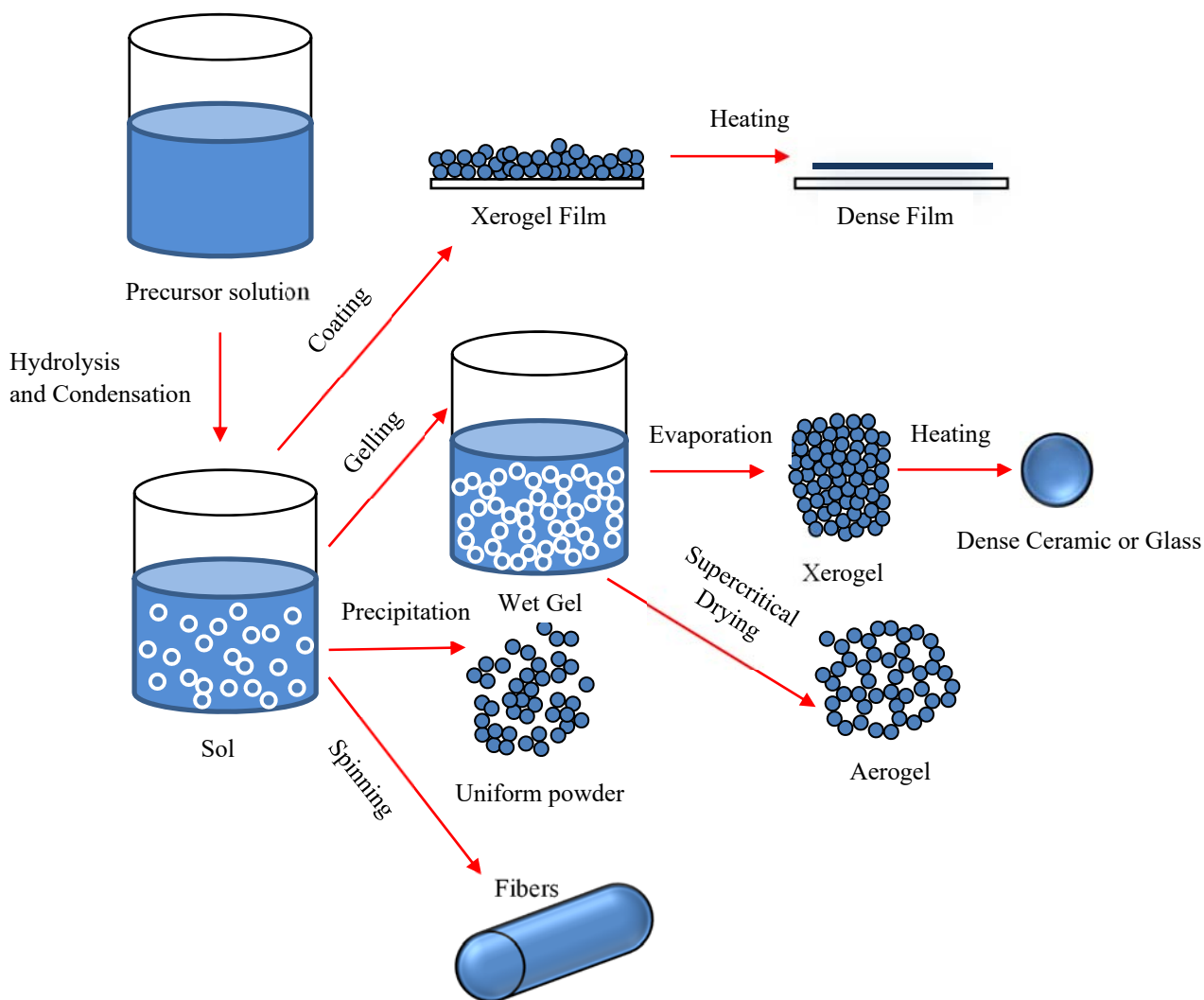
**Figure 2.1.1.** Sol-gel synthesis.

The hydrolysis of salts can involve the cation, the anion or even both. The most widely used starting compounds are the metal alkoxides that can react easily with water and exist in many metals modifications.

Commonly used in industry low cost alkoxides are Si, Ti, Al, Zr-based, whereas other ones are hardly available and have a high cost, such as Mn, Fe, Co, Ni, Cu, Y, Nb, Ta. The sol-gel process includes the steps showed on Fig. 2.1.1. Dissolution of metal organic precursors in an organic solvent that is miscible with water and homogeneous solution preparation, or dissolution of inorganic salts in water [Bradley 2001, Turova 2002].

i)     Homogeneous solution transformation into a sol by treatment with a suitable reagent (commonly water with or without any acid/base)
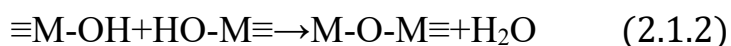
ii)     Sol aging

iii)    Shaping

iv)     Sintering

During the first step is the formation of an inorganic polymer by hydrolysis and condensation reactions occurs, the transformation of the molecular precursor into a highly crosslinked solid takes place at this moment. Sol is forming by hydrolysis and condensation results in a gel. Drying of gels is possible by removal of the pore liquid in harsh conditions without collapse of the network and aerogels are formed. In case of the gel drying under ambient conditions, shrinkage of the pores occurs and xerogel is obtained. The sol-gel processes allows to configurate the material into any form such as monoliths, powders, films, fibers, as well as convert it into a ceramic material under heat treatment [Mehrotra 1997].

The inorganic route of sol-gel when the precursor is an aqueous solution of an inorganic salt involves the formation of condensed species by adjusting the pH, changing the oxidation state and increasing the temperature. The disadvantages of this method are that the process is complex and result in the formation of a large number of oligomeric species. The counter anions are able to coordinate the metal ion and can influence the morphology, the structure of the resulting solid phase. The removal of these anions from the final metal oxide is a problem. Use of metal alkoxides as precursors allows avoiding many of these undesirable effects [Livage 1988, Hench 1990, Jolivet 2000, Brinker 1990]. They are soluble in organic solvents, forming homogeneous solution. The metal alkoxides transformation involves two main reactions: hydrolysis and condensation Fig. 2.1.1.

When hydrolysis occurs, the alkoxide groups (-OR) are replaced via the nucleophilic attack of the Oxygen atom of a water under release of alcohol forming a metal hydroxide.

Then the condensation between two hydroxylated metal species result in M-O-M bonds under release of water (oxolation), and the reaction between an alkoxide and hydroxide leads to M-O-M bonds under release of an alcohol (alkoxolation).

$$\equiv\text{M-OR} + H_2O \rightarrow \equiv\text{M-OH} + ROH \qquad (2.1.1)$$

$$\equiv\text{M-OH} + HO\text{-M}\equiv \rightarrow \text{M-O-M}\equiv + H_2O \qquad (2.1.2)$$

$$\equiv\text{M-OR} + HO\text{-M}\equiv \rightarrow \equiv\text{M-O-M}\equiv + ROH \qquad (2.1.3)$$

**Scheme 2.1.4.** Sol-gel process using metal alkoxides. Hydrolysis (Eq. 2.1.1) and condensation, oxolation (Eq. 2.1.2) and alkoxolation (Eq. 2.1.3).

In principal the chemical reactivity of metal alkoxides during hydrolysis and condensation depends on the electronegativity of the metal atom, its ability to increase the coordination number, the steric hindrance of the alkoxy group, and on the molecular structure of the metal alkoxides (monomeric or oligomeric). During the hydrolysis step the amount of water and the way of water adding influence alkoxides degree of hydrolysis and which oligomeric intermediate species are formed. Depending on the synthesis procedure, e.g. pH or the molar ratio r of $H_2O$:M in Eq. 2.1.1, the structures of the inorganic polymers may be modified. Other parameters are the polarity, the solvent acidity, and the dipole moment.

The control of the hydrolysis and condensation rates is quite complicated in sol-gel methods. Most of transition metal oxide precursors reacts too fast what leads to loss of morphological and structural control over the final oxide material. The different metal alkoxides reactivity makes the control of the composition and the homogeneity of complex multimetal oxides. The reactivity of the precursors can be modified by addition of chelating ligands such as carboxylic acids, functional alcohols or β-diketones. The slow release of water allows control of the water concentration thus modifying the precursors reactivity [Livage 1988, Hubert-Pfalzgraf 1998].

The high sensitivity of aqueous sol-gel approach towards any slight changes in the synthesis conditions as well as the simultaneous occurrence of hydrolysis and condensation reactions makes difficulty to control the sol-gel process of metal oxides in aqueous medium.

## 2.2 Non-aqueous sol-gel chemistry

The first studies on nonaqueous sol-gel processes started in the middle of the 19th century, when the reaction between metal chlorides and alcohols were investigated. Non-aqueous sol-gel approach is less popular and implicates the transformation of the precursor in an organic solvent under exclusion of water. The number of precursors is more various than for aqueous sol-gel chemistry, and includes inorganic metal salts and alkoxides, metal acetates and acetylacetonates. The use of organometallic compounds is rather based on thermal decomposition than sol-gel. The first studies on nonaqueous sol-gel processes started in the middle of the 19th century, when the reaction between metal chlorides and alcohols were investigated. Dearing and Reid proposed aqueous and nonaqueous routes to silica gels, assuming that they might show "different absorptive power" [Dearing 1928].

In the middle of the 1980s, and at the beginning of the 1990s, research on non-hydrolytic preparation routes to metal oxides became mostly popular. Two approaches are known as the main research directions: the first is focused on the preparation of metal oxide gels; the second is connected with preparation of metal oxide powders. Some groups developed glycothermal method involving the reaction of metal alkoxides or acetylacetonates with 1,4-butanediol as a versatile approach to various metal oxides [Inoue 2004, Kominami 1993]. Corriu and coworkers published their work on monolithic Si, Al, and Ti gels, as well as on gels containing two metals. Also the synthesis of Zinc oxide gels was showed, using Zinc alkoxides as precursors and acetone as condensation agent [Corriu 1992A, Corriu 1992B, Corriu 1992C, Goel 1992]. The gels containg zirconate nanocrystals were formed upon aging. Similar approach was used for BaO, BaTiO$_3$, TiO$_2$. A huge variety of metal oxide gels were later on synthesized and reported: Silica, Alumina, mixed Al/Si, Titania, and transition metal oxides from the corresponding metal chlorides and metal alkoxides or ethers as Oxygen donors [Borm 2006].
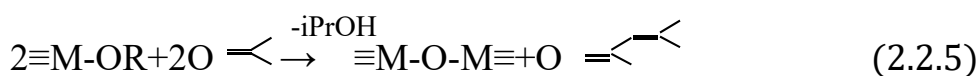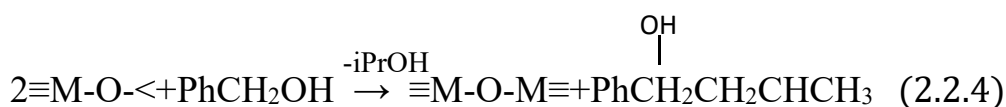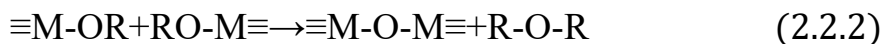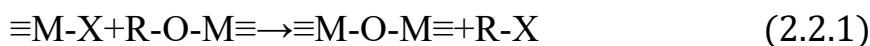
At this date, the number of metal oxide nanoparticles that are prepared by nonaqueous processes has grown and ranges from simple binary metal oxides to more

complex ternary, multi-metal and doped systems [Ivanda 1999, Kominami 1999, Zappel 1955].

An interesting question arises how the oxidic network is forming if the water is not present in the non-aqueous system. The Oxygen for nanoparticles is provided by the solvent (alcohols, ketons or aldehydes, ethers) or by the organic constituent of the precursor (alkoxides, acetylacetonates). The formation of the metal-oxygen-metal bonds as basic structural unit can be demonstrated in the following pathways scheme:

i)      Elimination of the alkyl halide, Eq.2.2.1

ii)      Elimination of the Ether, Eq.2.2.2

iii)      Condensation of carboxylate groups (ester and amide eliminations), Eq.2.2.3

iv)      Carbon-carbon coupling of benzylic alcohols and alkoxide molecules, Eq.2.2.4

v)      Aldol/ketamine condensation, Eq.2.2.5

Elimination of the alkyl halide during the condensation between metal alkoxides and metal halides under release of an alkyl halide is presented in Eq.2.2.1. The reaction between two metal alkoxides results in ether elimination, Eq.2.2.2. Condensation of carboxylate groups leads to the ester and amide elimination processes, Eq.2.2.3.

$$\equiv M\text{-}X + R\text{-}O\text{-}M \equiv\ \rightarrow\ \equiv M\text{-}O\text{-}M \equiv + R\text{-}X \qquad (2.2.1)$$

$$\equiv M\text{-}OR + RO\text{-}M \equiv\ \rightarrow\ \equiv M\text{-}O\text{-}M \equiv + R\text{-}O\text{-}R \qquad (2.2.2)$$

$$\underset{\equiv M\text{-}O\text{-}CR}{\overset{O}{\|}} + R\text{-}O\text{-}M \equiv\ \rightarrow\ \equiv M\text{-}O\text{-}M \equiv + \underset{RO\text{-}CR}{\overset{O}{\|}} \qquad (2.2.3)$$

$$2\equiv M\text{-}O\text{-}< + PhCH_2OH\ \overset{\text{-iPrOH}}{\rightarrow}\ \equiv M\text{-}O\text{-}M \equiv + PhCH_2CH_2\underset{\overset{|}{OH}}{C}HCH_3 \qquad (2.2.4)$$

$$2\equiv M\text{-}OR + 2O =<\ \overset{\text{-iPrOH}}{\rightarrow}\ \equiv M\text{-}O\text{-}M \equiv + O =<^{-<} \qquad (2.2.5)$$

Carbon-carbon bond formation between alkoxy groups is also observable, Eq.2.2.4. Transition metals with high Lewis acidity (Nb,Y, Ce) are able to directly catalyse Guerbet-like reaction. In case of ketones as solvents, the release of oxygen involves adol condensation, where two carbonyl compounds react with each other under water elimination, Eq.2.2.5. The water provides oxygen for the metal oxide formation [Borm 2006].

## 2.3 Sol-gel films deposition techniques

Sol-gel layers can be deposited on the substrate using spin or dip coating process. Films deposited by these two techniques are divers. Spin-coated film is deposited and dried in a few seconds, when dip-coated films are formed with a speed a few centimeters per minute. Both techniques are used to produce various coatings and thin films with wide range thickness, different morphology, and controllable microstructure, Table 2.3.1. For both of methods the thickness of the film and its density are inverse related, and the thin films are denser than thick.

**Table 2.3.1.** An overview of the common thin film deposition techniques.

| Spin-coating technique | Dip-coating technique |
|---|---|
| **Thickness** | |
| 10 nm -5 µm | 20 nm-50 µm |
| **Benefits** | |
| Uniformity, reproducibility, excellent thickness control, low-cost | Complex and irregular shapes, continuous regime of the process, simple |
| **Limitations** | |
| The substrate has to be flat, high material loss | Surface defects: pin holes and voids |
| **Applications** | |
| Flat panel displays, photo resists, dielectric layers | Electronic parts and assemblies, insulating polymer layers |

Spin-coating deposition allows achieving uniform coatings, and on the other hand this technique is not convenient for thick films deposition, especially of large areas of unsymmetrical substrates, and the substrate have to be flat and smooth. Other advantages of spin-coating are good reproducibility, excellent thickness homogeneity, ease of integration, speed, the possibility of coating one face only, low pollution and low cost. Moreover the shape of the substrate for spin-coating has to allow fast rotation. Various types of thickness uniformity and defects can arise in spin-coated layers. This takes place because the optimal parameters from one system to the other differ greatly. By all means the surface has to be clean, the quantity of dispensed solution is adapted to the surface dimensions, the speed and rotation time should be tailored to the solution viscosity and volatility, as well as the proper atmosphere control should be managed. The thickness inhomogeneity in the form of radial

streaks can appear even if the quantity of solution is enough to prepare the layer and the substrate is clean from any particles. This can be explained by appearance of Marangoni effect, what can be reduced by reduction of the evaporation rate [Levy 2015, Wright 2000]. Film thickness could be easily changed by changing spin rate.

The coatings obtained by dip-coating technique characterized by a better adjustment of the polymer molecules, leading in a denser and less rough film than in spin-coated samples. At another point appearance of non-uniformity of the coating near the edges of the substrate is a frequent problem in dip-coating process. For instance, to fabricate 0.5 µm layer onto the disk around 20 cm$^2$ using solution of 10 vol. % nonvolatile component, 0.1 ml of solution is dispensed. Only 10 % of the solution is coated, while 90 % is splashed up. Fast evaporation of 0.1 ml of solution was observed, what is leading to increase in solvent vapor pressure. The control of the atmosphere which is important for sol-gel film structuration is realized by eliminating solvent vapor pressure forcing airflow inside the drying chamber. The turbulence above the substrate is leading to local thickness fluctuations.

Various types of thickness uniformity and defects can arise in spin-coated layers. This takes place because the optimal parameters from one system to the other differ greatly. By all means the surface has to be clean, the quantity of dispensed solution is adapted to the surface dimensions, the speed and rotation time should be tailored to the solution viscosity and volatility, as well as the proper atmosphere control should be managed. The thickness inhomogeneity in the form of radial streaks can appear even if the quantity of solution is enough to prepare the layer and the substrate is clean from any particles. This can be explained by appearance of Marangoni effect, what can be reduced by reduction of the evaporation rate [Levy 2015, Wright 2000].

## 2.4 Film formation by spin-coating technique

Spin-coating technique is based on the liquid deposition onto a moving substrate. The substrate is accelerated to high angular velocities, during which the excess

liquid is spun off from the substrate, forming thin layer of coating. Thickness of less than 30 nm to a few microns per layer can be easily obtained [Mitzi 2009].
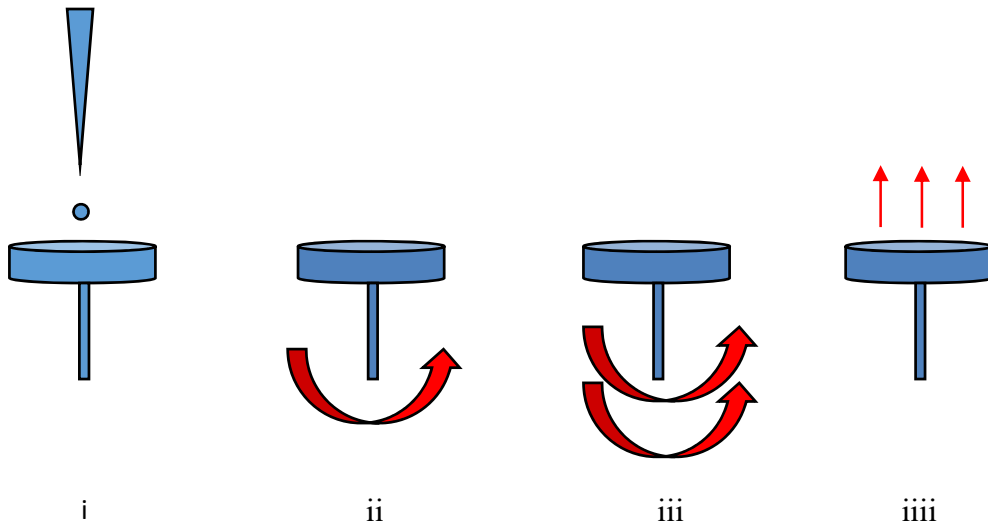


i        ii        iii        iiii

**Figure 2.4.1.** Spin-coating technique [arranged by Mitzi 2009].

When the homogeneous layer is formed, the spinning rate may be increased to thin the film and to drive air convection above the wet film. Under such condition, Esmilie et al. proposed a simple model of the spin-coating process predicting film thickness as a function of a number of physical parameters from the following equation (Eq. 7):

$$h(t) = \frac{h_0}{\sqrt{1+\frac{4\rho w^2 h_0^2 t}{3\eta}}} \qquad (7)$$

where $h(t)$ is the film thickness at the time t, $h_0$ is the film thickness at t=0 (initial thickness), $\rho$ is the density of the liquid, $\omega$ is the angular velocity, $\eta$ is the viscosity.

Fundamentally this technique implicates the equilibrium between the centrifugal and viscous forces. The control of the coating thickness can be carried out by controlling the spin speed and time, and the solution viscosity [Mitzi 2009].

In the work of Meyerhofer was discussed the effect of solvent evaporation out of the top surface of the solution. The Meyerhofer observation is enlightening because the spin-coating run was split into two steps: first controlled by viscous flow and the second controlled by evaporation. Using this consideration he was able to

predict the final film thickness $h(t)$ inversely proportional to the square root of the spin speed, (Eq. 8):

$$t \infty \frac{1}{\sqrt{\omega}} \qquad (8)$$

When the rotation dependencies for the viscous flow and the evaporation rate are known, the final film thickness should vary with the spin rate according to the -1/2 power [Birnie 2004].

The viscosity and density can vary during the solvent evaporation with the time. The sols with high concentrations of particles and polymers result in irregular thickness of the coating thickness. Also on the coating surface appears some roughness in the form of periodic ridges. These defects were described in the work of Kozuka and Birnie and attributed to the solvent evaporation. Solvent evaporation initiates surface tension gradients and occurrence of cappilar convection (Gibbs-Maragoni effect). If the surface tension gradient occurrence is driven by temperature gradient it calls Bénard-Marangoni convection. Nevertheless, both of the effects cause surface defects. These undesirable effects are possible to reduce in the process of evaporation if select carefully solvents [Mitzi 2009, Zhang 2009].

## 2.5 Film formation by dip-coating technique

Dip-coating as an another low-cost deposition technique especially wide used in the semiconductor industry for coating irregular and intricate shapes, where polymeric or particulate inorganic precursors are accumulated on the substrate surface through the gravitational draining and ongoing condensation reactions. Substrate is immersed into the film-forming solution and the layer is obtained by vertical substrate extraction from the solution storage tank at a constant rate. Deposited films structure depends mainly on size and structure of the precursors, relative rates of condensation and evaporation, pressure in the capillary, withdrawal speed of substrate. In case of use polymeric silicate precursors, the porosity and refractive index of the film can be modified in the following intervals, volume porosity (0-56 %), pore radius (0-3.1 nm), surface area (1.2-263 $m^2g^{-1}$), RI (1.18-1.45) [Brinker 1994].

The physics of dip-coating film formation includes a balance among gravitational forces, the viscous drag and surface tension in the meniscus.
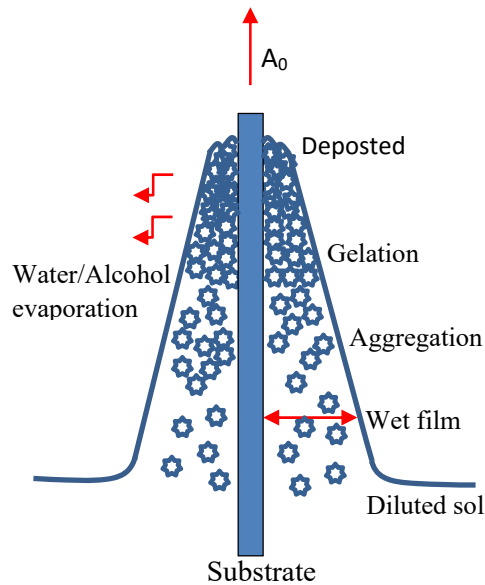


**Figure 2.5.1.** Dip-coating process.

During the course of dip-coating process the substrate is draw vertically upon from the cuvette with sol at a speed $A_0$, Figure 2.5.1. The running substrate pick the sol up in a fluid mechanical boundary layer that splits in two above the liquid cuvette surface the outer layer returning to the cuvette.
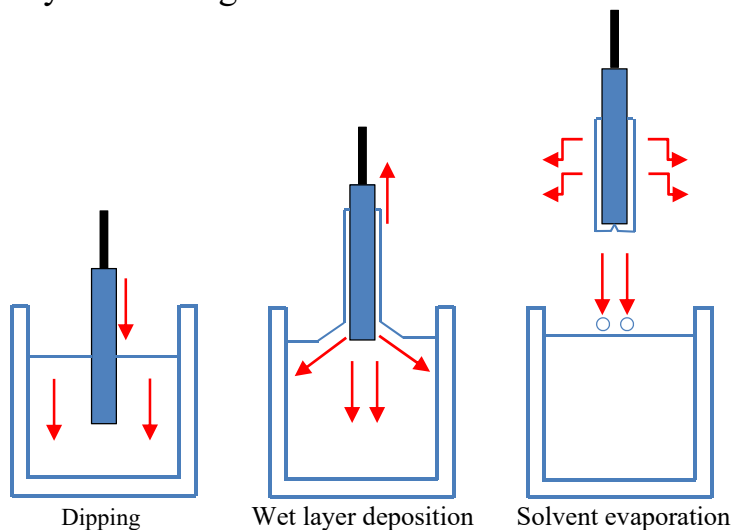


**Figure 2.5.2.** Dip-coating process mechanism.

The fluid film ceases at h=0 drying line (x=0) (Eq.9) whereas the solvent is evaporating and draining. When the drying line velocity is equal to $A_0$, the process is stabilized compared to the liquid cuvette surface.

A fluctuating rate of the evaporation is close to the drying line and results in a parabolic thickness profile. It has been determined that the film thickness *t* is inversely proportional to the square root of the spin speed [Brinker 1991]:

$$h(x) \propto x^{1/2} \qquad (9)$$

where $h(x)$ is the film thickness as a function of x position below the drying line. A coherent liquid film entrains on withdrawal of the substrate from the coating solution then consolidates by drying and ongoing chemical reactions. The final coating is obtained after curing/sintering step. During the consolidation step the sol-gel transition with concurrent draining, evaporation and hydrolysis occur. It is obvious when during the deposition process in a receding drying line that is moving downwards with colorful interface lines, leaving behind the consolidated film. On account of evaporation and cooling furthermore a downward vapor flow forms out over the surface of the wet film, improving the drying. Any turbulence or variation in this stage of the deposition will result in inhomogeneities in the film.

Looking at the film formation as physical process it based on a fluid mechanical equilibrium between the entrained film and the receding coating fluid. Several forces under control equilibrium, in particular the viscous drag and the gravity force the same as the surface tension and inertial force [Aegerter 2004].

In the work of Scriven was indicated that the thickness of the deposited films is related to the position of the streamline dividing upward and downward moving layers. At high sol viscosity and substrate speed $A_0$ the deposited film thickness $h$. When the liquid viscosity and substrate speed Uo are high enough to lower the curvature of the meniscus, the deposited film thickness $h$ is that which balances the viscous drag (proportional to q Uo/h) and gravity force (pgh):

$$h = \frac{c \cdot (\eta U)^{2/3}}{\gamma^{1/6} (\rho g)^{1/2}} \qquad (10)$$

where *c* is a constant (0.94 for Newtonian liquids), η is the liquid viscosity, U the substrate withdrawal rate, ρ the density of the liquid, γ the liquid vapor surface tension, g is the gravitational acceleration. The rate of withdrawal U is selected depending on the chemical properties of the film-forming solution. Moreover the film thickness increases with the withdrawal speed.

This equation assumes steady-state balancing between drainage of the liquid because of gravitational forces and a viscous drag effect from moving substrate. This equation does not consider liquid evaporation. Liquid evaporation occurs in such manner that the thickness profile of the drying liquid come close to parabolic shape. Thickness and the evaporation speeds are changing faster near the drying line. When a mixture of different solvents is used with different evaporation rates, and the more volatile solvent is completely evaporated, a second drying line involving the evaporation of the higher boiling point solvent is noticed at a higher position from the meniscus. However different sol compositions leads to changes in surface tension in the liquid film which is changing by position. Surface tension differences result in liquid transport within the film. Solvent evaporation bring a change in sol stability. Solvent composition modification subverts sol stability and cause gel formation or precipitates [Zhang 2010, Scriven 1988].

Surface inhomogeneties can be observed in dip-coated films. The most common of them are pin holes, voids, thickness variations and wavy appearance. Pin holes and voids are caused by air entrapment in the film, dust particles and surface contamination. Dip coating is the most suitable technique to produce homogeneous sol-gel films. This technique is characterized as the best in control of the processing conditions. Dip-coating setup allows film fabrication with one-directional thickness gradients by programming withdrawal rate in the direction of dipping. This characteristic is very useful for sampling the thickness influence on a single substrate sample, or for fabrication of multiwavelength interferometry monochromators [Levy 2015].

## 2.6 SiO₂-HfO₂, HfO₂-P₂O₅, SiO₂-P₂O₅ systems

It should be noted that the behavior indicated in the phase diagram is related to the bulk materials and in case of thin films or coatings their characteristics during fabrication process could be different.

Moreover, despite many applications of $SiO_2$-$HfO_2$-based system of this increasingly important system as dielectric material in semiconductor devices, the literature shows very little structural characterization of this system [Kerber 2004, Zhao 2005].
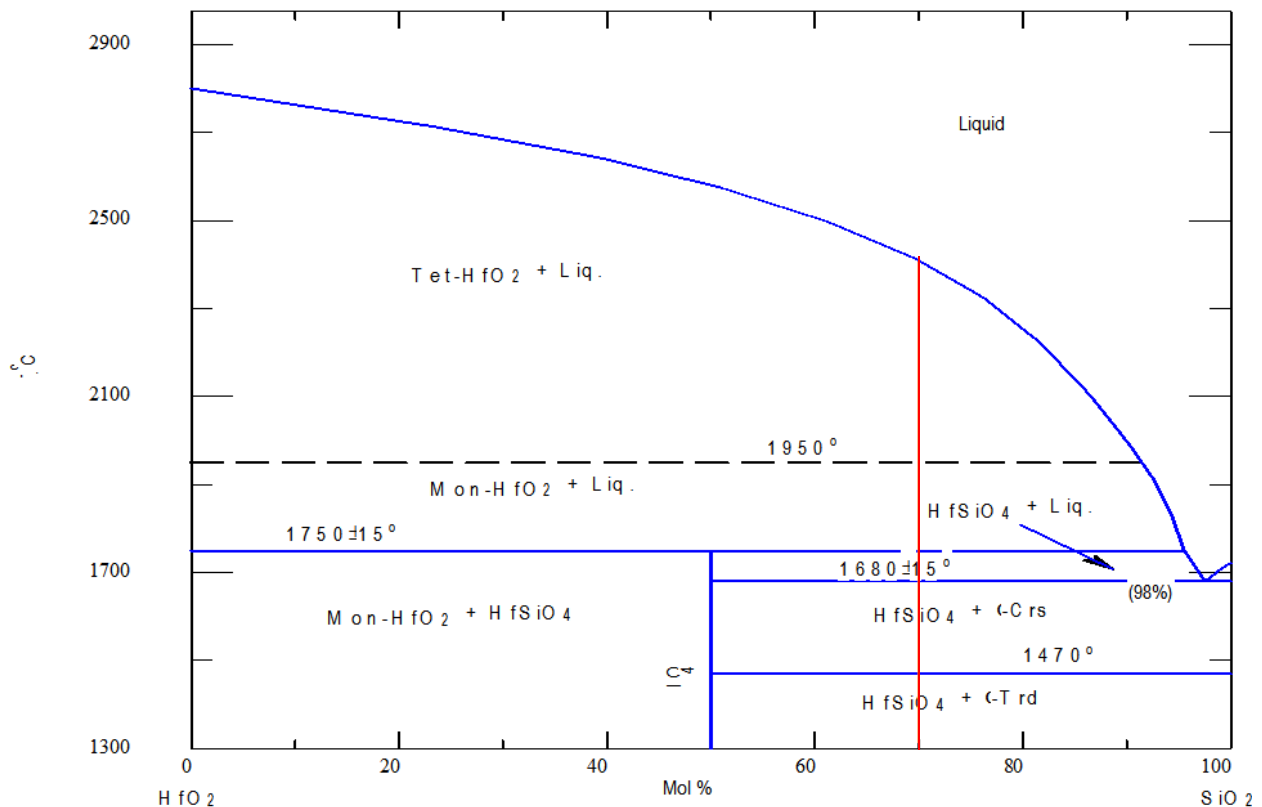


**Figure 2.6.1.** SiO₂-HfO₂ phase diagram.

In monolith samples 70SiO₂-30HfO₂ prepared by conventional melting quenching technique at 1680 °C amount of liquid melt is about 44 %. Complete melting occurs at 2400 °C. Use of sol-gel technology allows fabricating vitreous films at the temperature 900 °C.

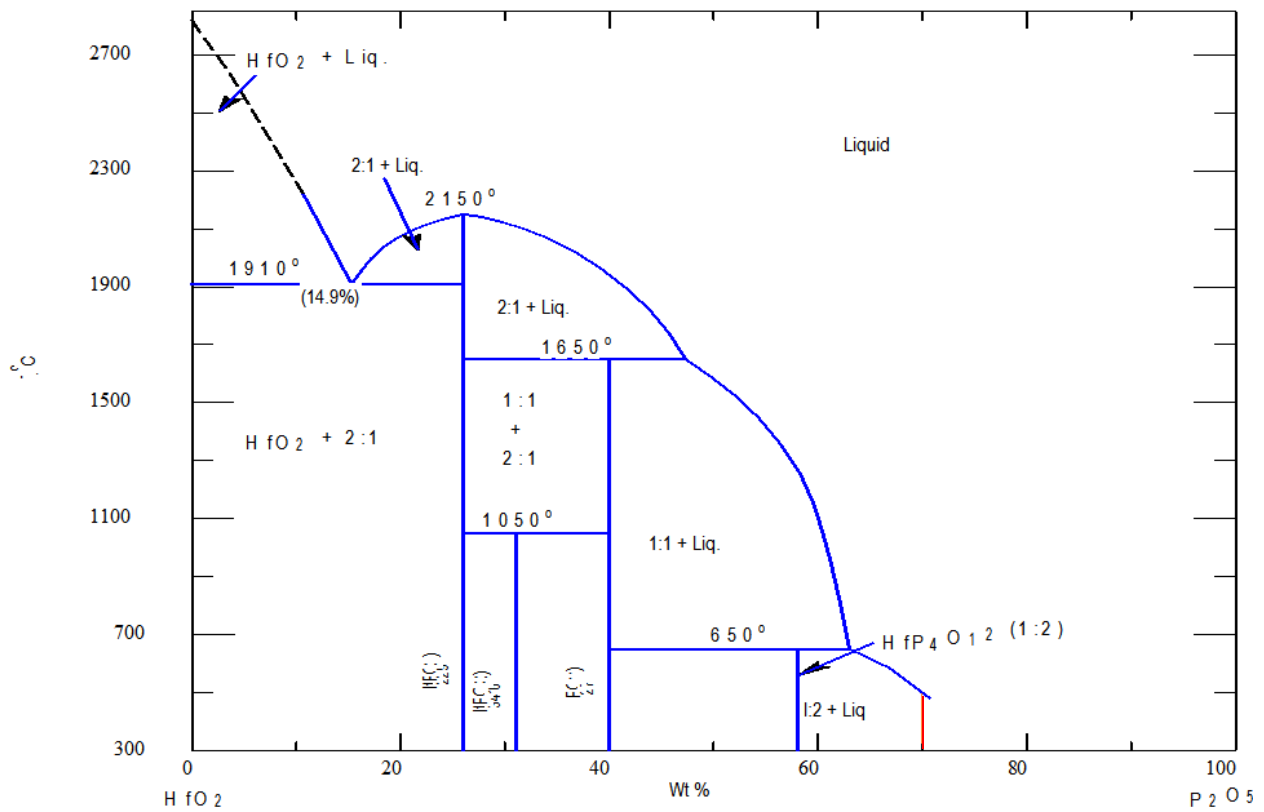**Figure 2.6.2.** HfO$_2$-P$_2$O$_5$ phase diagram.

The presence of Phosphorous significantly decreases meting temperature of the system. At the concentration of Phosphorous 70 mol. %, the temperature for annealing process decreases up to 600 °C.
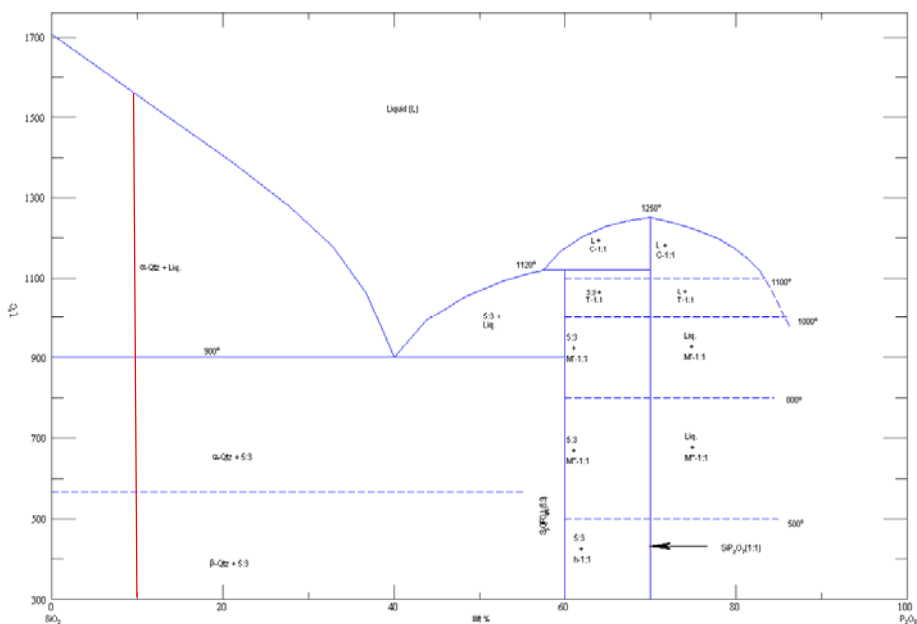
**Figure 2.6.3.** SiO$_2$-P$_2$O$_5$ phase diagram.

For the concentration of Phosphorous 10 mol. % (1:9) the melting temperature is dropping to 1520 °C and complete melting occurs for the monolith samples without Hafnium.

In the monolith at 900 °C (eutectic point) with 27 % of liquid melt. Sol-gel approach ensures preparation 100 % liquid melt and vitreous coatings at 900 °C.

The high concentration of large Phosphorous ions inside the matrix disrupts silica-oxygen network. With increasing the Phosphorous concentration (2:6) homogeneity of silica-oxygen network with formation of the chemical species and crystallization occurs.

# Bibliography

[Adachi 1988] Adachi, T.; Sakka, S. "The role of N,N- dimethylformamide, a DCCA in the formation of silica-gel monoliths by sol-gel method", J. Non-Cryst. Solids 99

[Aegerter 2004] Aegerter, M.A.; Menning, M. "Sol-Gel Technologies for Glass Producers and Users", Springer US, (2004), pp. 493

[Birnie 2004] Birnie, D.P. "Sol-Gel Technologies for Glass Producers and Users", Springer US, (2004), pp. 49-55

[Borm 2006] Borm, P.J.A., Robbins, D., Haubold, S., Kuhlbusch, T., Fissan, H., Donaldson, K., Schins, R., Stone, V., Kreyling, W., Lademann, J., Krutmann, J., Warheit, D., Oberdorster, E. "The potential risk of nanomaterials: A review carried out for ECETOC", Part. Fibre Toxicol., 3 (2006), pp. 11-45

[Bradley 2001] Bradley, D.C., Mehrotra, R.C., Rothwell, I.P., Singh, A. "Alkoxo and aryloxo derivatives of metals", Academic Press: London, (2001), pp.704

[Brinker 1990] Brinker, C.J., Scherer, G.W. "Sol-gel science", Academic Press, (1990), pp. 980

[Brinker 1991] Brinker, C.J.; Frye, G.C.; Hurd, A.J.; Ashley, C.S. "Fundamentals of sol-gel dip coating", Thin Solid Films, 201 (1991), pp. 97-108

[Brinker 1994] Brinker, C.J.; Hurd, A. "Fundamentals of sol-gel dip-coating", Journal de Physique III, EDP Sciences, 4 (1994), pp.1231-1242

[Corriu 1992A] Corriu, R., Leclercq, D., Lefevre, P.,Mutin, P.H., Vioux, A. "Preparation of monolithic binary oxide gels by a nonhydrolytic sol-gel process", Chem. Mater., 4 (1992), pp. 961-963

[Corriu 1992B] Corriu, R.J.P., Leclercq, D., Lefevre, P., Mutin, P.H., Vioux, A. "Preparation of monolithic gels from silicon halides by a non-hydrolytic sol-gel process", J.Non-Cryst. Solids, 146 (1992), pp. 301-303

[Corriu 1992C] Corriu, R.J.P., Leclercq, D., Lefevre, P., Mutin, P.H., Vioux, A. "Preparation of monolithic metal-oxide gels by a non-hydrolytic sol-gel process", J. Mater. Chem., 2 (1992), pp. 673-674

[Dearing 1928] Dearing, A.W., Reid, E.E. "Alkyl orthosilicates", J. Am. Chem. Soc. 50, (1928), pp. 3058-3062

[Goel 1992] Goel, S.C., Chiang, M.Y., Gibbons, P.C., Buhro, W.E. "New chemistry for the sol-gel process: Acetone as a new condensation reagent", Mater. Res. Soc. Symp. Proc., 271 (1992), pp. 3-13

[Hench 1990] Hench, L.L., West, J.K. "The sol-gel process", Chem. Rev., 90 (1990), pp. 33-72

[Hubert-Pfalzgraf 1998] Hubert-Pfalzgraf, L.G. "Some aspects of homo and hetero-metallic alkoxides based on functional alkohols", Coord. Chem. Rev., 178-180 (1998), pp. 967-997

[Inoue 2004] Inoue, M. "Glycotheral synthesis of metal oxides", J. Phys.: Condens. Matter, 16 (2004), pp. 1291-1303

[Jolivet 2000] Jolivet, J.P. "Metal oxide chemistry and synthesis", John Wiley & Sons Ltd., (2000), pp. 168

[Jun 2006] Jun, Y.W., Choi, J.S., Cheon, J. "Shape control of semiconductor and metal oxide nanocrystals through nonhydrolytic colloidal routes", Angew. Chem. Int., 45 (2006), pp. 3414-3439

[Kerber 2004] Kerber, A.; Cartier, E.; Pantisano, L.; Degraeve, R.; Groeseneken, G.; Maes, H.E.; Schwalke, U. "Origin of the threshold voltage instability in $SiO_2/HfO_2$ dual layer gate dielectrics", Microelectron. Eng. 72 (2004), pp. 267-272

[Kominami 1993] Kominami, H., Inoue, M., Inui, T. "Formation of niobium double oxides by the glycothermal method", Catal. Today, 16 (1993), pp. 309-317

[Levy 2015] Levy, D.; Zayat, M. "The Sol-Gel Handbook: Synthesis, Characterization and Applications", John Wiley & Sons, (2015), pp.1650

[Livage 1988] Livage, J., Henry, M., Sanchez, C. "Sol-gel chemistry of transition metal oxides", Prog. Solid State Chem. 18 (1988), pp. 259-341

[Mehrotra 1997] Mehrotra, R.C., Singh, A. "Recent trends in metal alkoxide chemistry", Prog. Inorg. Chem. 46, (1997), pp. 239-454

[Mitzi 2009] Mitzi, D. "Solution Processing of Inorganic Materials", John Wiley and Sons, (2009), pp. 501

[Niederberger 2007A] Niederberger, M., Antonietti, M. "Nanomaterials chemistry: Recent developments and new directions, chap. Nonaqueous sol-gel routes to nanocrystalline metal oxides", Wiley-VCH, (2007), pp. 119-138

[Niederberger 2007B] Niederberger, M. "Nonaqueous sol-gel routes to metal oxide nanoparticles", Acc. Chem. Res., 40 (2007), pp.793-800

[Park 2007] Park, J., Joo, J., Kwon, S.G., Jang, Y., Hyeon, T. "Synthesis of monodisperse spherical nanocrystals", Angew. Chem. Int.,46 (2007), pp. 4630-4660

[Pinna 2008]  Pinna, N., Niederberger, M. "Surfactant-free nonaqueous synthesis of metal oxide nanostructures", Angew. Chem. Int., 47 (2008), pp. 5292-5304

[Scriven 1988]  Scriven, L.E.; Brinker, C.D.; Clark, D.E.; Ulrich D.R. "Better Ceramics Through Chemistry", Materials Research Society, 111 (1988), pp. 717-729

[Turova 2002] Turova, N.Y., Turevskaya, E.P. "The chemistry of metal alkoxides", Kluwer Academic Publishers, (2002), pp. 573

[Wright 2000] Wright, J.D.; Sommerdijk, N.A.J.M. "Sol-Gel Materials: Chemistry and Applications", CRC Press, (2000), pp. 125

[Zhang 2009] Zhang, S. "Handbook of Nanostructured Thin Films and Coatings", CRC Press, (2010), pp. 1232

[Zhao 2005] Zhao, C.Z.; Zahid, M.B.; Zhang, J.F.; Groeseneken, G.; Degraeve, R.;De Gent, S. "Properties and dynamic behavior of electron traps in $HfO_2/SiO_2$ stacks", Microelectron. Eng., 80 (2005), pp.366-369

### 3. Sol-gel fabrication of Erbium activated $SiO_2$-$HfO_2$-$P_2O_5$ planar waveguides

Silica glass ($SiO_2$ glass) is one of the most important materials in optical and electrical applications, i.e., as optical fibers and insulators in semiconductor devices [Righini 2002]. Considering that it has many attractive properties, such as high UV transparency, high mechanical strength, high glass transition temperature, extremely low thermal expansion, and low reflective index, it has various potential uses in many optical devices, such as in waveguides and lasers. However the needs for compact and efficient photonic devices obtained by rare earth ions activated glasses still drive the research of novel glass composition and optimized fabrication protocols [Righini 2005, Righini 2014]. Considering the case of silica glass-based Erbium Doped Waveguide Amplifiers (EDWAs) their short length (around few centimetres) generally imposes a high $Er^{3+}$ doping level which may produce clustering effects [Righini 2009]. These phenomena, due to the ion-ion interactions, lead to undesirable luminescence quenching, thus reducing the performance of the amplifier. At the same time the difficulty of low solubility of rare-earth in silica is due to the mismatch in size and valence between the rare-earth ions and the constituents of the silica network. A possible way to increase the amounts of rare-earth ions in the matrix avoiding or reducing clustering effects is the addition of co-doping agents, such as $P_2O_5$ or $Al_2O_3$ [Deschamps 2012, Lemaire 1989]; their role resides in non-bridging oxygens formation that benefits better rare-earth ions incorporation. Moreover from a technological point of view physical and chemical deposition techniques such Flame Hydrolysis Deposition (FHD) and Plasma Enhanced Chemical Vapor Deposition (PECVD) have important drawbacks associated to the incorporation of rare earth ions in silicate glasses due to the high process temperatures in the first case [Kik 1998], and the low vapour pressure of most Erbium compounds in the second [Ribeiro

2000]. Therefore there is a need to investigate complementary approaches for depositing Er-doped silicate glass, which can incorporate the full range of codopants needed to tailor the Er environment. One possibility is the sol-gel route, which allows very flexible chemistry and low process temperatures.

In this chapter we have investigated planar waveguides with compositions $(70-x)$ $SiO_2$-$30HfO_2$ -$xP_2O_5$ (x= 5, 10  mol. %), activated by 0.5 mol. % $Er^{3+}$ ions. We used different Phosphorus precursors focusing the attention of their influence on the optical and spectroscopic properties.

### 3.1. Experimental part and discussion

Multilayer wave guiding films activated with rare-earths were produced by sol-gel approach employing the motor driven dip-coating set-up. For film-forming, solution $(70-x)SiO_2$-$30HfO_2$ -$xP_2O_5$ (x= 5, 10 mol. %), activated by 0.5 mol. % $Er^{3+}$ ions was prepared by mixing tetraethylorthosilicate (TEOS), ethanol, deionised water and hydrochloric acid as a catalyst, then pre-hydrolysed for 1 hour at 65 °C. A second solution was obtained by dissolving $HfOCl_2 \cdot 8H_2O$ as Hafnia precursor in ethanol and then added to the TEOS solutions. Phosphorous and Erbium $Er(NO_3)_3 \cdot 5H_2O$ precursors were mixed with final solution. Synthesis occurred under continuous stirring for 16 h at room temperature. The films were deposited on clean silica substrates with roughness of about 2 nm. Films were formed by dip-coating, with a dipping rate of 40 mm/min. After each dip, layer was subjected to annealing in air for 50 s at 900 °C. After a 10-dip cycle, the film was heated for 2 min at 900 °C after each tenth layer. In order to obtain a fully densified structure a further annealing at 900 °C for 5 min was performed [Righini 2005]. The thickness and the refractive index at 632.8 and 543.5 nm were measured in TE polarization by an m-line apparatus based on the prism coupling technique [Tien 1970, Shuto 1993]. The losses at 632.8 were evaluated by photometric detection of the light intensity scattered out of the waveguide plane exciting the transverse electric $TE_0$ mode. Photoluminescence spectroscopy was performed using the 514.5 nm line of an $Ar^+$ ion laser as excitation source. The lumines-

cence was dispersed by a 320 mm single-grating monochromator with a resolution of 2 nm. The light was detected using a Photo Multiplier Tube (PMT) and standard lock-in technique [Gonçalves 2004]. Decay curves were obtained recording the signal by a digital oscilloscope.

The choice of a suitable Phosphorous precursor (PP) is a key point towards the realization of low losses waveguides operating at 1.5 μm with high $Er^{3+}$ ions content. Several PPs (reported in Table 3.1.1) have been investigated for the synthesis of a dielectric stable sol useful for the realization of planar waveguides.

The composition and the optical parameters of the $Er^{3+}$-activated silica-hafnia-phosphorous oxide planar waveguides (called Wx) are reported in Table 3.1.1.

**Table 3.1.1.** Phosphorous precursors and optical properties of $SiO_2$–$HfO_2$–$P_2O_5$ planar waveguides activated with 0.5% mol of $Er^{3+}$ ions.

| Label | Phosphorous precursors | $P_2O_5$ mol. % | Layers number | Thickness ±0.3 μm | | Refractive index ±0.0005 | | TE Modes number |
|---|---|---|---|---|---|---|---|---|
| | | | | @632.8 nm | @543.5 nm | @632.8 nm | @543.5 nm | |
| W1 | $C_6H_{15}O_3P$ | 5 | 5 | - | 0.2 | - | 1.5762 | 1 |
| W2 | $(CH_3CH_2O)_3PO$ | 10 | 18 | 0.8 | 0.8 | 1.5868 | 1.5940 | 2 |
| W3 | $(CH_4CH_9O)_3PO$ | 5 | 18 | 0.9 | 0.9 | 1.5716 | 1.5871 | 2 |
| W4 | $H_3PO_4$ | 5 | 30 | 1.4 | 1.4 | 1.5585 | 1.5676 | 3 |

The systems W1, W2 and W3 present an opaque and whitish appearance attributable to the low solubility in the matrix of the PPs, indicating that these reagents are not suitable for the realization of optical devices.

The use of $H_3PO_4$ as Phosphorous precursor permits to realize a waveguide (W4) that present a good transparency: over 92 % in a wide range from 400 to 2000 nm, as evidenced in Figure 3.1.2 by means of transmission measurement and allows to realize thick guiding film that support single mode at 1.5μm.
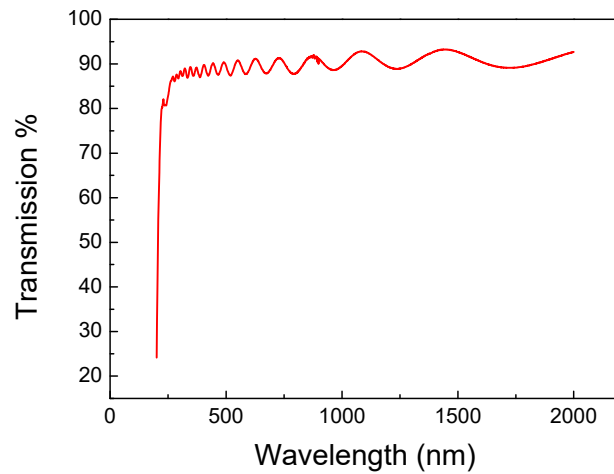
**Figure 3.1.2.** Transmission spectrum of the planar waveguide W4 doped by 0.5 mol. % $Er^{3+}$ ions.

Figure 3.1.3 and Figure 3.1.4 report the profile of the refractive index and of the $TE_0$ mode squared electric field of the waveguide W4, respectively. The $TE_0$ mode is computed for 632.8 nm and 1542 nm for the choice of the parameters determined by the m-line measurement.
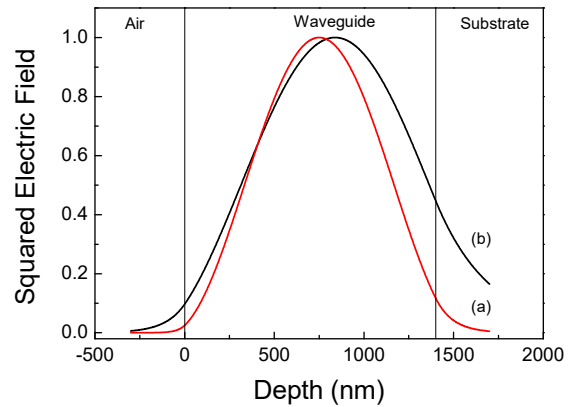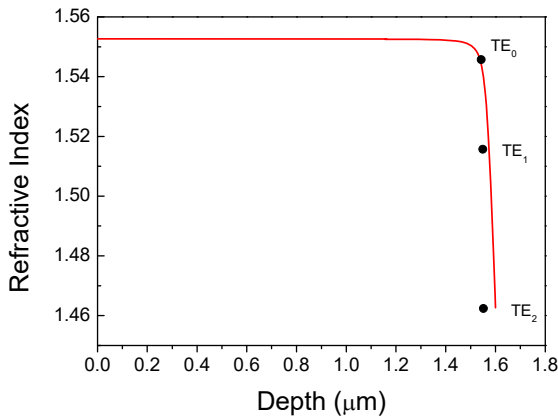
**Figure 3.1.3.** Refractive index profile of the W4 waveguide reconstructed from modal measurements at 632.8 nm for the TE. The effective indices of the TE (•) modes are reported.

**Figure 3.1.4.** Calculated squared electric field profiles of the $TE_0$ mode at 632.8 and 1532 nm (a) and (b), respectively, across the layered structure, cladding of air, waveguide and the $SiO_2$ substrate of the W4 planar waveguide

The refractive index profile of the W4 waveguide can be reconstructed from the effective refractive indices at 632.8 nm by an inverse Wentzel–Kramers–Brillouin method [Chiang 1985], in particular from Figure 3.1.3 we can observe that the W4 exhibits a single step profile with a uniform refractive index throughout the whole thickness.

The modelling of the square electric field, reported in Figure 3.1.4, indicates that the optical parameters of the waveguide, i.e. refractive index and thickness, appear appropriate for application in the third telecommunication window ($\lambda$=1.5 $\mu$m). In fact, the ratio of the integrated intensity, i.e. the square of the electric field in the waveguide to the total intensity, which includes also the squared evanescent field, is 0.98 and 0.87 at 632.8 nm and 1542 nm, respectively.

Photoluminescence measurements were performed in order to investigate the effect of $P_2O_5$, comparing the spectroscopic features of the W4 with those of a wave-

guide with the following molar composition $70SiO_2$-$30HfO_2$ activated with 0.5 mol. % (WU), doped with the same $Er^{3+}$ ions concentration.

In Figure 3.1.5 is reported the photoluminescence (PL) spectra of transition $^4I_{13/2} \rightarrow {}^4I_{15/2}$ of $Er^{3+}$ ions acquired from the sample WU and W4. Analyzing Figure 3.1.5 is possible to observe that luminescence shape is similar for both the samples with a main emission peak at 1533 nm and a spectral bandwidth of 48 nm, measured at 3 dB from the maximum of the intensity. The shape of the emission spectrum is characteristic of the $^4I_{13/2} \rightarrow {}^4I_{15/2}$ transition of $Er^{3+}$ ions in silicate glasses.



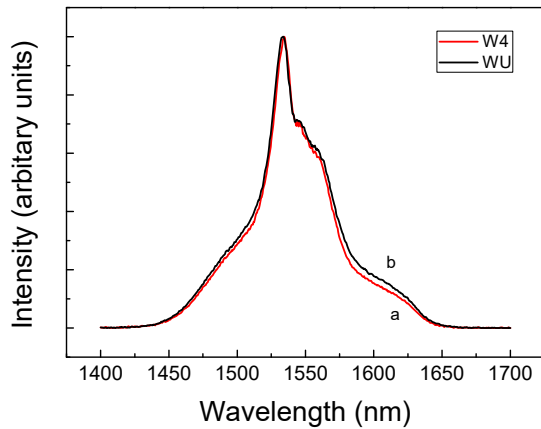**Figure 3.1.5.** Room temperature PL spectra relative to the $^4I_{13/2} \rightarrow {}^4I_{15/2}$ transition of $Er^{3+}$ ions for W4 and WU waveguides (a) and (b), respectively upon excitation at 514 nm.
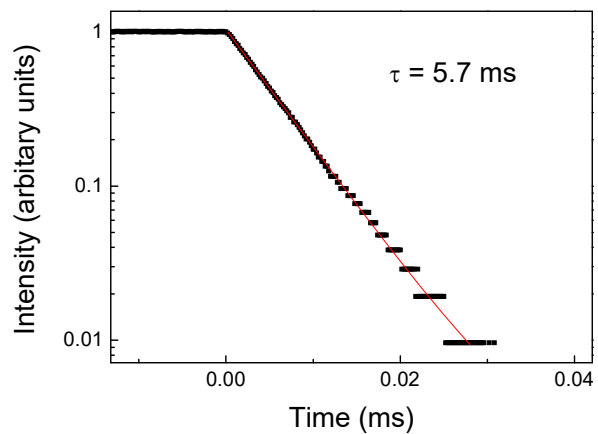
**Figure 3.1.6.** Decay curve of the luminescence from the $^4I_{13/2} \rightarrow {}^4I_{15/2}$ metastable state of $Er^{3+}$ ions for the W4 waveguide. The red solid line represents single exponential fits to the decay data.

Figure 3.1.6 reports the luminescence decay curve from the metastable level $^4I_{13/2} \rightarrow {}^4I_{15/2}$ for the W4 waveguide obtained upon excitation at 514 nm; we can notice that the decay curve exhibits a single exponential behavior, indicating that $Er^{3+}$ ions all occupy sites characterized by similar local environment and the value of the measured lifetime $\tau_{W4} = 5.7 \pm 0.1$ ms. This value can be compared with that obtained

on the sample WU ($\tau_{Wu}$= 5.1 ± 0.1 ms) and discussed in ref [Chiappini 2011]. The increase of the lifetime measured for the sample W4 with respect to WU can be attributed to the presence of $P_2O_5$ in the matrix indicating that the phosphorous oxide can increase the $Er^{3+}$ ions solubility.

In conclusion $Er^{3+}$ activated $65SiO_2$-$30HfO_2$-$5P_2O_5$ waveguides (WGs) were prepared via the sol-gel method and dip coating processing. We have studied the influence of the Phosphorous precursors on the optical properties of planar waveguides demonstrating that $H_3PO_4$ precursor allows to obtain a guiding transparent film. The waveguide realized (W4) supports a single and well confined (87 %) mode at 1.5 μm, presents a single step refractive index profile and an attenuation coefficient of about 3.5 dB/cm at 632.8 nm.

Luminescence in the third telecom region, with a spectral width of 48 nm and a single exponential lifetime of 5.7 ms, was observed upon excitation at 514.5 nm.

Finally the increase of the lifetime of the W4 with respect to that obtained on a complementary WG not codoped with $P_2O_5$ indicates that the Phosphorous oxide can increase the $Er^{3+}$ ions solubility reducing the concentration quenching.

# Bibliography

[Chiang 1985] Chiang, K.S. "Construction of refractive index profile profiles of planar dielectric waveguides from the distribution of effective indixes", J. Lightwave Technol., LT3 (1985), pp. 385-391

[Chiappini 2011] Chiappini , A.; Chiasera, A.; Armellini, C.; Varas, S.; Carpentiero, A.; Mazzola, M.; Moser, E.; Berneschi, S.; Righini, G.C.; Ferrari, M. "Sol-gel derived photonic structures: fabrication, assessement, and application", J. Sol-Gel Sci. Technol., 60 (2011), pp. 408-425

[Deschamps 2012] Deschamps, T.; Ollier, N.; Vezin, H.;,Gonnet, C. "Local environment of $Yb^{3+}$ in fiber preform codoped with Al and P and its relevance to photodarkening", J. Chem. Phys., 136 (2012), pp. 0145031

[Goncalves 2004] Goncalves, R.R.; Carturan, G.; Montagna, M.; Ferrari, M.; Zampedri, L.; Pelli, S.; Righini, G.C.; Ribeiro, S.J.L.; Messaddeq,Y. "Erbium-activated $HfO_2$-based waveguides for photonics", Opt. Mat., 25 (2004), pp. 131-139

[Kik 1998] Kik, P.G.; Polman, A. "Erbium-doped optical-waveguide amplifiers on silicon", MRS Bull., 23 (1998), pp. 48-54

[Lemaire 1989] Lemaire, P.J.; MacChesney, J.B.; Simpson, J.R. "Article comprising silica based glass containing aluminum and phosphorus", US4830463 A EP0328315A1, (1989)

[Ribeiro 2000] Ribeiro, S.J.L.; Messaddeq, Y.; Gonçalves, R.R.; Ferrari, M.; Montagna, M.; Aegerter, M.A. "Low optical loss planar waveguides prepared by an organic-inorganic hybrid system", Applied Physics Letters, 77 (2000), pp. 3502-3504

[Righini 2002] Righini, G.C.; Pelli, S.; Ferrari, M.; Armellini, C.; Zampedri, L.; Tosello, C.; Ronchin, S.; Rolli, R.; Moser, E.; Montagna, M.; Chiasera, A.; an Ribeiro, S.J.L. "Er-doped silica-based waveguides prepared by different tech-

niques: RF-sputtering, sol-gel and ion-exchange", Optical and Quantum Electronics, 34 (2002), pp. 1151-1166

[Righini 2005] Righini, G.C.; Ferrari, M. "Photoluminescence of rare-earth-doped glasses", Riv. Nuovo Cimento, 28 (2005), pp. 1-53

[Righini 2009] Righini, G.C.; Berneschi, S.; Nunzi Conti, G.; Pelli, S.; Moser, E.; Retoux, R.; Féron, P.; Gonçalves, R.R.; Speranza, G.; Jestin, Y.; Ferrari, M.; Chiasera, A.; Chiappini, A.; Armellini, C. "$Er^{3+}$-doped silica-hafnia films for optical waveguides and spherical resonators", Journal of Non-Crystalline Solids, 355 (2009), pp. 1853-1860

[Righini 2014] Righini, G.C.; Chiappini, A. "Glass optical waveguides: a review of fabrication techniques", Opt. Eng., 53 (2014), pp. 071819-1/14

[Shuto 1993] Shuto, K.; Hattori, K.; Kitagawa, T.; Ohmori, Y.; Horiguchi, M. "Erbium-doped phosphosilicate glass waveguide amplifier fabricated by PECVD", Electron. Lett., 29 (1993), pp. 139-141

[Tien 1970] Tien, P.K.; Ulrich, R. "Theory of the prism coupler and thin film light guides", JOSA, 60 (1970), pp. 1325-1337

## 4. Experimental

### 4.1 Requirements for substrates

The choice of the substrates depends on the type of measurements the films will be exposed to. In any circumstance, the substrate material should be chemically inert to the deposited films, have good compatibility to the deposition process and to be mechanically stable. The nature and surface quality of the substrates are critical because they affect the film properties and should be matched with the type of measurements. For instance, conductive atomic force microscopy requires samples with smooth surfaces for attaining reliable results.

### 4.2 Quality parameters of optical coatings

The optical coatings applied in laser technology should satisfy specific quality parameters given in the Table 4.2.1:

**Table 4.2.1.** Quality parameters of optical films [Träger 2012].

| Specification | Parameter | Unit | Standard | Measurement principle |
|---|---|---|---|---|
| Laser-induced damage threshold (LIDT) | cw-LIDT<br>1 on 1-LIDT<br>S on 1-LIDT<br>Certification | W/cm<br>$J/cm^2$<br>$J/cm^2$<br>$J/cm^2$ | ISO 11254-1<br>ISO 11254-1<br>ISO 11254-2<br>ISO 11254-3 | CW-laser irradiation. Irradiation with single pulses. Repetitive irradiation with pulses. Irradiation sequence |
| Optical losses | Absorptance<br>Total | Ppm<br>Ppm | ISO 11551<br>ISO 13696 | Laser calorimetry<br>Integration of scat- |

| | scattering | | | tered radiation |
|---|---|---|---|---|
| Transfer function | Reflectance Transmittance | % % | ISO 13697 ISO 15368 | Precise laser ratiometric method Spectrophotometry |
| Surface quality | Form tolerances Scratch/digs Roughness | λ/N | ISO 10110 | 14 parts containing different types of imperfections |
| Stability | Abrasion Environmental stability | | ISO 9211 ISO 9022 | Different test methods 21 parts containing a variety of conditioning methods |

The fundamental properties of the coating system must be adjusted for the optical device and application in the laser systems [Träger 2012, Czichos 2006]. In case when high laser powers or precision requirements are implicated, supplementary quality parameters relevant to the stability and optical losses of the coatings have to be analyzed. The absorbance has an effect to many applications of high-power lasers, because a fraction of the impinging radiation transforms energy into heat, and the temperature in the coating increase. This effect may influence the transfer behavior and result in thermal destruction of the optical component [Träger 2012, ISO/TR 22588 Geneva 2005]. Absorption always entails a loss of laser energy and guided by defects, contaminants, or stoichiometric inadequacy. Mainly, dielectrics due to stoichiometric inadequacy have got minor excess of the metal component, which is arise from coating decomposition during thermal evaporation or sputtering. The role of stoichiometric effects to absorbance behavior in the short-wavelength region whereas predominant contaminant in optical coatings, such as absorbed water, may lead to increase absorption value in the MIR spectral region, particularly at the wavelength

10.6 μm [Träger 2012, Rahe 1992] of the $CO_2$ laser or the band of the Ho:YAG and Er:YAG lasers in the range 2-3 μm [Träger 2012, Gross 1997]. Absorbance in laser components can be measured by the standard laser calorimetric investigation, as reported by ISO 11551 [Träger 2012, ISO 11551 Geneva 2003].

The second loss channel in optical components is a scattering [Träger 2012, Bennett 1999, Duparre 1995]. Scattering causes not only a reduction of the imaging quality of optical systems, but also economic loss of radiation and safety danger. Appearance origin of scattering losses in optical coatings is mainly associated to microstructural imperfections and inclusions in the coating, the roughness of the surface and the interfaces between the single layers [Träger 2012, Bennett 1999]. The theoretical model of scattering depending on the wavelength is described on the basis of a $1/\lambda^x$ function with an exponent of 1-4. Following this relation, high scattering losses in optical component are expected for the vacuum ultraviolet (VUV)/UV spectral range. Shifting towards longer wavelength, optical scattering decreases and can be even neglected in the MIR spectral range, where absorption losses are noticeable. There are number of different scattering measurement techniques for total scattering (TS) [Träger 2012, ISO 13696 Geneva 2002, ASTM 1987] and angle-resolved scattering (ARS) [Träger 2012, ASTM 1990]. Total scattering can be measured from the total amount of radiation scattered into the $4\pi$ full space by an optical component measurement apparatus with an Ulbricht integrating sphere [Träger 2012, Ulbricht 1990] or a Coblenz collecting sphere [Träger 2012, Coblentz 1913]. The measurement procedure is described in ISO 13696 [Träger 2012, Kadkhoda 2000A, Kadkhoda 2000B, Hultacker 2003]. The working principle of the Ulbricht sphere is based on the integration of scattered radiation from a reflecting coating on the inner wall of sphere and monitoring of part of the integrated radiation. The use of Coblenz sphere allows a direct collection and concentration of the scattered radiation onto the detector.

Specifically, the use of high-power laser enforces demands on the power-handling capability of optical coatings, which is practically means the laser-induced

damage threshold (LITD). A few material properties can limit the LITD values of coatings: melting point, the thermal conductivity or the band-gap energy [Träger 2012]. Moreover, extrinsic effects such as defects and inclusions in the layer structure or even any high-power mechanisms at the layer interfaces have to be taken into consideration [Träger 2012, Walker 1981]. Defect-induced damage mechanisms are noticed in optical coatings, which is described as a result of inclusions heating under laser radiation [Träger 2012, Walker 1981]. The damage is reached when the temperature in perimeter of inclusion is equal to the melting point of the surrounding coating material [Träger 2012, Ristau 1984].

In case of absorption-induced damage, the energy is directly coupled into the layer structure at the interface of interaction area with the laser beam. Then the temperature homogeneously increases until the damage temperature of the structure is attained [Träger 2012, Ristau 1984]. Typically, for short laser pulses (ps and fs), diffusion lengths of thermal effects are very small compared with the thickness of the layers structure and can be neglected.

### 4.3 Sputtering film deposition

There are number of physical vapor deposition techniques for producing coatings in a vacuum ambience and these can be distinguished into two groups: (i) thermal evaporation techniques when material is heated in vacuum until its pressure is higher than the ambient pressure; (ii) ionic sputtering methods when high-energy ions strike a solid and dispose of atoms from the surface. Ionic sputtering techniques include ion-beam sputtering, diode sputtering and magnetron sputtering [Swann 1988].

The early experiments on sputtering film deposition were realized in 1852 year in the laboratory of William Robert Grove. They announced about formation of a deposit in the anode of a gaseous discharge and its removal with polarity reversion. This scientific curiosity to the sputtering techniques was observed until the 1940s when diode sputtering experiments were first performed for commercial coatings process.

Then in the mid-1970s magnetic enhancement of the diode sputtering process was applied and this becomes known as magnetron sputtering.

The use of magnetron sputtering is explained by the potential to sputter wide range of materials for different fields of applications. Such high popularity of these deposition techniques can be described by the specific advantages of this approach:

- Stoichometry control

- Good film adhesion because of high kinetic energy of sputtered atoms

- Uniform deposition over a large area

- Good control of film thickness

- Other evaporation techniques require horizontal placement of the crucible containing molten material and vertical placement below the substrate, while sputtering works in any orientation

- Any conductive or insulating materials to any type of substrate can be applied for deposition, because sputtering is a cold momentum transfer process

- Substrate can be cleaned in sputtering chamber in a vacuum

- Using simultaneous deposition from multiple sources allows to develop new complex composition.

- Sputtering process has proved to be useful for large scale production

- By varying sputtering parameters, such as sputtering gas pressure biasing the substrate and target to substrate spacing is possible to achieve desired film parameters, for example, microstructure, composition, step coverage and etc.

- Film sputtering deposition can be performed in the presence of a reactive gas (i.e. oxides, nitrides)

The main limitations of the process are the low deposition rate, low ionization efficiencies and high substrate heating [Maurya 2014]. Magnetron sputtering is a high-rate vacuum coating technique for deposition of metals, alloys and other compounds with thickness up to 5 μm. This method has a few significant advantages over the other vacuum coating techniques and this has led to the development of a

number of commercial applications such as microelectronics fabrication or even simple decorative coating [Swann 1988].

In practice, use of magnetron is necessary to increase the efficiency of the sputtering process through increase of the number of collisions made by each secondary electron before it reaches the anode. Magnetic field confines the electrons in orbits close to the cathode [Kelly 1999]. Also electromagnets may be used instead of permanent magnets to generate the magnetic field which bind the electrons to orbit near the cathode. Use of electromagnets makes it possible to change the plasma position with respect to the cathode by varying the field strength in sets of magnets [Biltoft 2002].

Magnetron sputtering has many advantages such as sputtering of any compound, metal or alloy; high purity of films and high deposition rates; excellent adhesion of films and excellent coverage of surface; simplicity of automation; capability to use heat-sensitive substrates; simplicity of automation and superior uniformity of coating on large-area substrates [Swann 1988].

In magnetron sputtering, combination of magnetic and electric fields confines the plasma in front of the target (cathode). Magnetic field (about 50-200 mTorr) is bounteous to influence electrons, but not ions.

Then the electrons are subject to Lorenz force in addition to that due to the electric field:

$$F=-e(E+vxB) \qquad (11)$$

Magnetic field can be formed in different configurations; the most often used being the planar magnetron, because of its physical simplicity and the ability to extend the cathode to virtually any size required i. e. an evaporation characteristic of the emission volume. The magnetic field is caused but the bar magnets behind the target, emitting at suitable angles to the target and bend in such a way as to provide a component which is parallel to the surface of target. When electrons meet this magnetron component of the field, they are subjected to a force dedicating to bring them back towards the target with a cycloidal motion, leading to very high ionization effi-

ciency. For this reason, magnetron discharges can be maintained at much lower pressures ($<10^{-2}$ Pa) the glow discharges without magnetic support. This configuration of the magnets in the planar magnetron leads to a distinct region in which the electrons become confined. This place of the target is known as "racetrack" is abraded by virtue of the fact that there is high gas ionization directly above. At the same time the use of magnetron greatly increases the rate at which may be sputtered, that is also leads to less efficient use of the target material [Chapter 3, Biltoft 2002].

Also electromagnets may be used instead of permanent magnets to generate the magnetic field which bind the electrons to orbit near the cathode. Use of electromagnets makes it possible to change the plasma position with respect to the cathode by varying the field strength in sets of magnets [Biltoft 2002].

As it was explained before during the sputtering process atoms or molecules of a material are ejected from a target by the bombardment of high energy particles. The segment from which the atoms are rejected is known as the "target". Basically, the target is a plate of materials (oxides or nitrides) to be deposited or the material from which a film is obtained. The target is connected to the negative terminal of a DC or RF power supply and thus is also known as the cathode. The substrate on to which the film is grown faces the cathode. It may be heated, cooled, grounded, biased negatively or positively. In general, for thin film deposition, a dense target is heated by the bombarding ions; the electrode to which the target is bonded must be cooled. The back of the target is surrounded by ground shields or dark space shields, which are placed at such a distance that no discharge will be initiated in that place to abolish sputtering of the backing material [Chapman 1980, Shwartz 2006]. To proceed with sputtering successfully, a few criteria have to be accomplished. In the first instance, created ions must have sufficient energy and be directed towards the surface of a target to eject atoms from the material. Furthermore, ejected atoms must be able to move freely towards the matter to be coated with little impedance to their movement. That explains why sputtering process is performed in vacuum conditions: 1) to retain high ion energies; 2) to avert an enormous number of atom-gas collisions after ejec-

tion from the target. The use of term of mean free path is reasonable here. Mean free path (MFP) intends the average distance that atoms can travel without collisions with other gas atoms.

The sputtering chamber maintains the lowest pressure in order to create a clean environment. A highly pure Argon gas is usually used in sputtering process, which play a role of the chamber medium. A discharge is initiated and preserved.

The anode is grounded and a large negative potential applied to the cathode. Highly conductive plasma is produced between the plates; the applied voltage is dropped across the cathode, leading to ion bombardment. The gas pressure and applied voltage ranges required for the parallel plate glow discharge are around 3-300 Pa and 1000-2000 V respectively. Ions which encounter on the cathode surface generating secondary electrons. Acceleration of these electrons into the plasma, resulting in further ionizing collisions. The majority of the produced electrons will be not involved in collisions, escaping anode and making the process inefficient [Chapter 3].

The segments which are important for sputtering use the cathode dark space and the positive glow. The electrons are emitted from the cathode when a conduction conditions are stable. If the anode is moved closer to the cathode until it reaches the dark space the plasma extinguishes. Ions stop to be produced and sputtering process ceases. The size of the dark space increases when a gas pressure is decreased with a glow discharge, due to the larger MFP for electrons. This leads to the ions production far away from the target material where they can be lost to chamber walls.

Likewise, primary electrons may reach the anode without generating gas ionization. Consequently, the overall ionization efficiency becomes low, and below 1Pa the plasma and sputtering stops. Commonly this happens at pressures where MFPs are becoming convenient for a coating process. To overcome this problem is possible with a method of generating more efficient ionization at these lower pressures, this method is the magnetron design [Swann 1988].

Two sputtering types can be designated: dc (diode and triode) and ac (radiofrequency). These types functionates in two regimes: magnetron dc (balanced and un-

balanced) and magnetron ac (balanced and unbalanced). In the sputtering process the cathode electrode is the sputtering target and the substrate is placed on the anode in dc discharge [Vossen 1978]. In the zone near to the cathode appears the applied potential and plasma generates. In case of dc discharge is important that the cathode is an electrical conductor, because ion bombardment of the surface can be prevented by surface charge of insulating material. In that way dc sputtering is suggested to use for plain electrically conductive materials such as metals. DC approach is rather slow and expensive process compared to vacuum deposition. One of the advantages of dc sputtering is that the plasma can be established uniformly over a large area and a solid large-area vaporization source can be established. On the contrary, in dc sputtering the electrons ejected from the cathode are accelerated away from the cathode are not effectively used for discharge support. In order to avoid this effect, a magnetic field is applied to the dc sputtering system that can deflect the electrons to close to the target surface with proper magnets arrangement. Through film growth sputtering techniques, the electrons can be made to circulate very near on the target surface. In this event the high current of electrons initiates high-density plasma, from which ions can be extracted to sputter the target material, producing a magnetron sputter configuration [Penfold 1995]. A drawback of the magnetron sputtering regime is that the plasma is confined near the cathode and is not accessible to active/reactive gases in the plasma near the substrate for the reactive sputtering deposition [Windows 1986, Alfonso 2012].

Practically, about 1 % of the incident energy goes into the particle ejection, about 75 % into heating the bombarded surface, and the rest of the incident energy is dissipated by secondary electrons which heat the substrate. For particle ejection, the kinetic energy of the incoming ions should exceed the binding energy of the surface atoms of a solid. And sputtering looks as the results of a collision cascade, am outcome of independent binary collisions, what does not mean a simple interaction between an incoming ion and a surface atom [Shwartz 2006, Vossen 1978].

## 4.4 The main parameters of sputtering deposition process

The threshold energy is the minimum ion energy required for sputtering. This energy depends on the heat of sublimation of the target material and does not sensitive to the nature of the bombarding atoms. For the most part of the sputtering processes, the source of ions is an inert gas, typically Argon, but in reactive sputtering, depending on the material to be deposited Oxygen or Nitrogen is added.

The next important sputtering parameter is the yield. The yield is the number of atoms ejected for each incoming ion. It increases with ion energy, first exponentially at lower energies and then linearly, after reaching a plateu it decreases at very high energy. In practice, the yields are very low (~0.1) in the low energy range of exponential increase. Often the sputtering yield increase with increasing mass of the bombarding ion, but in some of the research for inert gas ion sputtering of copper show, that it depends also from the substrate [Almén 1961, Vossen 1978]. Molecular ions dissociate into energetic atoms upon collision with the surface of the target as though the individual atoms arrived separately [Steinbruckel 1984].

The composition of the deposited film is usually the same as of a homogeneous target. When a multicomponent target (for ex. an alloy), that has the atoms of different sputtering yields, an altered layer forms at the surface of the target. The component with the highest sputtering yield is preferentially removed, leaving the surface with the lower sputtering yield component. At steady state, the composition of the sputtered material form the altered layer onto the substrate is the same that of the target. If the target has the component which is volatile, the ion heating of the target may result in a difference in stoichiometry between the target and deposit, if the volatile component is added to the sputtering gas it can compensate the difference in stoichiometry.

The effect of operating conditions has also a significant influence on the sputtering process. The ion current for sputtering increases when the gas pressure is raising, but the ions energy decreases, the ultimate outcome is an increase in deposition rate, because the yield decreases slowly with decreasing energy in the used sputtering

energy range. At some pressure range, backscattering in the gas will lead to a rate decrease. Generally, the flow rate of the gas does not have any effect on the deposition rate, although the contaminants which are coming from the vacuum chamber, which are purged in a high flow, affects the rate [Jones 1968]. It is highly recommended to remove the contaminants, in order to reduce the probability of their incorporation into the growing film. The uniformity of the film can be increased by increasing the source-to-substrate distance, but the accumulation rate decrease at the same time. It should be mentioned that in some cases, not all of the material sputtered from the target on the substrate remains on the surface. Some of them can be resputtered or reemitted thermally. In a DC glow discharge the metals can be sputtered, but if the insulators are exposed to DC plasma a positive charge accumulates on the surface, which prevents further positive ion bombardment. This problem can be avoided in RF sputtering, when an RF potential is applied to a cooled metal electrode to which the insulating target is bonded.

At low frequencies (less than 50 kHz), the ions are considerable mobile that the electrodes easily alternate between being anode and cathode. The standard frequency fir RF sputtering is 13.56 MHz. At higher frequencies, two effects appears: 1) The power may be transferred through the insulating target from the cathode by capacitive coupling; 2) No need to maintain the secondary electrons in the cathode region, because the electrons oscillating in the glow region become sufficiently energetic to initiate ionizing collisions themselves [Chapter 3].

Therefore, the use of frequencies higher than 13.56 MHz is advantageous, because the ion energy decreases when the ion current increases. This results in higher deposition rates at lower target voltages. When the target voltage is reduced, the energy of the secondary electrons is also reduced, as the substrate heating.

Numerous film properties are affected by the deposition temperature, for this reason, temperature control is necessary. During the sputtering the substrates are heated by ion bombardment and secondary electrons, they temperatures could be different from the holder [Lamont 1979].

The sputter deposited films of fine quality can be obtained also at low temperatures. Nevertheless, this approach has the number of weak spots. First, is the high cost, because the systems can be very large, but the efficiency is quite low. Furthermore, the difficulty with implementation of the load locks in such systems is connected with a flake formation during wafer load or unloads. The flakes could be incorporated into the film, which are obviously decreasing the quality of the deposited films [Shwartz 2006].

## 4.5 Waveguide fabrication by magnetron RF sputtering technique

$SiO_2$-$HfO_2$-$P_2O_5$ waveguides activated by $Er^{3+}$ ions were prepared by magnetron RF-sputtering technique. Silica and Silicon substrates were used for film deposition. The substrates were cleaned before deposition step at 120 °C for 20 min. Sputtering deposition of the films was performed by using 8'' $HfO_2$ disks of 0.5 cm in diameter , 8'' $SiO_2$ of 5x14cm and PG1 specimen (multicomponent glass $69P_2O_5$-$15SiO_2$-$10Al_2O_3$-$5Na_2O$-$1Er_2O_3$).

Deposition conditions:

RF sputtering was used to deposit the SiHfP-based layers with the following sputtering conditions:

Power to target: 120 W

Sputtering gas (Ar) pressure: $3.8x10^{-7}$ mbar), $5.4x10^{-4}$ mbar in vacuum

Target to substrate distance: 20 cm

Target size : $HfO_2$: 0.5 cm diameter; $SiO_2$: 5x14cm

The residual pressure, before deposition was about $2x10^{-7}$ mbar. No heating during the sputtering was present. The used for sputtering gas was Argon at a pressure of $3.8x10^{-7}$ mbar and the applied power for sputtering was 120 W with a reflected power of 0 W. In order to reach an apporiate thickness of the film for one propagating mode at 1.5 μm the applied deposition time was 3h45min. Thermal annealing at 400 °C for 6h in air was used to achieve light propagation [Tosello 2001]. Micro-

fractures, cracking or bad cohesion may be prevented when SOS substrates undergo the thermal annealing at 400 °C before the film deposition process [Tosello 2001].

Deposition time: 70h at 120 W of RF power on the target

Final thermal treatment: 400 °C, 6h in air

## 4.6 Optical measurements

The thickness and refractive index of the waveguides were determined at 543.5 and 632.8 nm for TE and TM polarization by an m-line apparatus based on the prism coupling technique [Ribeiro 2000]. The attenuation coefficient was measured at 633, 1342 and 1532 nm by photometric detection of the light intensity scattered out of the waveguide plane, by exciting the $TE_0$ mode [Almeida 1997].

## 4.7 M-line measurements

M-line technique is an accurate and precise measurement of refractive index n and film thickness $w$ [Wu 2005]. M-line spectroscopy has been extensively studied by Pelletier at al. and Olivier and Peuzin and is nowadays applied in many laboratories [Pelletier 1989, Olivier 1978].

By contrast to other methods, M-line spectroscopy is more advantageous because it is nondestructive method which requires only angle measurement and gives an opportunity to determine the anisotropy of the layer. This method has some disadvantages, such as (i) the film must be thick enough to support at least two guided modes, (ii) the layer must be hard enough to be pressed against the base of a prism, (iii) the roughness of the film must be low, (iv) the substrate must be transparent at the required wavelength [Olivier 1978]. Table 4.7.1. [Christensen 1992] show comparison of some light wave coupling techniques.

**Table 4.7.1.** Comparison of some light wave coupling techniques [Christensen 1992].

| Techniques | Advantages | Disadvantages |
|---|---|---|
| Prism coupling | High efficicency; mode selective | Complex, difficult to align |
| End coupling | High efficicency for thick waveguides | Difficult to align for thin waveguides |
| Launch coupler | Tolerant of allignement | Long, thin taper required for thin waveguides |
| Grating coupler | Tolerant of alignement; mode selective | Lower efficiency |

The most widely-accepted methods are a prism coupling and end coupling techniques.

The highly efficient is a prism coupling method is one of the best ways to couple large amounts of light in planar waveguides [Tong 2013]. This technique is mode selective, but requires placement of prism on top of the waveguide with an accurate gap adjustment between the prism and the waveguide.

Simple and efficient end coupling technique requires that the input beam from the source has to be directed into the end of waveguide, requiring alignment accuracy as small as the waveguide thickness [Wu 2005].

Better efficiency for the thin waveguides is achieved using the tapered launch coupler, but fabrication of the tapered end is more difficult and makes the coupler end more fragile. The grating coupler is not efficient as the launch coupler, but this method is a mode selective.

The advantage and disadvantage of some coupling methods are summarized in Table 4.7.1 [Cristensen 1992].

## 4.8 Theoretical background and experimental details of prism-coupling technique

Prism coupling of the laser light to a planar waveguide is based on the angle of the light of incidence on the prism base θ (Fig.4.8.1). A necessary condition to have a coupling is only when $θ=θ_m$, it means that the phase velocity in direction x, $x(i)=C/n_p sinθ$ should be equal to the phase velocity $v_m$ of the m-th mode.

The light velocity is Cm the refractive index of the prism is $n_p$, synchronous angle θ and m is 0,1,2...

The effective indices $N_m$ may be find from the following equation:

$$N_m = \frac{C}{v_m} = n_p sinθ_m \qquad (12)$$

Using an angle at which the light falls on the entrance face of the prism $l_m$, before mentioned equation can be rewritten as following:

$$N_m = n_p sin\left(α + arcsin\left(\frac{sinl_m}{n_p}\right)\right) \qquad (13)$$

Where the foot angle of the prism is α. Dispersion equations for planar waveguides, where $n_0$ and $n_2$ are the refractive indices of the two media that are neighboring to the waveguide layer and λ is a vacuum wavelength:

$$\frac{ω}{λ} = \frac{1}{2π\sqrt{n^2 - N_m^2}}[mπ + tan^{-1}(\frac{\sqrt{n_0^2 - N_m^2}}{N_m^2 - n^2}) + tan^{-1}(\frac{\sqrt{n_2^2 - N_m^2}}{N_m^2 - n^2})] \quad (TE\ mode) \qquad (14)$$

$$\frac{ω}{λ} = \frac{1}{2π\sqrt{n^2 - N_m^2}}[mπ + tan^{-1}(\frac{n^2}{n_0^2}\frac{\sqrt{n_0^2 - N_m^2}}{N_m^2 - n^2}) + tan^{-1}(\frac{n^2}{n_2^2}\frac{\sqrt{n_2^2 - N_m^2}}{N_m^2 - n^2})] \quad (TM\ mode) \qquad (15)$$
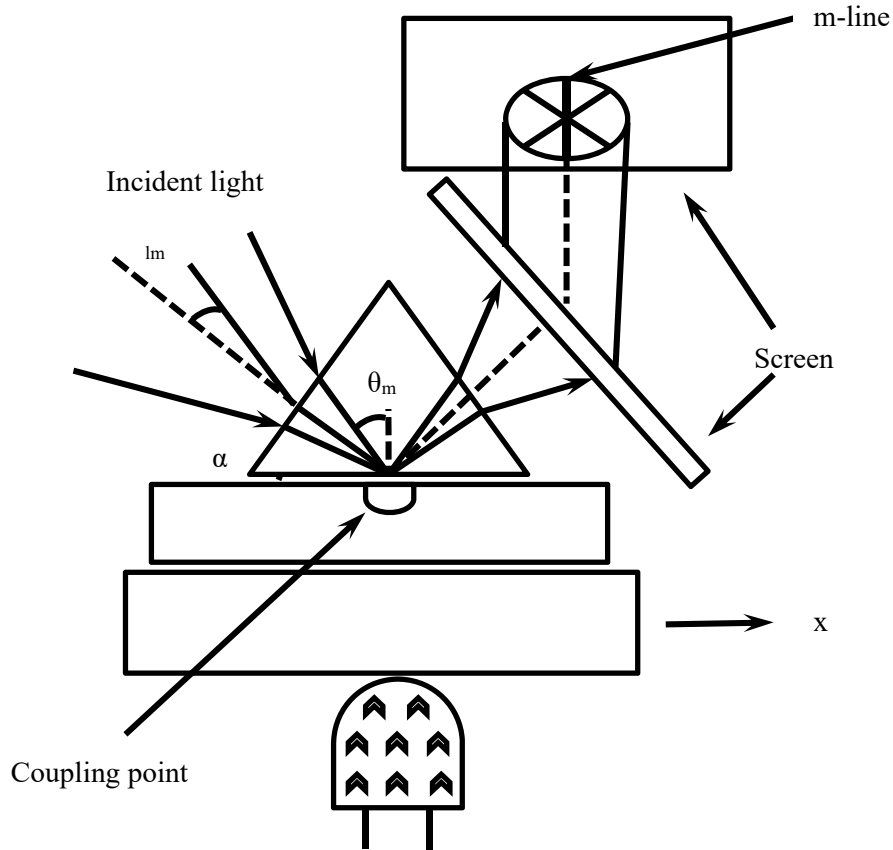
**Figure 4.8.1.** Prism coupling in MLS and MWMLS apparatus.

The last two equations allow determining two unknown parameters from more than two independent m-line measurements.

The refractive index and the thickness can be evaluated by tailoring the theoretical values of $N_m$ to the experimental values. The step-index model is satisfied when the measured and calculated values of $N_m$ agree to within one part in 1000 or better.

Other way to reconstruct refractive index profile *vs* film thickness is possible using an inverse Wentzel-KramerBrilloin (WKB) method. This approach is excellent if the change of refractive index is small. To use the WKB method, at least three should be present. By the way, higher the number of modes higher the accuracy is. [Chiang 1985, Wu 2005].

## 4.9 Prism coupling working principle

A Metricon[TM] automatic prism coupler was used for the most of the refractive index/thickness measurements during the characterization of processing parameters against optical layer properties [Khomchenko 2001, Tien 1970, Red'ko 1992]. The principal components of the Metricon[TM] optics module consist of one or more lasers, a reference slit, a position adjustment mirror, and a rotary table upon which the coupling prism and primary photodetector are mounted [Khomchenko 2001]. First the laser beam is passing through a small defining aperture, and then is directed onto the coupling prism by the adjustable mirror. A stepper motor drives the rotary table modifying the incident angle to reach a necessary phase matching condition Metricon[TM] model 2010 prism coupler. The coupling of light into the waveguide occur under total internal reflection conditions via evanescent waves in the air layer (Fig.4.8.1, Fig. 4.9.1). Recording and plotting of relative intensity against incident angle is accomplished by software. Software applies pattern recognition procedure to determine the minimum intensity, which is associated with coupling. The thickness and refractive index of the film is automatically calculated [PLSWA].
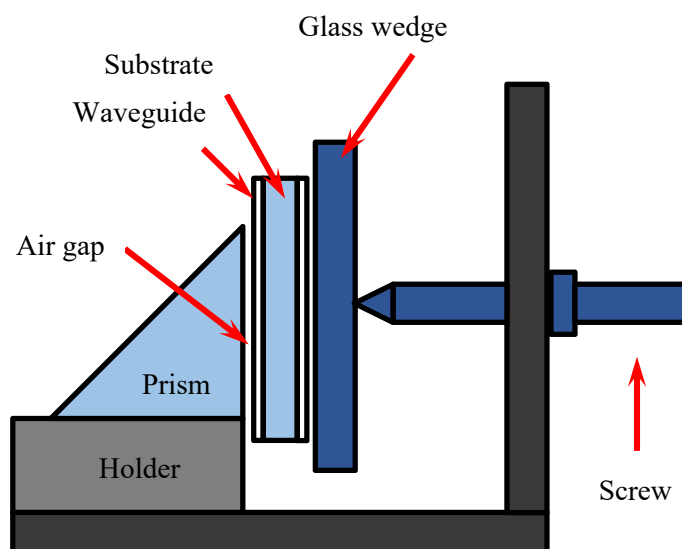


**Figure 4.9.1.** Scheme of prism coupling in the MLS apparatus [Wu 2005].

Inside the waveguide coupling occurs when resonant conditions are met. Hereafter, a finite number of discrete indices of the laser beam arise, for which the light can be coupled into the waveguide. The appearance of a dark line in the reflected beam signalize about resonant coupling of the laser beam into the waveguide film and excites a propagation mode, i.e. $\theta=\theta_m$ . Polarization of the incident light has influence on the the appearance of dark lines. Then the light reverses exactly in the direction of the incident beam. In fact this technique also automatically measures the thickness of the film with an uncertainty of less than 0.5 % [Elliot 2005].

Recording and plotting of relative intensity against incident angle is accomplished by software. After scanning procedure, the software applies pattern recognition process to determine the minimum intensity, which is associated with coupling. The thickness and refractive index of the waveguiding film are automatically calculated [PLSWA].

## 4.10 Propagation losses by diffusion

Appearance of diffusion is usually caused by the imperfections inside the waveguides or at the interfaces (waveguide/cladding layer or waveguide-substrate). These imperfections can limit light propagation because they partially diffuse of light by radiation. These defects appear as porosity, cracks, contaminants, grain boundaries and etc. Such imperfections can be formed during any waveguide fabrication process. Formation of sol-gel films requires strict care in order to reduce these film defects.

Cracks and pores are especially inescapable in sol-gel derived films because of organic components which must be eliminated during heat treatment. Pores in sol-gel waveguides appears with the removal of organic residues at high temperatures. Cracks occur due to the difference of thermal expansion coefficient of sol-gel coating and substrate due to the internal stress within the film. The light diffusion tends to increase with $1/\lambda$ , meaning that diffusion can be reduced at the longer wavelength. The size and the optical properties of these inhomogeneities play a significant role on their participation in the diffusion loss with the working wavelength. The propagation

losses increase when nanocrystals larger than 10-15 nm are present. In all cases, the propagation losses always exist in various degrees whatever the elaboration process. Optimization of elaboration process in order minimize or reduce the propagation losses is possible through an understanding of the structural and textural imperfections [Wu 2005].

## 4.11 Propagation loss measurements

Performance of optical integrated devices can be characterized by their optical attenuation [Tong 2014].

The losses related to each mode in a multimode waveguide can be determined using prism couplers where the prism slid along the streak in the waveguide and the ratio of light coupled in and out of the waveguide is identified as a function of the propagation length.

Fiber probe is also can be used to measure losses in a waveguide. In this technique the optical fiber is moving along the streak and the light scattered out of the waveguide is coupled into the fiber probe.

Both of techniques are characterized by a lack of accuracy and reproducibility, also sliding prism technique can damage the waveguide [Francis 2001]. In fiber moving probe technique (Fig. 4.11.1) we assume that the scattering centers in the waveguide are uniformly distributed and the intensity of the scattered light in the transverse direction is proportional to the number of scattering centers, and the intensity of the scattered light along the waveguide is proportional to the guided light intensity at each point. Keeping constant angular position and its distance from the waveguide is possible to obtain the plot of transmitted intensity propagation length by means of moving fiber probe. The fiber probe in combination with a microscope allows better control of the distance, improving the overall accuracy. The fiber probe may move to the waveguide until it touches surface and then with tracing it until it loses contact. The distant end of the fiber is connected to a detector, and output goes to a recorder.

This measurement should be repeated at several points along the streak, then by ana-lyzing the resulting trace it is possible to determine attenuation at 0.3 dB/cm.
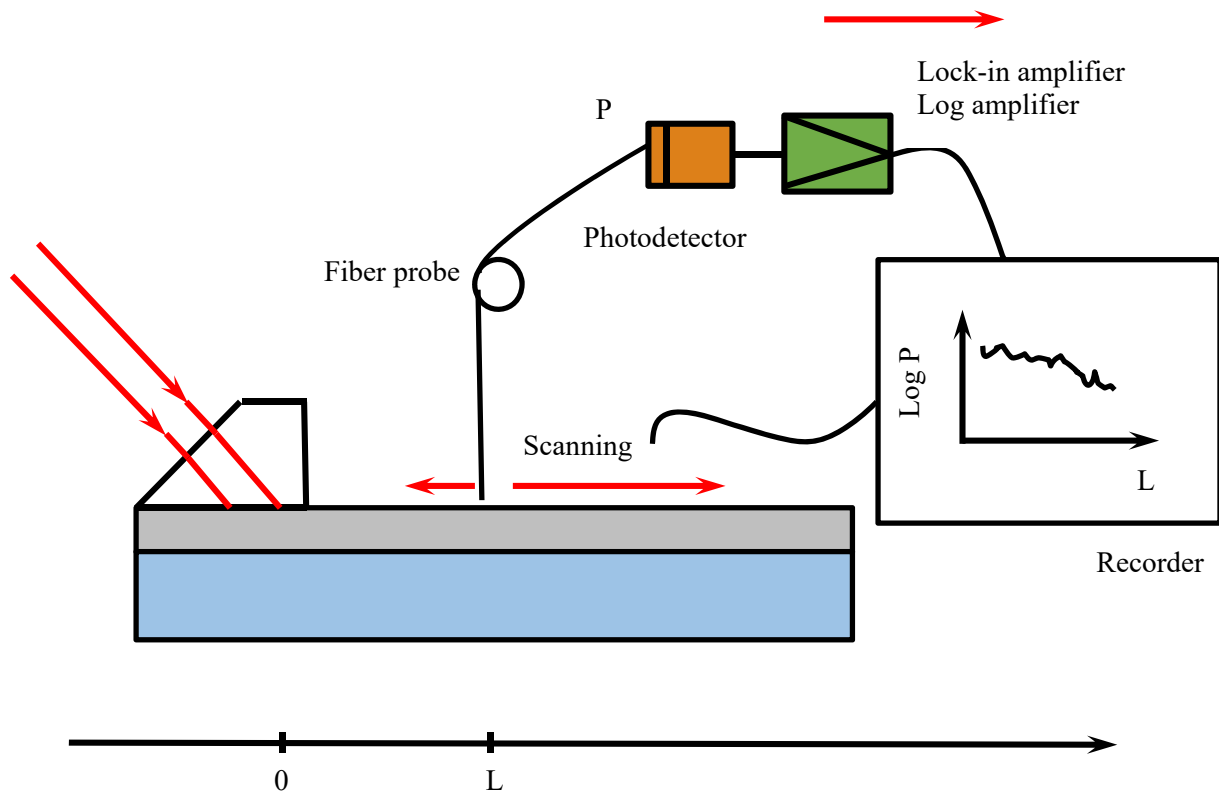


**Figure 4.11.1.** Fiber probe moving technique.

Waveguide propagation loss can be measured using of Fabry-Perot techniques. In this case the optical length of the waveguide or the wavelength of the source is varied over a short range with the monitored output intensity. The optical length of the waveguide can be changed by heating or cooling the sample, and the wavelength of the laser source can be varied by variations in the power supply current [Mentzer 2001].

# Bibliography

[Alfonso 2012] Alfonso, E.; Olaya, J.; Cubillos, G. "Thin Film Growth Through Sputtering Technique and Its Applications" , INTECH Open Access Publisher, (2012), pp. 36

[Almeida 1997] Almeida, B. G.; Amaral, V. S.; Sousa, J. B.; Colino, J.; Schuller, I. K.; Schad, R.; Moshchalkov, V. V.; Bruynseraede, Y. "Electrical resistivity behavior of Fe/Cr multilayers deposited by different techniques (molecular-beam epitaxy, sputtering), on different substrates (MgO,Si)", Journal of Applied Physics, Volume 81 (1997), pp. 5194-5196

[Almén 1961] Almén, O.; Bruce, G. "Sputtering experiments in the high energy region", Nuclear Instruments and Methods, 2 (1961), pp. 257-273

[ASTM 1987]  ASTM: ASTM Doc. F1048-87 "Standard test method for measuring the effective surface roughness of optical components by total integrated scattering", (1987)

[ASTM 1990]  ASTM: E1392-90 "Standard practice for angle resolved optical scatter measurements on specular or diffuse surfaces", (1990)

[Bennett 1999] Bennett, J.M.; Mattsson L. "Introduction to surface roughness and scattering", Optical society of America, 2 (1999), pp.130

[Biltoft 2002] Biltoft, Benapfl, and Swain, Vacuum Technology, 60A & 60B (2002), pp. 52-59

[Chapman 1980] Chapman, B. "Glow Discharge Processes: Sputtering and Plasma Etching", Wiley (1980), pp. 432

[Chapter 3] Chapter Three Experimental Techniques, pp.69-87

[Chiang 1985] Chiang, K.S. "Construction of refractive index profiles of planar dielectric waveguides from the distribution of effective indexes", J. Lightwave Technol., LT-3 (1985) pp. 385-391

[Christensen 1992]  Christensen, D.A.; Dyer, S.; Herron, J.N.; Hlady, V. "Comparison of robust coupling techniques for planar waveguide immunosensors", Pro-

ceedings of SPIE--the international society for optical engineering, 1796 (1992), pp. 20-25

[Coblentz 1913] Coblentz, W.W. "The diffuse reflecting power of various substances", Bull. Bur. Stand., 9 (1913), pp. 283–325

[Czichos 2006] Czichos, H.; Saito, T.; Smith, L. "Springer Handbook of Materials Measurement Methods", Springer Science, Business Media Inc. (2006), pp. 970

[Duparré 1995] Duparré, A. "Light scattering of thin dielectric films", Thin Films for Optical Coatings, CRC Press, (1995), pp. 273-303

[Duparré 2004] Duparre, A.; Ristau, D. "2004 topical meeting on optical interference coatings: Measurement problem", in Optical Interference Coatings, OSA Technical Digest Series, WD1 (2004)

[Elliot 2005] Elliot, T.B. "Focus on Semiconductor Research", Nova Publishers, (2005), pp. 237-239

[Francis 2001] Francis, T.S.; Yu, S.J.; Shizuhuo, Y. "Introduction to Information Optics", Elsevier, (2001), pp. 734

[Hultacker 2003] Hultacker, A.; Gliech, S.; Benkert, N.; Duparré, A. "VUV-Light scattering measurements of substrates and thin film coatings", Proc. SPIE , 5188 (2003), pp. 115–122

[ISO 13696 Geneva 2002] ISO 13696 "Optics and optical instruments -Test methods for radiation scattered by optical components", (2002), pp. 26

[ISO 11551 Geneva 2003] ISO 11551 "Optics and optical instruments - Lasers and laser-related equipment -Test method for absorptance of optical laser components", (2003), pp.13

[ISO/TR 22588 Geneva 2005] ISO/TR 22588 "Optics and photonics -Lasers and laser-related equipment -Measurement and evaluation of absorption-induced effects in laser optical components", (2005), pp.19

[Jones 1968] Jones, R.E.; Standley, C.L.; Maissel, L.I. "Reemission Coefficients of $SiO_2$ Films Deposited Through RF and DC Sputtering", J. Appl. Phys., 38 (1968), pp. 4656-4662

[Kadkhoda 2000A] Kadhoda, P.; Blaschke, H.; Kohlhaas, J,; Ristau, D. "Investigation of transmission and reflectance in the DUV/VUV spectral range", Proc. SPIE, 4099 (2000), pp. 311-318

[Kadkhoda 2000B] Kadhoda, P.; Welling, H.; Gunster, S.; Ristau, D. "Investigation on total scattering at 157 nm and 193 nm", Proc. SPIE, 4099 (2000), pp. 65-74

[Kelly 2000]  Kelly, P.J.; Arnell, R.D. "Magnetron sputtering a review of recent developments and applications", Vaccum, 56 (2000), pp. 159-172

[Khomchenko 2001] Khomchenko, A. V. "Spatial Fourier spectroscopy of guided modes in low-dimensional structures", Appl. Opt., 41 (2002), pp. 4548-4551

[Lamont 1979] Lamont, L.T. "Thermal history of substrates during sputtering and sputter etching", Solid State Tech., (1979), pp. 107-112

[Maurya 2014] Maurya, D.K.; Sardarinejad, A.; Alameh, K. "Recent Developments in R.F. Magnetron Sputtered Thin Films for pH Sensing Applications- An Overview", Coatings, 4 (2014), pp. 756-771

[Mentzer 2011] Mentzer, M. "Applied Optics Fundamentals and Device Applications: Nano, MOEMS, and Biotechnology", CRC Press, (2011), pp. 368

[Olivier 1978] Olivier, M.; Peuzin, J.C. "Characterization of silicon layers via guided wave optics", Appl. Phys. Lett. 32 (1978), pp. 386-388

[Pelletier 1989] Pelletier, E.; Flory, F.; Hu, Y. "Optical characterization of thin films by guided waves", Appl. Opt., 28 (1989), pp. 2918-2924

[Penfold 1995] Penfold, A. S. "Handbook of Thin Film Process Technology", Bristol: IOP Publishing, A3.2.1 (1995)

[PLSWA] "Production of layers and structures suitable for waveguiding applications", online

[Rahe 1992] Rahe, M.; Detlev, R.; Holger , S. "Effect of hydrogen concentration in conventional and IAD coatings on the absorption and laser-induced damage at 10.6 μm", Optical Materials for High Power Lasers. International Society for Optics and Photonics, 1848 (1992), pp. 335-348

[Red'ko 1992] Red'Ko, V. P.; Romanenko, A. A.; Sotskii, A. B.; Khomchenko, A. V. "A method for determining the complex mode propagation constants of optical waveguides", Pis'ma v Zhurnal Tekhnicheskoi Fiziki, 18 (1992), pp. 14-18

[Ribeiro 2000] Ribeiro, S.J.L.; Messaddeq, Y.; Gonçalves, R.R.; Ferrari, M.; Montagna, M.; Aegerter, M.A. "Low optical loss planar waveguides prepared by an organic-inorganic hybrid system", Applied Physics Letters, 77 (2000), pp. 3502-3504

[Ristau 1984] Ristau, D.; Dang, X.C.; Ebert, J. "Interface and bulk absorption of oxides layers and correlation to damage threshold at 106 µm", NBS Spec. Publ., 727 (1984), pp.298-312

[Shwartz 2006] Shwartz, G.C.; Srikrishnan, K. V. "Handbook of Semiconductor Interconnection Technology", CRC Press, (2006), pp. 536

[Steinbruchel 1984] Steinbruchel, C.H. "Reactive Ion Beam Etching", J. Vac. Sci. Technol., 2 (1984), pp. 38-44

[Swain 1988] Swain, S. "Negative Cross-correlation in the Quantum-beat Laser", Journal of Modern Optics, 35 (1988), pp. 1-5

[Tien 1970] Tien, P.K.; Ulrich, R. "Theory of the prism coupler and thin film light guides", JOSA, 60 (1970), pp. 1325-1337

[Tong 2013] Tong, X.C. "Advanced Materials for Integrated Optical Waveguides", Springer Series in Advanced Microelectronics, (2013), pp. 552

[Tong 2014] Tong, X.C. "Advanced Materials for Integrated Optical Waveguides", Springer, 46 (2014), pp. 53-102

[Tosello 2001] Tosello, C.; Rossi, F.;Ronchin, S.; Rolli, R.; Righini, G.; Pozzi, P.; Pelli, S.; Fossi, M.; Moser, E.; Montagna, M.; Ferrari, M.; Duverger, C.; Chiappini, A.; De Bernardi, C. "Erbium-activated silica-titania planar waveguides on silica-on-silicon substrates prepared by rf sputtering" , Journal of Non-Crystalline Solids, 284 (2001), p. 230-236

[Träger 2012] Träger, F. "Springer Handbook of Lasers and Optics", Springer, (2012), pp.1694

[Ulbricht 1990] Ulbricht, R. "Die Bestimmung der mittleren räumlichen Lichtintensität durch nur eine Messung", Elektrotechnische Zeitschrift, 29 (1900), pp, 595-597

[Vossen 1978] Vossen, L.J.; Cuomo, J.J "Thin film processes", Academic Press, (1978), pp.1-24

[Walker 1981] Walker, T.W.; Guenther, A.H.; Nielsen, P. "Pulsed Laser-induced Damage to Thin-Film Optical Coatings", IEEE J.Quantum Electron., (1981), pp. 2041-2053

[Willamowski 1998] Willamowski, U.; Ristau, D.; Welsch, E. "Measuring the absolute absorptance of optical laser components", Appl. Opt., 37 (1998), pp. 8362-8370

[Windows 1986] Window, B.; Savvides, N. "Unbalanced DC Magnetrons as a Sources of High Ion Fluxes", J. Vac. Sci. Technol., A4 (1986), pp. 453-456

[Wu 2005] Wu, K. "Towards system-on-substrate approach for future millimeter-wave and photonic wireless applications", APMC, IEEE, (2006), pp. 1895-1900

Chapter 5

**5. $SiO_2$-$P_2O_5$-$HfO_2$-$Al_2O_3$-$Na_2O$ planar waveguide was fabricated by**

**RF-sputtering technique**

**5.1 Sputtering protocol**

In Table 5.1.1 is reported the molar concentrations of the components in the planar waveguide W08 obtained by EDXS.

**Table 5.1.1.** Molar concentrations of the components in the W08 waveguide obtained by energy dispersive spectroscopy. The estimated error is 10 %.

| $SiO_2$ | $P_2O_5$ | $HfO_2$ | $Al_2O_3$ | $Na_2O$ | $Er_2O_3$ |
|---|---|---|---|---|---|
| 90.7 mol. % | 4.4 mol. % | 2.3 mol. % | 1.7 mol. % | 0.7 mol. % | 0.2 mol. % |

The deposition parameters such as RF power applied to the target, Ar pressure during the deposition, temperature of the target and sample holder, ect., have to be monitored because they influence the optical, spectroscopic and structural properties of the films.

For that reason, the apparatus allow to monitor and control different parameters during the various deposition process steps. In Figure 5.1.2 is reported the detailed schema of the apparatus used during this activity.
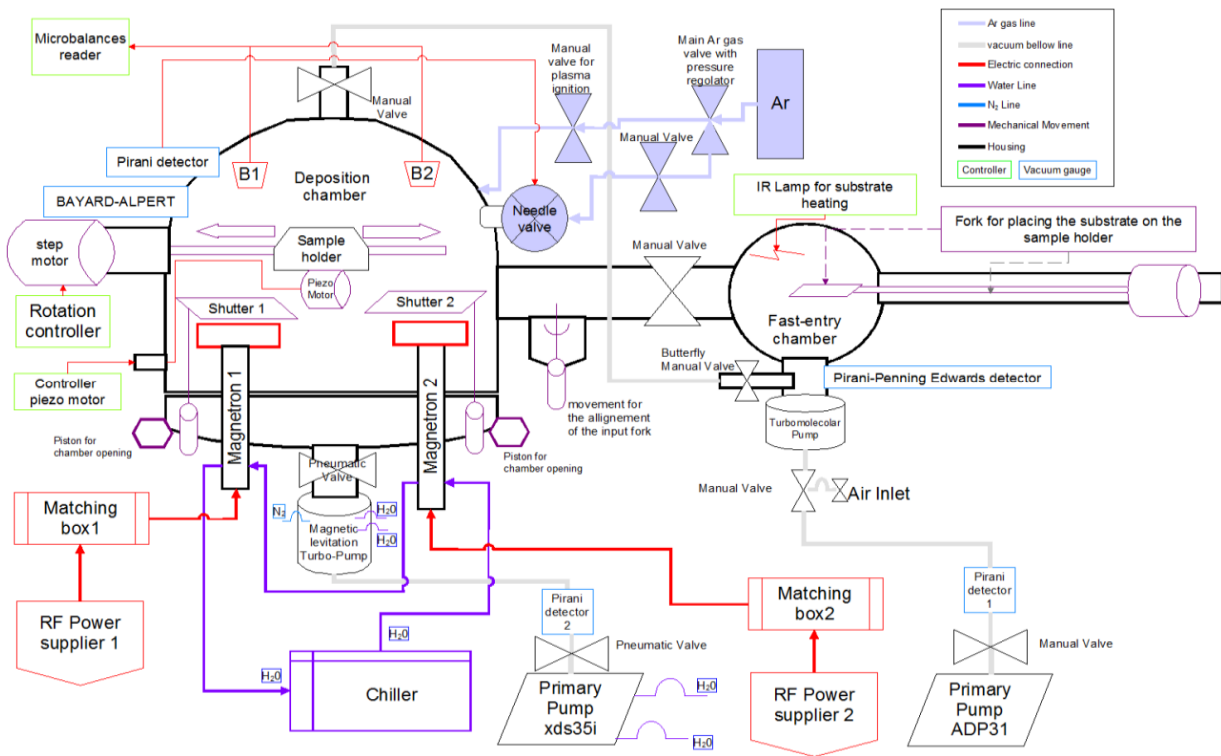
**Figure 5.1.2.** Schema of the RF-sputtering deposition setup.

The system allows to use 2 target in the same time but for our activity only one target was used: the target was composed by a $SiO_2$ plate on which 8 tablets of $HfO_2$ and the phosphate sample PG1 was placed as shown in Figure 5.1.3.
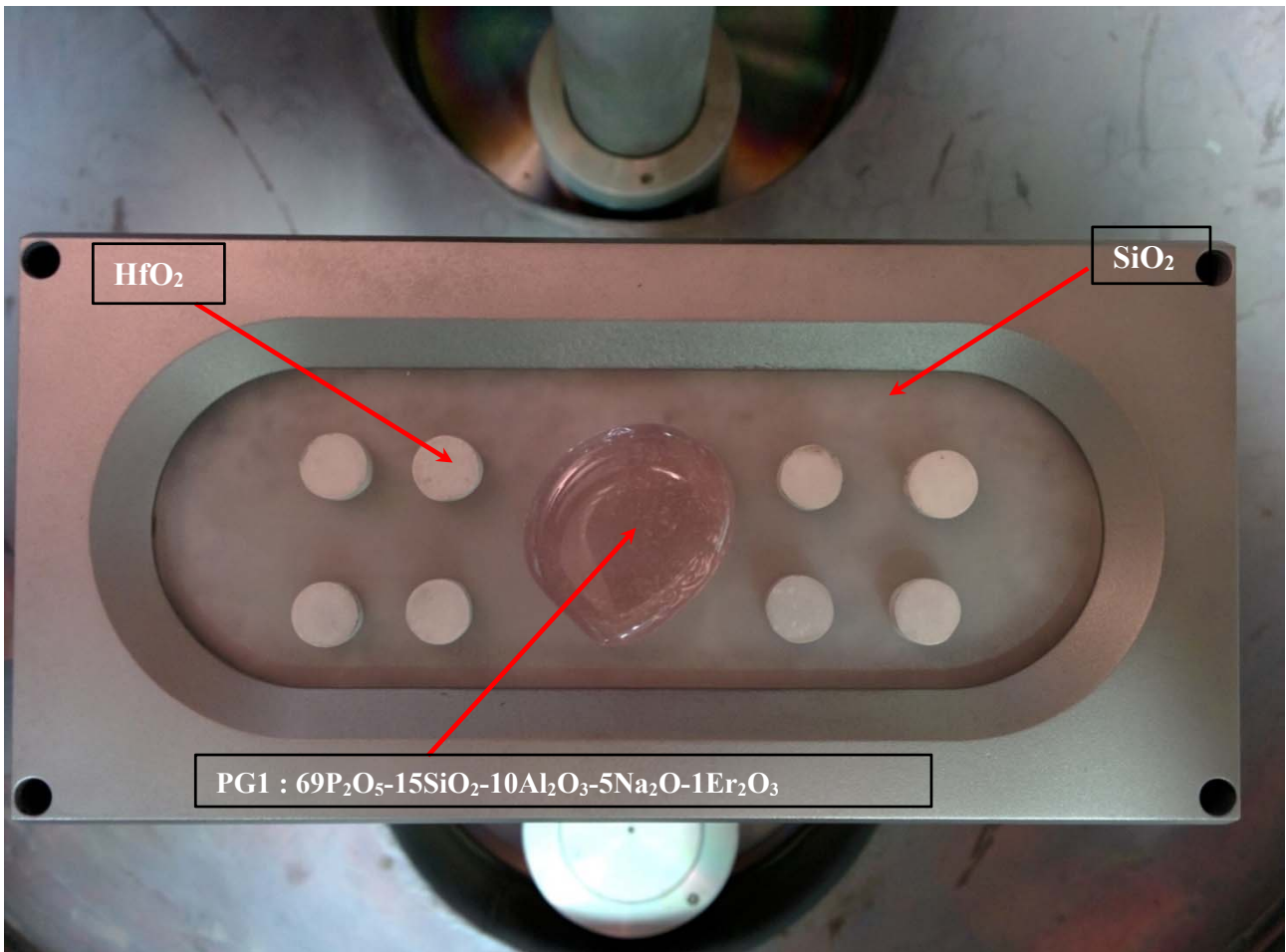
**Figure 5.1.3.** Photograph of the multicomponent target used to fabricate the activated waveguides; $HfO_2$: 0.5 cm diameter; $SiO_2$: 5x14 cm.

The sputtering apparatus is made up of two chambers, one where the deposition take place and one called fast-entry chamber used for the insertion end removing of the samples. The pumping system is oil free what allows to avoid contamination during the deposition also for long operation time.

In order to optimize the adhesion of the films on the substrate an accurate cleaning of the substrate surfaces is required: before the insertion of the sample in the fast-entry chamber the substrate are cleaned by soap, after cleaned in an ultrasonic bath in deionized water, polished with ethanol and finally dried in a Nitrogen flux [Waite 2007].

Moreover, when they are inserted in the fast-entry chamber the substrates are heated by a IR lamp at 120 °C for 20 minutes in a pressure of $10^{-6}$ mBar, this opera-

tion allows to remove contamination still stuck on the surfaces. This cleaning protocol was previously defined for the fabrication of planar waveguides in order to optimize the attenuation coefficient of the fabricated samples [Chiasera 2009, Chiasera 2013].

After the cleaning inside the fast-entry chamber the substrate are loaded in the deposition chamber and placed above the used target. The base pressure in the deposition chamber is maintained at around $10^{-7}$ mBar while the deposition take place in Ar atmosphere and the pressure is kept at $5.4*10^{-3}$ mBar. Before the effective deposition as the plasma is ignited above the considered target all the shutters are maintained close, this operation allow to clean the surface of the target without contaminate the substrates and stabilize the temperature of the magnetron that is controlled by a Chiller that keep a water flux in it with a temperature between 16 to 19 °C. This pre sputtering operation last 20 °C. The RF power on the magnetron is kept at 100 W during the pre-sputtering procedure while for the deposition it is increased at 120 W. The Matching networks are needed to provide maximum power transfer between the source and the magnetron. If RF circuit is not properly matched, we get reflected power on the power supplier and this could be damaged. Moreover the matching network contributes to keep the average potential on the target negative, at a value called Vbias, and therefore keep the flux of $Ar^+$ ions of the plasma towards the target.

When the shutter above the considered target is open the deposition start. The thickness of the sample is also defined by the time duration of the deposition process but other parameters concur to define the deposition rate and to monitor the growth of the films a quartz microbalance is placed above the target, close to the sample holder, more detail on the calibration and resolution of this thickness monitor can be found here [Valligatla 2012].

As deposited the film present a under stoichiometry in oxygen and a thermal treatment is performed in air at 400 °C for 6h [Tosello 2001].

## 5.2 RF-sputtering

A sputtering system consists of an evacuated chamber, a target (cathode) and a substrate table (anode) as shown in Figure 5.2.1. In the sputtering process, gas ions out of plasma are accelerated towards a target consisting of the material to be deposited. Material is detached ("sputtered") from the target and afterwards deposited on a substrate in the vicinity. The process is realized in a closed recipient, which is pumped down to a vacuum base pressure before deposition starts. To enable the ignition of the plasma, usually argon is fed into the chamber. By natural cosmic radiation there is always some ionized $Ar^+$ -ions available. In the dc-sputtering a negative potential $U$ up to some hundred Volts is applied to the target. As a result, the $Ar^+$ -ions are accelerated towards the target and set material free, on the other hand they produce secondary electrons. These electrons cause a further ionization of the gas. The gas pressure $p$ and the electrode distance $d$ determine a break-through voltage $U_D$ (at which the self-sustaining glow discharge starts) [Wasa 1992]:

$$U_D = A \cdot pd/(ln(pd) + B) \qquad (16)$$

with materials constants $A$ and $B$.

The ionization probability rises with an increase in pressure and hence the number of ions and the conductivity of the gas also increase the break through voltage drops. For a sufficient ionization rate a stable burning plasma results, where from a sufficient amount of ions is available for sputtering of the material. To increase the ionization rate by emitted secondary electrons even further, a ring magnet below the target is used in the magnetron sputtering. The electrons in its field are trapped in cycloids and circulate over the targets surface. By the longer dwell time in the gas they cause a higher ionization probability and hence form a plasma ignition at pressures, which can be up to one hundred times smaller than for conventional sputtering. On the one hand higher deposition rates can be realized thereby. On the other hand, fewer collisions occur for the sputtered material on the way to the substrate because of the lower pressure and hence the kinetic energy at the impact on the substrate is higher. The electron density and hence the number of generated ions is high-

est, where the B-field is parallel to the substrate surface. The highest sputter yield happens on the target area right below this region. An erosion zone is formed which follows the form of the magnetic field. The bombardment of a non-conducting target with positive ions would lead to a charging of the surface and subsequently to a shielding of the electrical field. The ion current would die off. Therefore the dc-sputtering is restricted to conducting materials like metals or doped semiconductors. To produce dielectric films, RF-sputtering (radio frequency) is used where an ac-voltage is applied to the target. In one phase ions are accelerated towards the target surface and sputter material. In the other phase charge neutrality is achieved [Smith 1995]. Hereby also sputtering of non-conducting materials is possible. Alternatively, for reactive sputtering other gases like oxygen or nitrogen are fed into the sputter chamber additionally to the Argon, to produce oxidic or nitridic films.
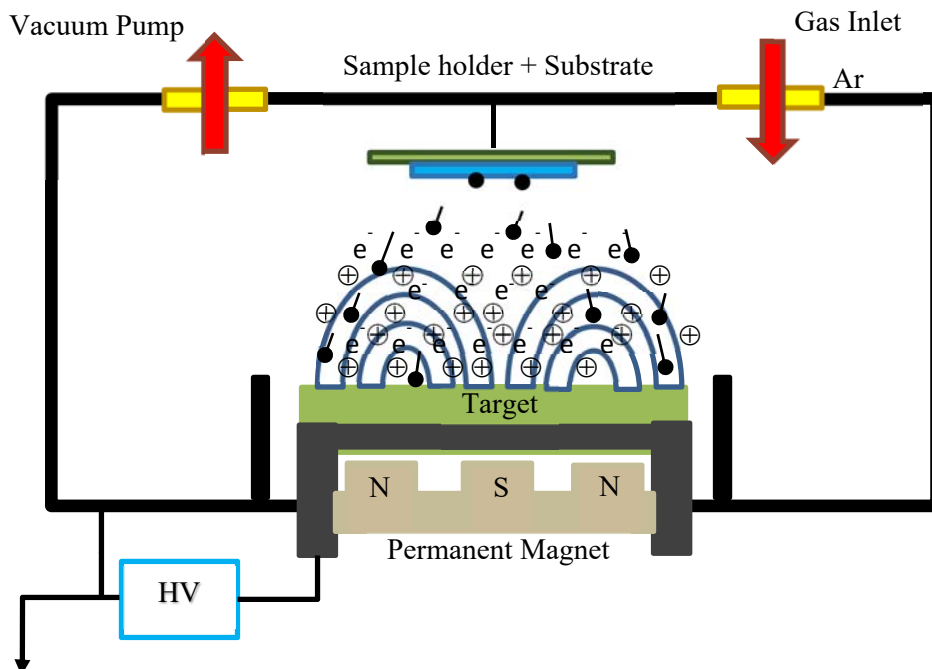
**Figure 5.2.1.** The schematic of a sputtering system.

## 5.3. Optical and spectroscopical properties

The refractive index at 632.8, 1319 and 1542 nm were measured in TE and TM polarizations, by a m-line apparatus based on the prism coupling technique. The thickness of the massive samples was measured by a micrometer while the thickness of the planar waveguide was directly obtained by m-line apparatus.

The refractive index at 632.8, 1319 and 1542 nm were measured in TE and TM polarizations, by a m-line apparatus based on the prism coupling technique. The thickness of the massive samples was measured by a micrometer while the thickness of the planar waveguide was directly obtained by m-line apparatus.

In Table 5.3.1 are presented the optical parameters of the phosphate bulk samples (PG0 and PG1 parent glasses) measured by m-line apparatus at 632.8, 1319 and 1542 nm in TE and TM polarizations and the thickness measured by a micrometer.

**Table 5.3.1**. Optical parameters of bulk phosphate glasses measured by m-line apparatus.

| Sample Label | Refractive index (± 0.0005) | | | | | | Thickness (mm) ±0.01 |
|---|---|---|---|---|---|---|---|
| | 633 nm | | 1319 nm | | 1542 nm | | |
| | TE | TM | TE | TM | TE | TM | |
| **PG0** | 1.5109 | 1.5113 | 1.5009 | 1.5040 | 1.4974 | 1.4986 | 5.47 |
| **PG1** | 1.5196 | 1.5201 | 1.5091 | 1.5088 | 1.5062 | 1.5073 | 5.40 |

The refractive index values reported in Table 5.3.1 shows that increasing the Erbium concentration the refractive index at all the wavelength is also increase at all the wavelength while the birefringence is negligible. The bulk glasses are characterized by a significantly higher refractive index relative to the pure silicate matrix making them attractive for active waveguide fabrication.
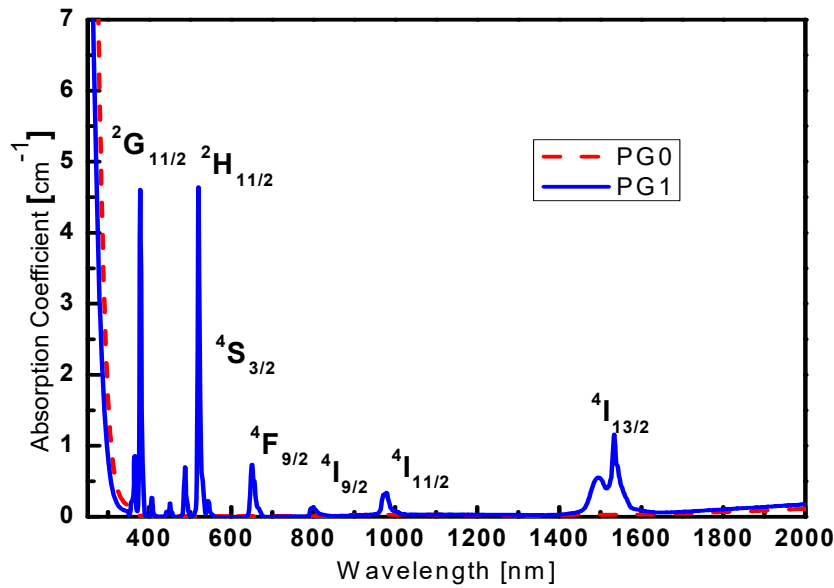
**Figure 5.3.2.** Room temperature absorption spectrum in the UV-Vis-NIR spectral region of the PG1 (continuous line ━━) and PG0 (dash line ─ ─) glasses. Some of the final states of the $^4I_{15/2} \rightarrow {}^{2S+1}L_J$ transitions are labeled.

The absorption spectrum of the PG0 and PG1 glasses in the UV-Vis-NIR is presented on Figure 5.3.2. The spectrum of PG1 glass is characteristic of $Er^{3+}$-doped glasses [Hehlen 1997]. The band which is located at around 1540 nm is related to the $^4I_{15/2} \rightarrow {}^4I_{13/2}$ transition of the $Er^{3+}$ ions.

These glass samples show a wide transparency from 350 nm and they are suitable for low loss waveguides fabrication

Using M-line technique is possible to obtain the optical characteristics of the planar waveguide. Two modes at 633 nm and one mode at 1319 and 1542 nm in presented in the waveguide. The results of optical and spectroscopic investigations of phosphate doped waveguides are reported in the Table 5.3.3.

**Table 5.3.3.** Optical and spectroscopic properties of  phosphate waveguides.

| Sample | Composition | Refractive Index | | | Attenuation coefficient (dB/cm) | | | Thickness (μm) | FWHM (nm) | Life time (ms) |
|---|---|---|---|---|---|---|---|---|---|---|
| | | 633 | 1319 | 1542 | 633 | 1319 | 1542 | | | |
| **W02** | $SiO_2$ target+ PG1 sample+8 pieces of $HfO_2$ | 1.49 | 1.479 | 1.477 | 0.6 | 0.4 | 0.4 | 3.1 | 33.5 | 0.7 |
| **W03** | $SiO_2$ target+ PG1 sample+8 pieces of $HfO_2$ | 1.485 | 1.474 | 1.471 | 0.6 | 0.4 | 0.3 | 2.9 | 29.5 | 1.10 |
| **W04** | $SiO_2$ target+ PG1 sample+8 pieces of $HfO_2$ | 1.489 | 1.48 | 1.478 | 0.6 | 0.4 | 0.3 | 3.6 | 34 | 1.75 |
| **W05** | $SiO_2$ target+ PG1 sample+8 pieces of $HfO_2$ | 1.488 | 1.477 | 1.474 | 0.4 | 0.3 | 0.3 | 2.6 | 32 | 1.97 |
| **W06** | $SiO_2$ target+ PG1 sample+4 pieces of $HfO_2$ | 1.482 | 1.471 | 1.468 | 0.3 | 0.25 | 0.25 | 2.9 | 32 | 3.3 |
| **W07** | $SiO_2$ target+ PG1 sample+4 pieces of $HfO_2$ | 1.475 | 1.468 | 1.465 | 0.25 | 0.2 | 0.2 | 3.1 | 34 | 3.47 |
| **W08** | $SiO_2$ target+ PG1 sample+2 pieces of $HfO_2$ | 1.479 | 1.468 | 1.465 | <0.2 | <0.2 | <0.2 | 3 | 28.5 | 5 |

| W10 | SiO$_2$ target+ PG1 | 1.468 | 1.458 | 1.455 | 0.3 | 0.2 | 0.2 | 3.4 | 28.5 | 3.8 |
| W11 | SiO$_2$ target+ PG1 | 1.472 | 1.461 | 1.458 | 0.3 | 0.2 | 0.2 | 3.4 | 29 | 3.4 |

**Table 5.3.4.** Optical parameters of the W08 phosphate planar waveguide  measured by M-line apparatus.

| Sample Label | Refractive | Index | | Attenuation | coefficient | | Thickness |
| | ±0.001 | | | (dB/cm) ±0.2 | | | (µm) ±0.1 |
| | 633nm | | 1319nm | 1542nm | 633nm | 1319nm | 1542nm | |
| | TE | TM | | | | | | |
| W08 | 1.478 | 1.479 | 1.468 | 1.465 | <0.2 | <0.2 | <0.2 | 3.0 |

From the Table 5.3.4 is noticeable that the W08 waveguide presents the thickness about 3 µm. The waveguide W08 supports two propagating modes at 633 nm in TE and TM polarization, the birefringence is negligible.
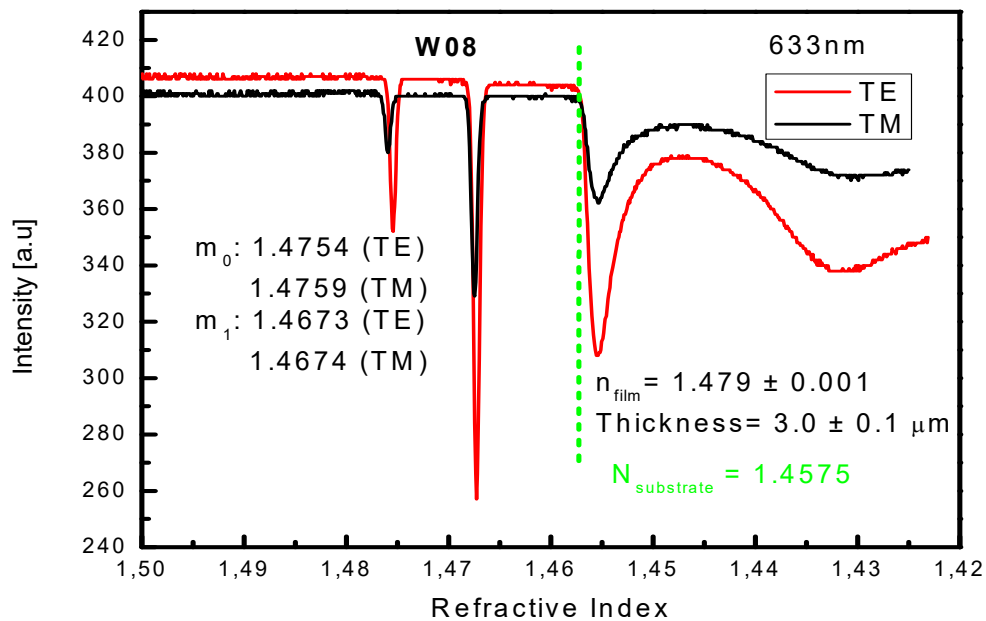


**Figure 5.3.5.** M-line curve for W08 at 633nm.
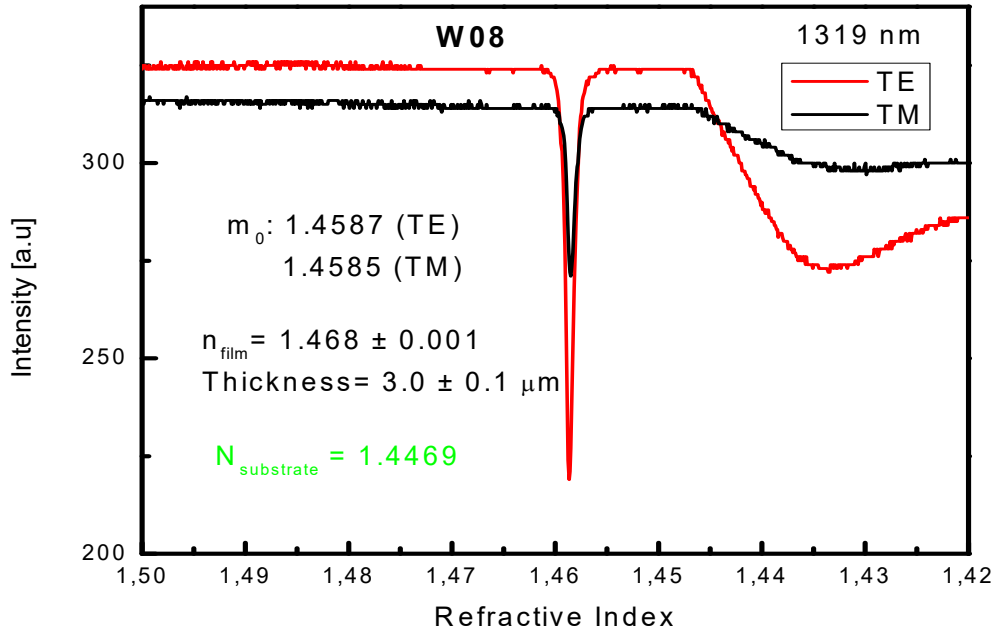
**Figure 5.3.6** M-line curve for W08 at 1319 nm.
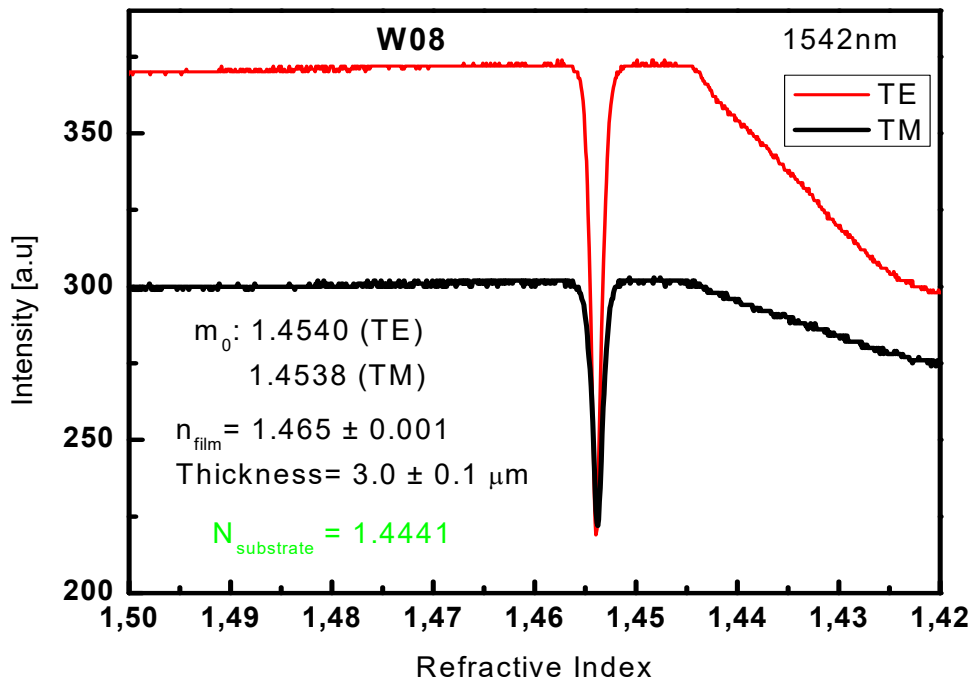


**Figure 5.3.7.** M-line curve for W08 at 1542 nm.

The calculated electric field profile of the TE modes of W08 waveguide at 1542 nm is shown in Figure 5.3.8.
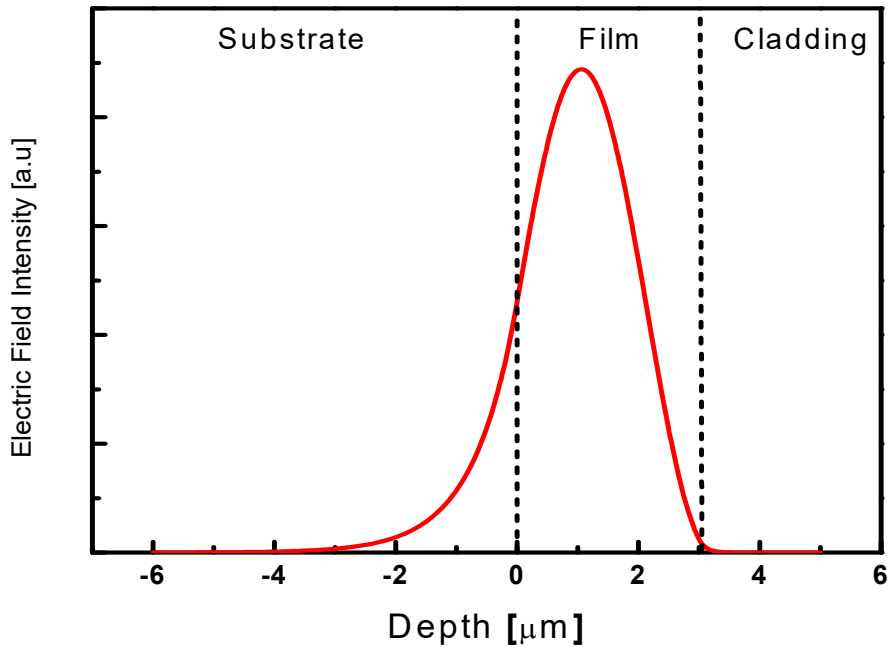


**Figure 5.3.8.** Calculated electric field profile of the $TE_0$ mode at 1542 nm across the layered structure consisting of cladding of air, waveguide and $SiO_2$ substrate of the W08 waveguide.

As it is shown in Figure 5.3.8 of the $TE_0$ modelling at nm indicates that the optical parameter of theW08 waveguide appear appropriate for application in the 1.5 μm region. The ratio of the integrated field intensity inside the waveguide to the total intensity, including also the evanescent fields, is 0.84.
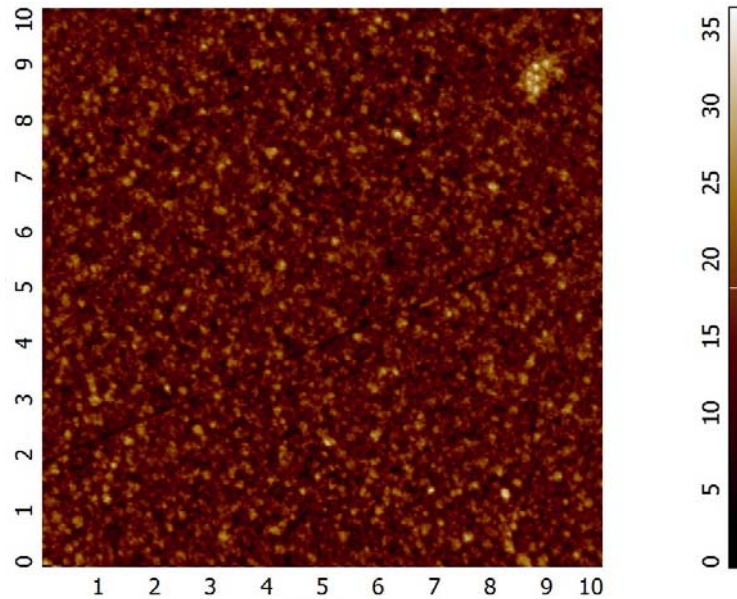
**Figure 5.3.9.** AFM images of representative 10x10 $\mu m^2$ area of the W08 waveguide.

The AFM measurements of 10x10 $\mu m^2$ area of W08 waveguide are presented in Figure 5.3.9. The average roughness was determined about 3.3 nm ($SiO_2$ substrate average roughness of about 0.5 nm).

A room temperature photoluminescence spectrum (PL) of an $Er^{3+}$ doped $SiO_2$-$P_2O_5$-$HfO_2$-$Al_2O_3$-$Na_2O$ planar waveguides was obtained using the 514.5 nm line of an $Ar^+$ ion laser as excitation source. The planar waveguide was excited by prism coupling technique in the $TE_0$ mode while the bulk glass was excited focusing direct-ly the laser beam on the sample. The luminescence was dispersed by a 320 mm sin-gle-grating monochromator with a resolution of 2 nm. The light was detected by us-ing a Hamamatsu photomultiplier tube and standard lock-in technique. The lifetimes were measured using a photomultiplier detector and analyzed using a Tektronix TDS 350 2 channel oscilloscope. More details about the experimental setup can be found in the ref [Chiasera 2009]. Luminescence from the excited $^4I_{13/2}$ is observed with a main emission peak of W08 deposited sample at 1537 nm and a spectral bandwidth of 48 nm. The shape of the emission spectrum is characteristic of the $^4I_{13/2}{\rightarrow}^4I_{15/2}$ transition of $Er^{3+}$ ions in silicate glasses [Orignac 1999, Yeatman 1999, Goncalves

2002, Zampedri 2001]. The bandwidth and the shape of the PL spectra of the other erbium-activated waveguides are the same respect to the reported spectrum, according to constant site-to-site inhomogeneities in the matrix.

The luminescence spectra of the W08 planar waveguide and the PG1 parent glasses are reported in Figure 5.3.10. The two spectra are recorded with the same spectral resolution and exciting the samples with the same laser at 514.5 nm.
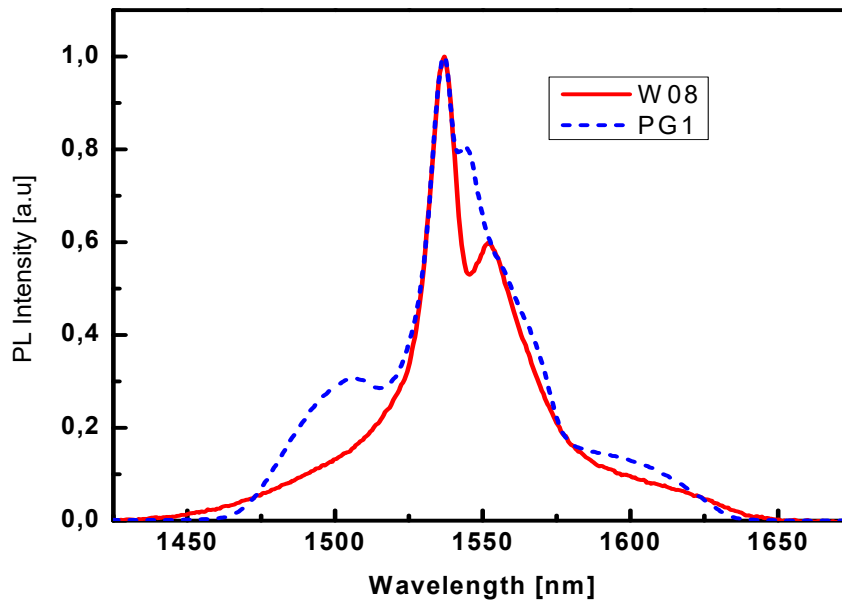


**Figure 5.3.10.** Room temperature photoluminescence spectra related to the $^4I_{13/2} \rightarrow {}^4I_{15/2}$ transition of $Er^{3+}$ ions from W08 planar waveguide (continuous line ——) and PG1 parent glass (dash line — —) upon excitation at 514.5nm. The spectra are normalized to the maximum.

Luminescence from the excited $^4I_{13/2}$ is observed with a main emission peak of W08 deposited sample at 1537 nm and a spectral bandwidth of 28 ± 0.5 nm. The spectrum obtained from the PG1 glasses appear different in comparison with the W08 spectrum and exhibits a bandwidth of about 30.5 ± 0.5 nm. The shape of the emission spectrum is characteristic of the $^4I_{13/2} \rightarrow {}^4I_{15/2}$ transition of $Er^{3+}$ ions in silicate glasses [Orignac 1999, Yeatman 2000, Goncalves 2002, Zampedri 2001, Chiasera 2009].

The bandwidth and the shape of the photoluminescence spectra indicate homogenous local crystal field distribution.
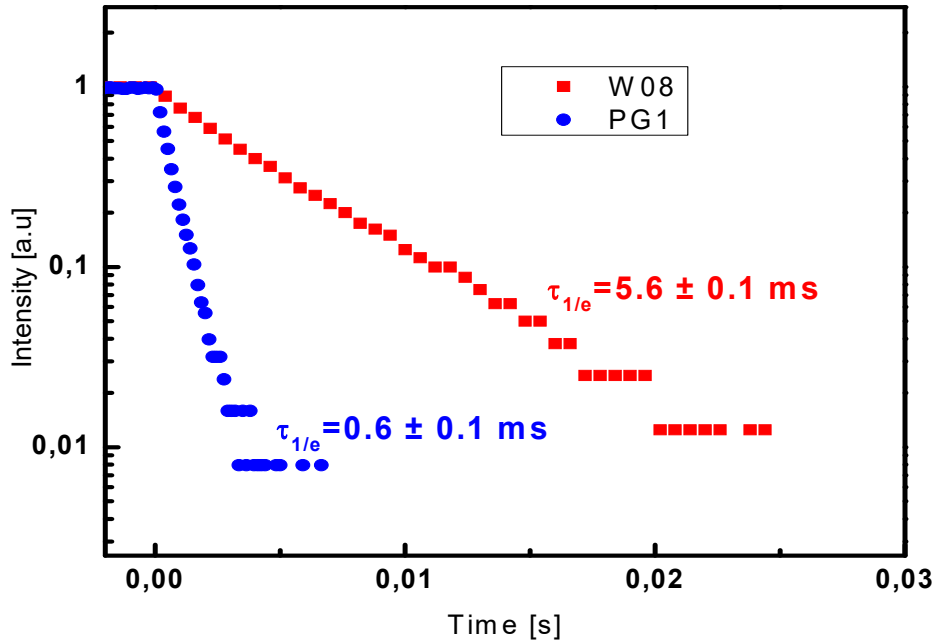


**Figure 5.3.11.** Decay curves of the luminescence from the $^4I_{13/2}$ metastable state of $Er^{3+}$ ions for (squares ■) W08 planar waveguide; (circles ●) PG1 parent glass.

The Figure 5.3.11 shows the measured luminescence decay curves of the metastable $^4I_{13/2}$ state of $Er^{3+}$ ions for W08 planar waveguide and PG1 parent glass. The $^4I_{13/2}$ decay curves present a single exponential profile with lifetime of 5.6 ms and 0.6 ms for the W08 and PG1 samples respectively. Is important to note as the comparison of the spectroscopic features reported in the Figures 5.3.9 and 5.3.11 put in evidence strong differences between the planar waveguide and the bulk glasses used to fabricate the active film. We can explain this variation with the different composition of the matrixes and the addition of the $HfO_2$ system to the planar waveguide. Zampedri et al. [Zampedri 2004] and Gonçalves et al. [Gonçalves 2004] have, in fact, demonstrated that $Er^{3+}$ spectroscopic properties are strongly affected by the local distortion induced by $Hf^{4+}$ also at low content [Minati 2009]. It is possible that the waveguide

exhibits a more distorted local environment for the $Er^{3+}$ ion in respect to the parent glasses changing drastically the emission band shape in the 1.5 µm region. The Erbium content in the active film result significantly reduced due to the presence of $HfO_2$ and $SiO_2$ on the target for the waveguide fabrication and this fact can contribute to reduce the ion-ion interaction and increase the 1.5 µm lifetime [Gonçalves 2004]. We have also to mention the fact that RF-sputtering process allow to strongly reduce the presence of defects characteristic of the parent glass.

# Bibliography

[Chiasera 2009] Chiasera, A.; Armellini, C.; Bhaktha, S.N.B.; Chiappini, A.; Jestin, Y.; Ferrari, M.; Moser, E.; Coppa, A.; Foglietti, V.; Huy, P.T.; Tran Ngoc, K.; Nunzi Conti, G.; Pelli, S.; Righini, G.C.; Speranza, G. "$Er^{3+}/Yb^{3+}$-activated silica-hafnia planar waveguides for photonics fabricated by rf-sputtering", Journal of Non-Crystalline Solids, 355 (2009), pp. 1176-1179

[Chiasera 2013] Chiasera, A.; Macchi, C.; Mariazzi, S.; Valligatla, S.; Lunelli, L.; Pederzolli, C.; D.N. Rao, D.N.; Somoza, A.; Brusa, R.S.; Ferrari, M. "$CO_2$ laser irradiation of $GeO_2$ planar waveguide fabricated by rf-sputtering", Optical Materials Express, 3 (2013), pp. 1561-1570

[Gonçalves 2002] Gonçalves, R.R.; Carturan, G.; Zampedri, L.; Ferrari. M.; Montagna, M.; Chiasera, A.; Righini, G.C.; Pelli, S.; Ribeiro, S.J.L.; Messaddeq,Y. "Sol-gel Er-doped $SiO_2$-$HfO_2$ planar waveguides: a viable system for 1.5 µm application", Appl. Phys. Lett., 81 (2002), pp. 28-30

[Goncalves 2004] Goncalves, R.R.; Carturan, G.; Montagna, M.; Ferrari, M.; Zampedri, L.; Pelli, S.; Righini, G.C.; Ribeiro, S.J.L.; Messaddeq,Y. "Erbium-activated $HfO_2$-based waveguides for photonics", Opt. Mat., 25 (2004), pp. 131-139

[Hehlen 1997] Hehlen, M.P.; Cockroft, N.J.; Gosnell, T.R. "Spectroscopic properties of $Er^{3+}$-doped and $Yb^{3+}$-doped soda-lime silicate and aluminosilicate glasses", Rev. B, 59 (1997), pp. 9302-9318

[Minati 2009] Minati, L.; Speranza, G.; Micheli, V.; Ferrari, M.; Jestin, Y. "X-ray photoelectron spectroscopy of $Er^{3+}$-activated $SiO_2$–$HfO_2$ glass-ceramic waveguides", Journal of Physics D: Applied Physics, 42 (2009) pp. 0154081-0154085

[Orignac 1999] Orignac, X.; Barbier, D.; Du, X. M.; Almeida, R.M.; McCarthy, O.; Yeatman, E. "Sol-gel silica/titania-on-silicon Er/Yb-doped waveguides for optical amplification at 1.5 µm," Opt. Mater., 12 (1999), pp. 1-18

[Smith 1995] Smith, D.L. "Thin-Film Deposition: Principles Practice", McGrawHill, (1995)

[Tosello 2001] Tosello, C.; Rossi, F.; Ronchin, S.; Rolli, R.; Righini, G.C.; Pozzi, F.; Pelli, S.; Fossi, M.; Moser, E.; Montagna, M.; Ferrari, M.; Duverger, C.; Chiappini, A.; De Bernardi, C. "Erbium-activated silica-titania planar waveguides on silica-on-silicon substrates prepared by rf sputtering", Journal of Non-Crystalline Solids 284, (2001), pp. 230-236

[Valligatla 2012] Valligatla, S.; Chiasera, A.; Varas, S.; Bazzanella, N.; Rao, D.N.; Righini, G.C.; Ferrari, M. "High quality factor 1-D $Er^{3+}$-activated dielectric microcavity fabricated by RF-sputtering", Optics Express 20, (2012), pp. 21214-21222

[Waite 2007] Waite, M.M.; Ismat Shah, S.; Glocker, D.A. "Sputtering Sources" Chapter 15 from "50 Years of Vacuum Coating Technology and the growth of the Society of Vacuum Coaters", Donald M. Mattox and Vivienne Harwood Mattox, eds., Society of Vacuum Coaters, (2007)

[Wasa 1992] Wasa, K.; Hayakawa, S. "Handbook of sputter deposition technology", Noyes, New Jersey, (1992), pp. 81

[Zampedri 2001] Zampedri, L.; Tosello, C.; Rossi, F.; Ronchin, S.; Rolli, R.; Montagna, M.; Chiasera, A.; Righini, G.C.; Pelli, S.; Monteil, A.; Chaussedent, S.; Bernard, C.; Duverger, C.; Ferrari, M.; Armellini, C. "Erbium-activated monolithic silica xerogels and silica-titania planar waveguides: optical and spectroscopic characterization", Proceedings of SPIE 4282, (2001), pp. 200-209

[Zampedri 2004] Zampedri, L.; Righini, G.C.; Portales, H.; Pelli, S.; Nunzi Conti, G.; Montagna, M.; Mattarelli, M.; Goncalves, R.R.; Ferrari, M.; Chiasera, A.; Bouazaoui, M.; Armellini, C. "Sol-gel-derived Er-activated $SiO_2$-$HfO_2$ planar waveguides for 1.5 μm application", Journal of Non-Crystalline Solids, 345&346 (2004), pp. 580-584

[Yeatman 1999] Yeatman, E.M.; Ahmad, M.M.; McCarthy, O.; Vannucci, A.; Gastaldo, P.; Barbier, D.; Mongardien, D.; Moronvalle, C. "Optical gain in $Er^{3+}$-

doped $SiO_2$-$TiO_2$ waveguides fabricated by the sol-gel technique", Opt. Comm. 164 (1999), pp. 19-25

## 6. Scanning Electron Microscopy

The history of electron microscopy started with the development of electron optics. The first "scanning microscope" was built by Knoll in 1935. In 1938, theoretical explanation of principles underlying the scanning microscope was performed by von Ardenne. The first and real description and development of SEM was accomplished by Zworykin in 1942. Zworykin showed that the secondary electrons provided topographic contrast by biasing the collector positively relative to the specimen [Bogner 2007, Goldstein 2003].

SEM allows providing information on crystalline structure, chemical composition, topography of the surface and electrical behavior. In comparison with optical microscopy, SEM has the following advantages: (i) SEM benefits from a large depth of field of the specimen surface apart from the surface roughness; (ii) High magnification can be attained up to 1 000 000x; (iii) besides surface topography, by SEM can be obtained information on crystal structure, electrical and chemical properties [Bogner 2007].

The electron beam interacts with the specimen from an electron gun, which rapidly scans the specimen surface. After this interaction of a beam with the specimen produces secondary, backscattered and Auger electrons, x-rays and light from the specimen surface, collected by different detectors, which generates electronic signals. These signal are collected in the manner of image on a cathode ray tube (CRT). The intensity of these secondary electrons depends upon the shape and the chemical composition of the specimen.
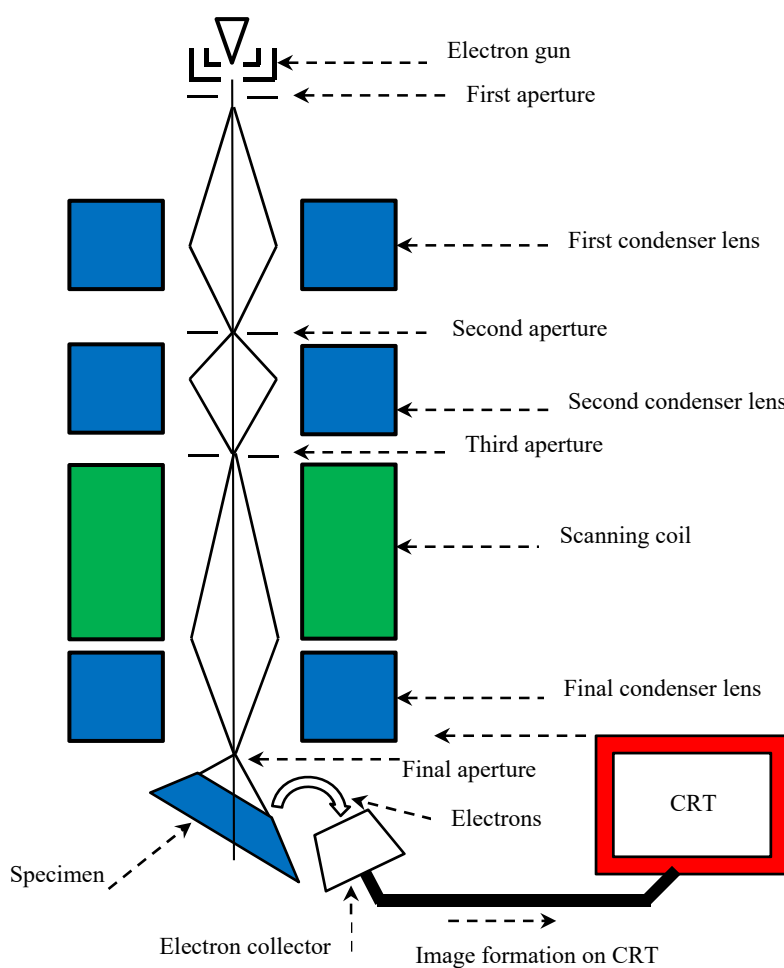
**Figure 6.1.** Ray diagram of a Scanning Electron Microscope.

Sol-gel prepared samples were investigated by Scanning electron microscopy (SEM) using FEI Quanta 200 SEM apparatus (Fig.6.2 (a, b, c, d)).
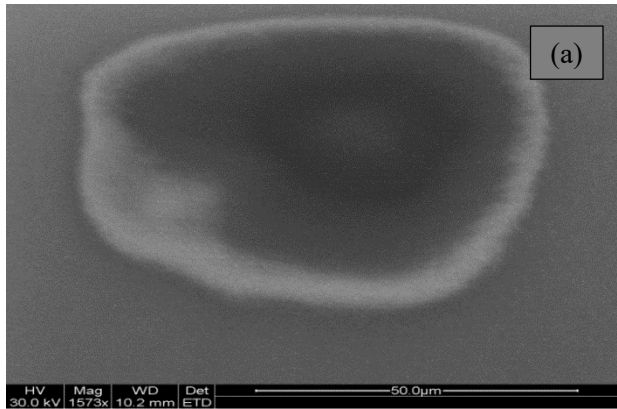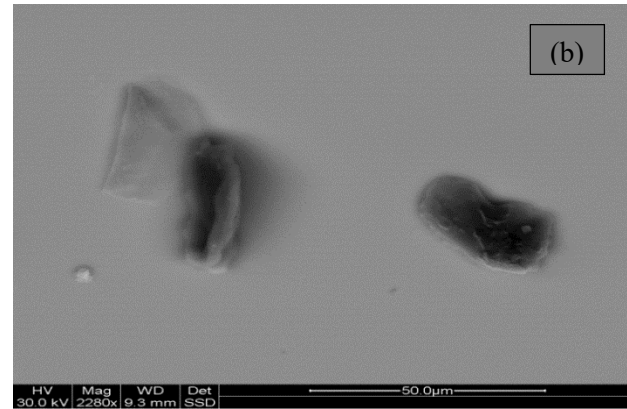
**Figure 6.2.** SEM microphotography of W4.



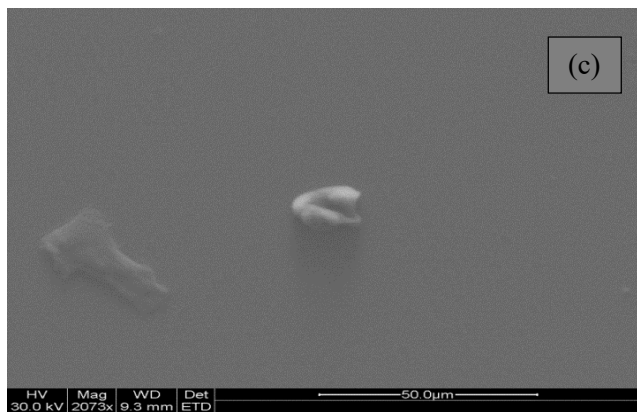**Figure 6.2.** SEM microphotography of W1.
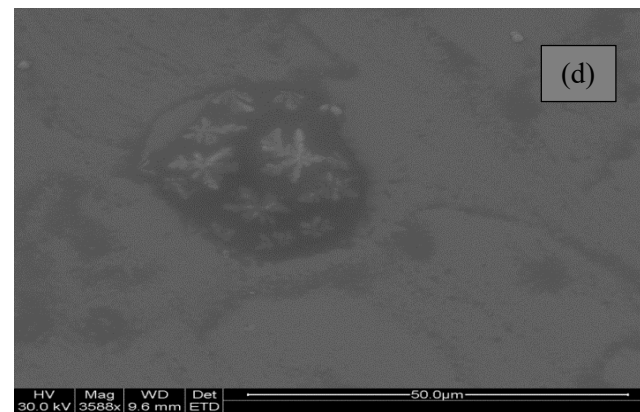


**Figure 6.2.** SEM microphotography of W3.



**Figure 6.2.** SEM microphotography of sputtered W05 waveguide on Silicon.

The microphotographs of sol-gel prepared and sputtered waveguides reveals some random defects. In case of sol-gel prepared waveguides the possibility to observe some macro-inhomogeneities in the structure are related to the fabrication process, which is multistep and requires strict control of all the steps of the production process in order to minimize the voids, contaminants introduced into the waveguide during the film formation procedure. Usually, the waveguides prepared by RF sputtering technique have much more less defects.

## 6.1 Atomic Force Microscopy

Atomic Force Microscopy is a robust and versatile research technique that permits to investigate the morphology and the local properties of surface with high spatial resolution. This technique was invented by Binning and coworkers in 1986 [Binnig 1986]. AFM allows the analysis of a surface and of its local properties by using special probes made by an elastic cantilever with a sharp tip on the end. The tail piece of such tips is about 10 nm. Usually the tip is placed close to the surface with working is 0.1-10 nm [Mironov 2004]. AFM measurements based on the atomic interaction force between the tip and the surface. This force coming from the surface and results in bending of the cantilever. When the tip is moved it will follow the surface contours. A laser beam is located at the end of the cantilever to measure its deviation by photoelectric sensors.  The distance between the surface and the tips is controlled by piezoelectric tubes, as well as the lateral scan. The tip-surface interactive force is possible to determine by measuring the cantilever deflection. The cantilevers deflection is detected and converted into an electronic signal that is utilized to reconstruct an image of the surface [Mironov 2004, Binning 1986].
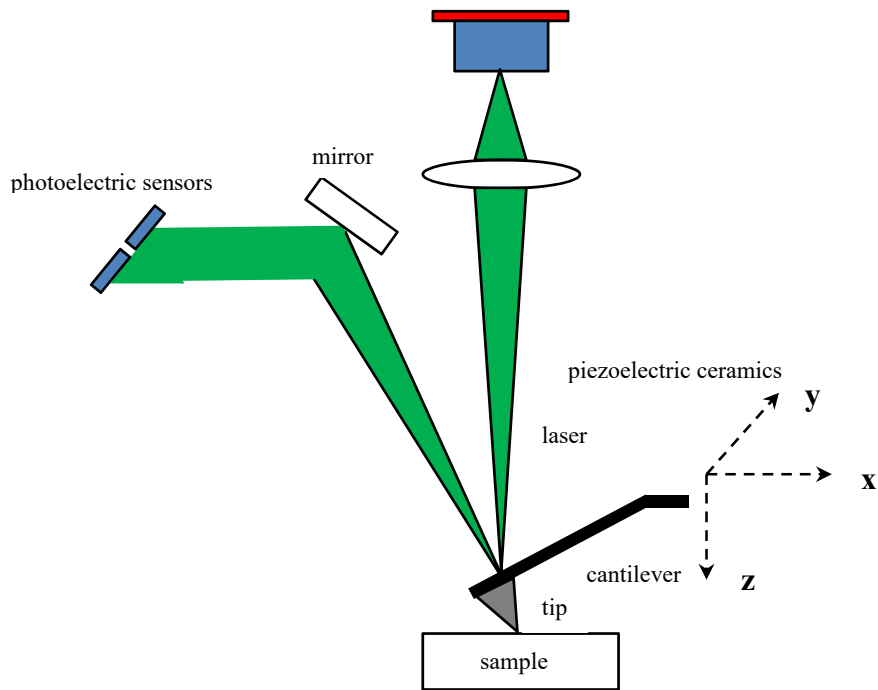
**Figure 6.1.1.** General principle of AFM.

The morphological characterization of sol-gel and RF-sputtered planar waveguides has been performed.

The AFM images were acquired with a Solver Px Scanning Probe Microscope from NT-MDT. AFM data were acquired in semi-contact mode with a Silicon tip (~5.5 N/m, ~120 KHz) with a nominal radius of less than 10 nm. Analyses were performed in the "center" of each sample on different scanning areas, 10x10 μm².

Average (Sa) and root mean square (Sq) roughness were estimated for each scanned area. Related formulas are given below:

Sa – average roughness, ISO 4287/1 (nm):

$$S_a = \frac{1}{N_x N_y} \sum_{i=1}^{N_x} \sum_{j=1}^{N_y} |z| \qquad (17)$$

Sq – Root mean square roughness, ISO 4287/1 (nm):

$$S_q = \sqrt{\frac{1}{N_x N_y} \sum_{i=1}^{N_x} \sum_{j=1}^{N_y} (z)^2} \qquad (18)$$

**Table 6.1.2.** Experimental conditions.

| Instrument | AFM  (NT-MDT Unisolver) |
|---|---|
| Probe | "GOLDEN"  Silicon  Probes/rectangular cantilever NSG01 |
| Force Constant | ~5.5 N/m |
| Resonant Frequency | 120.9 and 122.95 KHz |
| Analysed Area | 5x5, 10x10 μm² |
| Scan Mode | semi contact mode |

The waveguides have been investigated by the relative statistical analysis of the 5x5 and 10x10 μm² scanned areas. In some cases the cross section, on selected features, or a 3D image are reported as well (Figure 6.1.3).

(a)



(b)
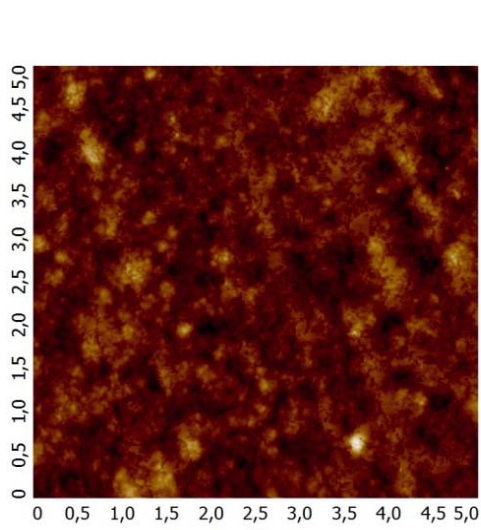


**Figure 6.1.3.** AFM of phosphate based waveguide on Silicon, fabricated by sputtering.

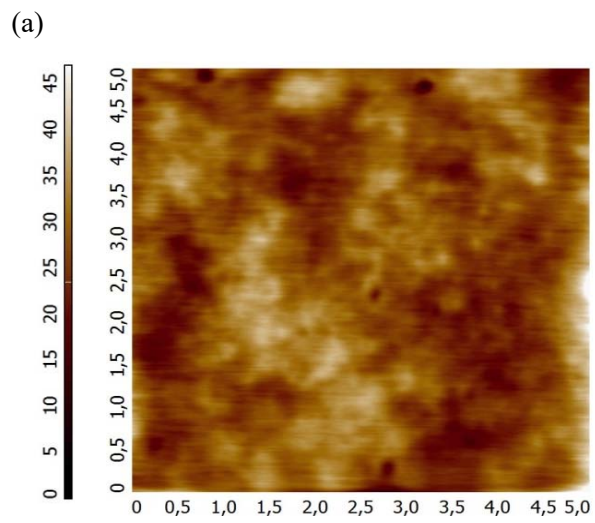Sq     7.0 nm
Sa     4.6 nm

**Figure 6.1.3.** AFM of Phosphorous (4 mol. %) codoped sol-gel silica hafnia waveguide.

Sq     3.3 nm
Sa     2.6 nm

(c)



(d)
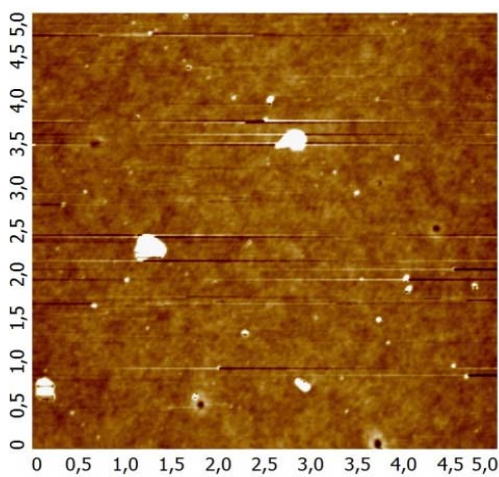


**Figure 6.1.3.** AFM of W2 sol-gel waveguide.

Sq     0.5 nm
Sa     0.2 nm
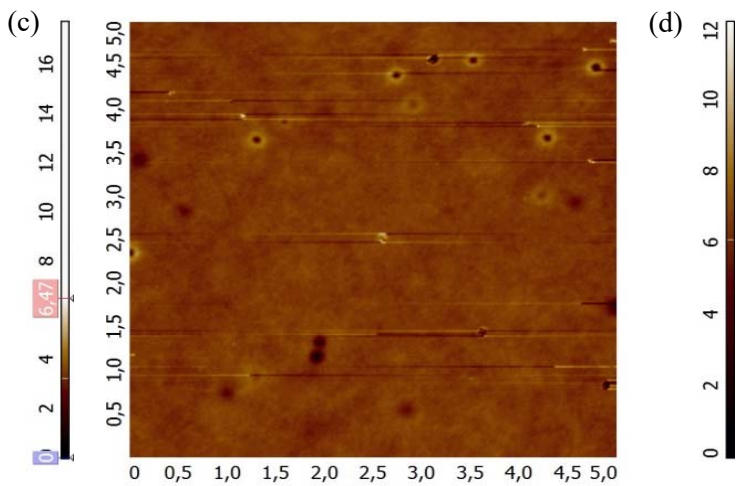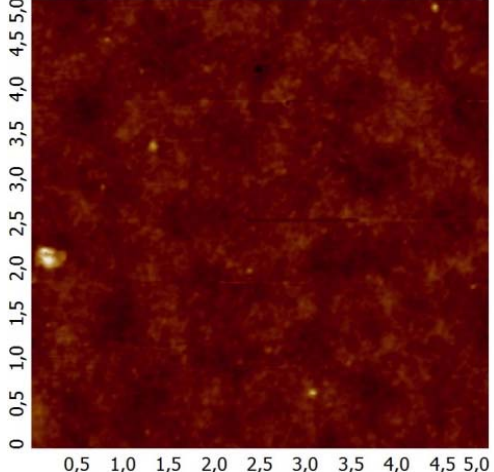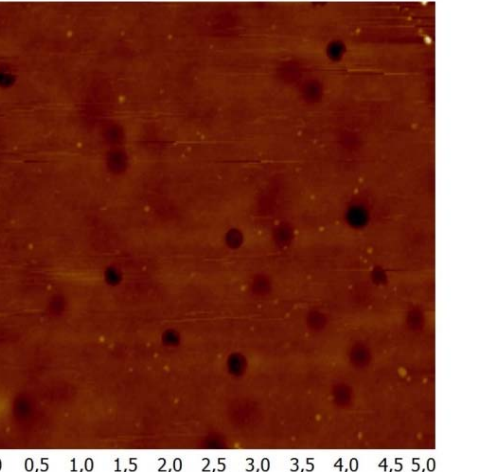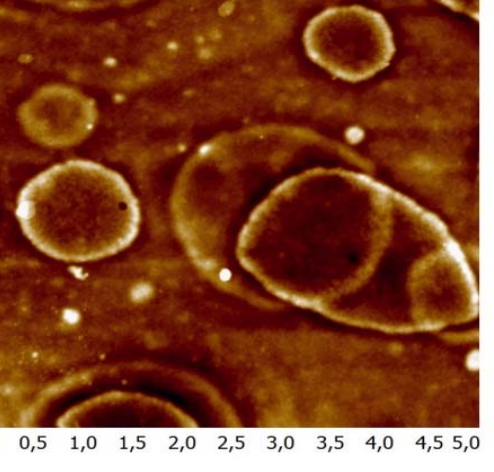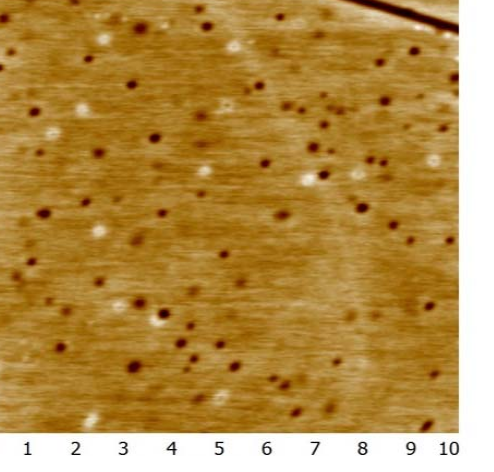
**Figure 6.1.3.** AFM of S08 (silica hafnia without Phosphorous, 50 layers) sol-gel waveguide.

Sq     0.9 nm
Sa     0.5 nm

143

(e)

**Figure 6.1.3.** AFM of S sol-gel waveguide.

Sq     1.2 nm
Sa     0.9 nm



(f)

**Figure 6.1.3.** AFM of W1 waveguide prepared by sol-gel route.

Sq     1.0 nm
Sa     0.5 nm



(h)

**Figure 6.1.3.** AFM of Phosphorous doped $((CH_4CH_9O)_3PO$ 10 mol. %) sol-gel waveguide.

Sq     2.6 nm
Sa     1.8 nm



(i)

**Figure 6.1.3.** AFM of S10 (silica safnia without Phosphorous 30 layers) sol-gel waveguide.

Sq     0.8 nm
Sa     0.5 nm

**Figure 6.1.3.** AFM of S09 (silica hafnia without Phosphorous 20 layers) sol-gel waveguide.
Sq      0.8 nm
Sa      0.6 nm

**Figure 6.1.3.** AFM of W08 waveguide prepared by RF-sputtering technique.
Sq      4.2 nm
Sa      3.3 nm
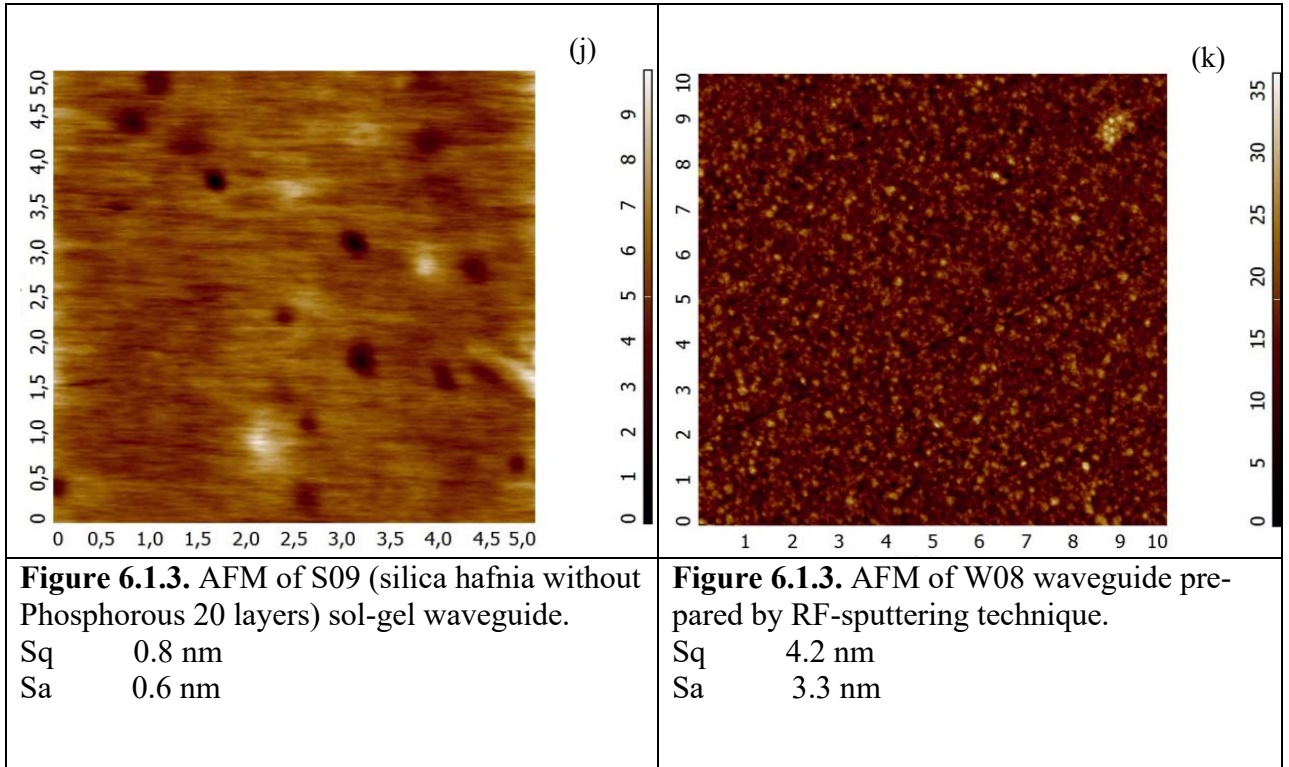
We report AFM images, the relative statistical analysis a 3D image on selected features of the 5x5 and 10x10 $\mu m^2$ scanned areas. Since the samples are supposed to be uniform, a single point for each sample was analysed. In case of sol-gel derived samples the morphology is different and an average roughness is depending on the chemical synthesis protocol and fabrication procedure is about 0.2-4.6 nm.

In conclusion we can tell that the average roughness of the films is  reasonably low, also for sol-gel derived waveguides. So, the losses are mainly due to microscopic defects.

# Bibliography

[Binning 1986] Binning, G.; Quate, F.; Gerber, Ch. "Atomic Force Microscope", Phys. Rev. Lett. 56 (1986), pp. 930-933

[Bogner 2006] Bogner, A.; Jouneau, P.H.; Thollet, G.; Basset, D.; Gauthier, C. "A history of scanning electron microscopy developments: towards "wet-STEM" imaging", Micron., 38 (2006), pp. 390-401

[Goldstein 2003] Goldstein, J.; Newbury, D.E.; Joy, D.C.; Lyman, C.E.; Echlin, P.; Lifshin, E.; Sawyer, L.; Michael, J.R. "Scanning Electron Microscopy and X-ray Microanalysis", Springer US, Third Edition (2003), pp.689

[Mironov 2004] Mironov, V.L. "The Fundamentals of the Scanning Probe Microscopy", Russian Academy of Sciences, Institute of Physics of Microstructures, (2004)

## 7. Dispersion in $SiO_2$-$HfO_2$-$P_2O_5$ planar waveguides

If one wishes to understand the origin of dielectric response function, or needs to deal with the dielectric properties of heterogeneous materials such as glasses, i.e. as in the present case, then the microscopic aspect cannot be ignored [Aspnes1982]. In particular, the refractive index and its dispersion are crucial for all the photonic application [Huang 1978, Karpienko 2014, Mito 1997].

From an experimental point of view the dispersion curve can be obtained by reflectance and transmittance measurement considering an electromagnetic field propagating in a multilayered dielectric system [Tan 1998]. This kind of measurement and analysis still remain a non-trivial task and the situation is much more complicated in the case of dip-coated waveguides due to the fact that the active film is deposited on both the side of the substrate [Belka2014].

From a general point of view the problem concerns electromagnetic planar multilayered media and the inverse transmittance problem for normal incidence: determination of the refractive index of an unknown material from a measured transmittance spectrum.

## 7.1 Characterization of the reflectance $R$ and transmittance T of a waveguiding system

The present Section is devoted to the study and characterization of the reflectance $R$ and transmittance $T$ of a system of $N$ contiguous dielectric layers (multilayer), stacked along the $y$ axis (to fix ideas) and having ideal infinite extensions along the $x$ and $z$ transverse directions, when a plane electromagnetic monochromatic wave, representing a light beam of given vacuum wavelength, impinges on it.

The approach is algorithmically oriented, being aimed to find a way to characterize the multilayer optical behavior by means of an easily implementable computer numerical code for arbitrary values of $N$.

Here, only the normal incidence case will be considered, which implies that the TE (Transverse Electric) and TM (Transverse Magnetic) polarizations will coincide.

Each layer is made of a material having a complex refractive index $\hat{n}_s$, Eq.19:

$$\hat{n}_s = n_s + ik_s \qquad (19)$$

where $i$ denotes the imaginary unit, while $s$ is an integer index labeling the different layers ($s = 1, \dots, N$). The imaginary part of the complex refractive index is known as the extinction coefficient and depends on the light absorption properties of a given material. The complex refractive index (along with its real and imaginary parts) depends in general on the (angular) frequency $\omega$ of the monochromatic plane wave, which is related to its vacuum wavelength $\lambda$ by means of Eq. 20:

$$\lambda = \frac{2\pi c_o}{\omega} \qquad (20)$$

where $c_o$ is the vacuum light speed. Also, each layer has a thickness $d_s$ ($s = 1, \dots, N$). The system is completed by considering a semi-infinite non-absorbing leading medium, in front of the multilayer (labeled with $s = 0$), which propagates the impinging incident wave, and a semi-infinite trailing medium after the multilayer (labeled with $s = N + 1$), which propagates the transmitted wave. The first layer with index $s = 1$ starts at the origin $O$ along the $y$ axis, with coordinate $y = 0$. The overall system is schematically depicted in the next Figure 7.1.1.
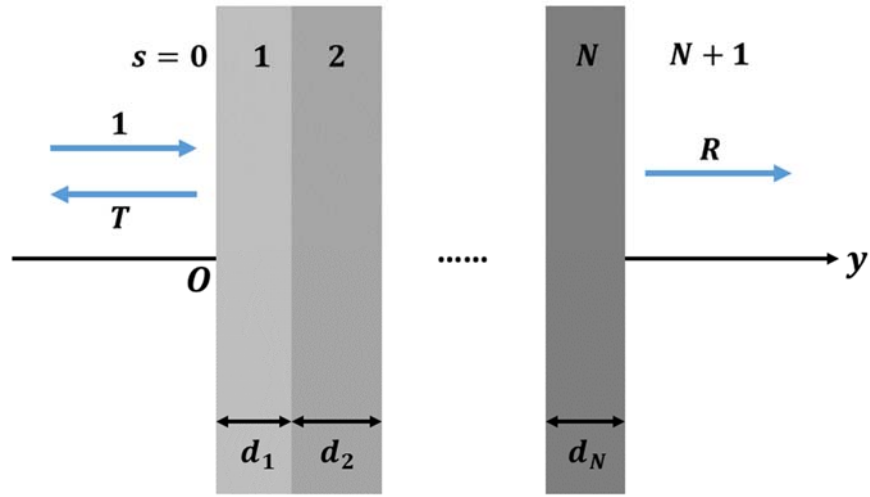
**Figure 7.1.1.** Scheme of the waveguiding system.

In what follows non-magnetic materials with magnetic permeability identically equal to that of vacuum are also assumed throughout, that means: $\mu \equiv \mu_o$ everywhere.

In order to calculate the reflected or transmitted electromagnetic powers normalized to the incident one, which are two ratios named reflectance $R$ and transmittance $T$ of the multilayered system, respectively. One can consider, to start, a simpler system with a single interface between two different media, labeled with indices $s = 1$ to the left and $s = 2$ to the right.

The most general solution is one in which on both of sides, the electromagnetic field is the superposition of right-going $(+)$ and left-going $(-)$ monochromatic plane waves:

$$E_{s,z} = E_s^{(+)}e^{+i\hat{k}_s y} + E_s^{(-)}e^{-i\hat{k}_s y} \qquad (21)$$

$$H_{s,x} = \frac{\hat{k}_s}{\omega\mu_o}\left[E_s^{(+)}e^{+i\hat{k}_s y} - E_s^{(-)}e^{-i\hat{k}_s y}\right] \qquad (22)$$

$(s = 1,2)$ where

$$\hat{k}_s^2 = \left(\frac{\omega}{c_o}\hat{n}_s\right)^2 \qquad (23)$$

The previous relations are consequences of Maxwell's equations, which rule all of the electromagnetic phenomena. Maxwell's equations also dictate that the $\vec{E}$ and $\vec{H}$ field vectors and the propagation direction unit vector in a plane wave are mutually orthogonal and form a right handed frame. This constrain explains why in the above expression for the magnetic $x$ component there is a minus sign before the left-going amplitude (the $H$ field is reversed while the $E$ field is not, to obey the prescription).

Besides that, Maxwell's equations dictates also the boundary conditions in passing through the discontinuous material interface from medium 1 to medium 2: there must be continuity of the tangential components of the electric and magnetic fields across the interface. Because it is at $y = 0$, this condition transforms in a matrix form, as following:

$$\begin{bmatrix} 1 & 1 \\ \hat{k}_1 & -\hat{k}_1 \end{bmatrix} \begin{bmatrix} E_1^{(+)} \\ E_1^{(-)} \end{bmatrix} = \begin{bmatrix} 1 & 1 \\ \hat{k}_2 & -\hat{k}_2 \end{bmatrix} \begin{bmatrix} E_2^{(+)} \\ E_2^{(-)} \end{bmatrix} \qquad (24)$$

By denoting with $D_s$ the 2x2 matrices above, which characterize the left or right material ($s = 1, 2$), after solving for the $s = 1$ amplitudes, the previous relation becomes, Eq. 25:

$$\begin{bmatrix} E_1^{(+)} \\ E_1^{(-)} \end{bmatrix} = (D_1)^{-1} D_2 \begin{bmatrix} E_2^{(+)} \\ E_2^{(-)} \end{bmatrix} \qquad (25)$$

where the $-1$ exponent denotes the matrix inverse.

A step further toward generalization consists in considering a single layer with two interfaces, one at $y = 0$ and the other at $y = L$, with three different media involved, labeled with index $s = 1, 2, 3$ from left to right, respectively. In this case it is possible to write down separately the transitions at the interface 0 to 1 and 1 to 2 which are of the type just seen, but a further relation is needed to connect the

field amplitudes at the interfaces located at $y = 0$ and $y = L$ inside medium s=1. This situation is depicted in Figure 7.1.2, in which it is assumed that for the transmitted waves (inside media s=1,2) the exponential phase reference is taken at y = L, while for the incoming wave (inside media s=0) this reference is taken at y=0.
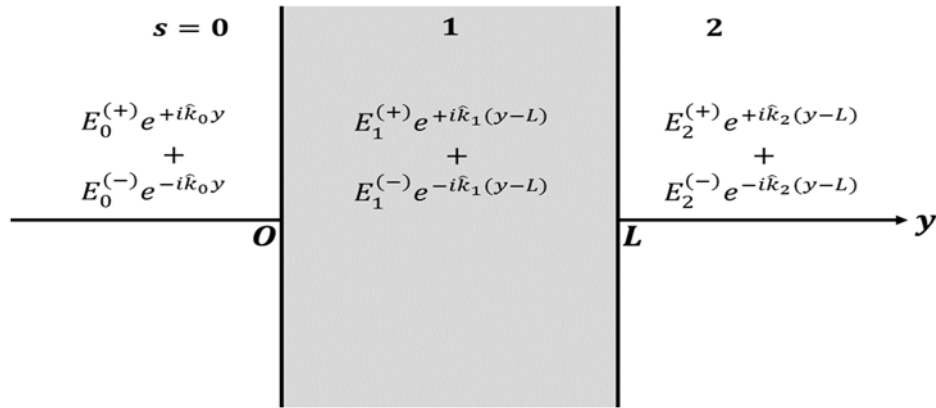


**Figure 7.1. 2** Transitions at the interfaces in the waveguiding layer.

By putting $y = 0$ and $y = L$ for the $s = 1$ medium, it is easily seen that the relation between the left and right layer interface amplitudes is:

$$\begin{bmatrix} E_1^{(+)} \\ E_1^{(-)} \end{bmatrix}_{at\ O} = P_1 \begin{bmatrix} E_1^{(+)} \\ E_1^{(-)} \end{bmatrix}_{at\ L} = \begin{bmatrix} e^{-i\hat{k}_1 L} & 0 \\ 0 & e^{+i\hat{k}_1 L} \end{bmatrix} \begin{bmatrix} E_1^{(+)} \\ E_1^{(-)} \end{bmatrix}_{at\ L} \qquad (26)$$

i.e., by means of a propagation matrix $P_1$ which is diagonal and depends on the thickness $L$ of the layer.

By composing this propagation with the transitions 0 to 1 and 1 to 2, one then has finally the linear relation between the incoming and exiting amplitudes, Eq. 27:

$$\begin{bmatrix} E_0^{(+)} \\ E_0^{(-)} \end{bmatrix} = (D_0)^{-1} D_1 P_1 (D_1)^{-1} D_2 \begin{bmatrix} E_2^{(+)} \\ E_2^{(-)} \end{bmatrix} \qquad (27)$$

This pattern is easily generalized to the case of $N$ layers:

$$\begin{bmatrix} E_0^{(+)} \\ E_0^{(-)} \end{bmatrix} = (D_0)^{-1}D_1P_1(D_1)^{-1}D_2P_2(D_2)^{-1}\cdots D_NP_N(D_N)^{-1}D_{N+1}\begin{bmatrix} E_{N+1}^{(+)} \\ E_{N+1}^{(-)} \end{bmatrix} \quad (28)$$

Hence the approach described gives an algorithm which is easily implementable as a computer numerical code, allowing the calculation of the overall matrix relation of the field amplitudes at the front and rear sides (with respect to the impinging beam propagation direction) of an arbitrary number of layers.

This overall matrix is expressed as a product sequence of 2x2 matrices. In such a sequence there are subsequences characterizing the single material slab through its complex refractive index and thickness: $D_kP_k(D_k)^{-1}$, for $k = 1, \ldots, N$.

The padding matrices $(D_0)^{-1}$ and $D_{N+1}$ describe instead of the initial and final semi-infinite media and do not involve any thicknesses.

The order of the sequence is important, because matrix product does not commute, although it still does remain associative. Once the overall matrix is known, it allows the calculation of the reflectance $R$ and transmittance $T$ of the multilayer system. In fact, using the definition of the Poynting vector for the incident, reflected and transmitted powers per unit area, it follows that:

$$\mathcal{P}_{inc.} = \frac{\left|E_0^{(+)}\right|^2}{2Z_{vac.}}\mathcal{R}e\{\hat{n}_0\} \quad (29)$$

$$\mathcal{P}_{refl.} = \frac{\left|E_0^{(-)}\right|^2}{2Z_{vac.}}\mathcal{R}e\{\hat{n}_0\} \quad (30)$$

$$\mathcal{P}_{trans.} = \frac{\left|E_{N+1}^{(+)}\right|^2}{2Z_{vac.}}\mathcal{R}e\{\hat{n}_{N+1}\} \quad (31)$$

where $\mathcal{R}e\{\cdots\}$ denotes the real part of a complex quantity, while $Z_{vac.}$ is the free space or vacuum impedance, a constant characteristic value of about 377 Ω. As has

been previously pointed out, the $s = 0$ medium is always assumed non-absorptive and thus $\hat{n}_0$ effectively is a real quantity (usually with a value of unity). For what concerns the transmitted power, the expression reported refers to the power flux just after the multilayer (or the beginning of the semi-infinite trailing medium), because if this medium is absorptive (i.e., $\hat{n}_{N+1}$ effectively a complex quantity) there will be an exponential decay of the power flux depending on the path length inside it, measured from its beginning after the multilayer. The vertical bars in the above expression denote modulus of complex quantities. By definition, one has that (for normal incidence):

$$R = \frac{\left|E_0^{(-)}\right|^2}{\left|E_0^{(+)}\right|^2} \tag{32}$$

$$T = \frac{\left|E_{N+1}^{(+)}\right|^2}{\left|E_0^{(+)}\right|^2} \mathcal{Re}\left\{\frac{\hat{n}_{N+1}}{\hat{n}_0}\right\} \tag{33}$$

The amplitude ratios in the expressions above are easily obtained if the overall matrix, let us call it S, has been calculated for a given multilayer. In fact, from the linear relation:

$$\begin{bmatrix} E_0^{(+)} \\ E_0^{(-)} \end{bmatrix} = S \begin{bmatrix} E_{N+1}^{(+)} \\ E_{N+1}^{(-)} \end{bmatrix} = \begin{bmatrix} S_{11} & S_{12} \\ S_{21} & S_{22} \end{bmatrix} \begin{bmatrix} E_{N+1}^{(+)} \\ E_{N+1}^{(-)} \end{bmatrix} \tag{34}$$

Suppose that $E_{N+1}^{(-)} = 0$, one gets:

$$\frac{E_0^{(-)}}{E_0^{(+)}} = \frac{S_{21}}{S_{11}} \tag{35}$$

and

$$\frac{E_{N+1}^{(+)}}{E_0^{(+)}} = \frac{1}{S_{11}} \qquad (36)$$

However involved is the multilayered structure, it is only a matter of constructing the matrix $S$ according to the previous formula to be able to calculate its transmittance and reflectance. Such a task can be readily obtained, after specification of the optical characteristics and thicknesses of the various constituent layers, by means of a computer code implementing the matrix products and for a whole frequency range, thus producing a spectral response of the multilayer.

We do not stress here on the specific analytic closed form which could take the elements of the matrix $S$, particularly for periodic multilayered structures (as would be the case of a given pattern of material slabs repeated many times along the beam propagation direction). We are mainly interested in the general numerical calculability of such elements by means of a computer code: a task which will be used in the application described in the next part.

## 7.2. Optical transmission calculations of the waveguiding system

The algorithm just described before solves the direct problem of calculating the optical transmittance behavior of a given multilayered structure. However, the same algorithm can also be used for the inverse problem. That is, the one of determining the refractive index and thickness of an unknown material layer - inserted inside a multilayer built from a sequence of slabs of known properties- from an experimentally measured transmittance spectrum of such a structure over a chosen wavelength range.

The spectrum, obtained instrumentally with a given wavelength sampling step, usually makes available a lot of transmittance data at various wavelengths which are in excess with respect to the number of parameters to be determined. Such a data set is thus suitably amenable to a least squares regression analysis which, however, will have to be nonlinear because transmittance does depend from the parameters in a nonlinear fashion.

To fix ideas, in the present work a tri-layer system has been considered, like the one which is schematically represented in Figure 7.2.1.
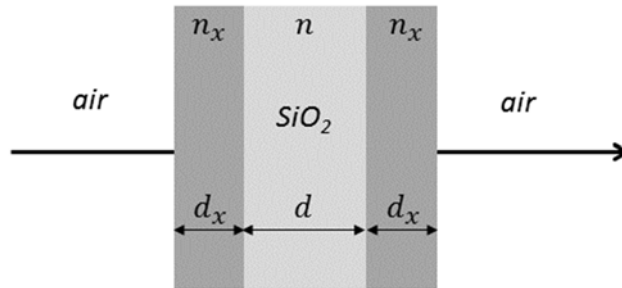


**Figure 7.2.1** Multilayered waveguiding structure.

Where a silica ($SiO_2$) substrate with a thickness $d = 1$ mm is sandwiched between two equal layers of a transparent material of unknown refractive index $n_x$ and thickness $d_x$.

It is assumed that the refractive index dispersion of the Silica substrate is described by the following Sellmeier formula, Eq. 37:

$$n(\lambda) = \sqrt{1 + \frac{A_1\lambda^2}{\lambda^2 - B_1^2} + \frac{A_2\lambda^2}{\lambda^2 - B_2^2} + \frac{A_3\lambda^2}{\lambda^2 - B_3^2}} \qquad (37)$$

where the parameters $A_i$ and $B_i$ ($i = 1, 2, 3$) values (for wavelengths expressed in micron, $\mu m$) are taken from the web site RefractiveIndex.INFO at:
http://refractiveindex.info/?shelf=main&book=SiO2&page=Malitson
and then:

$$A_1 = 0.6961663$$
$$A_2 = 0.4079426$$
$$A_3 = 0.8974794$$
$$B_1 = 0.0684043 \ \mu m^2$$
$$B_2 = 0.1162414 \ \mu m^2$$
$$B_3 = 9.896161 \ \mu m^2$$

For the unknown material a similar Sellmeier equation has been considered:

$$n_x(\lambda) = \sqrt{1 + \frac{H_1\lambda^2}{\lambda^2 - K_1^2} + \frac{H_2\lambda^2}{\lambda^2 - K_2^2} + \frac{H_3\lambda^2}{\lambda^2 - K_3^2}} \qquad (38)$$

but with the six parameters $H_i, K_i$ ($i = 1, 2, 3$) to be determined, along with the thickness $d_x$, by means of the previously mentioned nonlinear least squares fit, for a total of seven unknown parameters to be eventually calculated.

In other words, there is a quantitative analytical model, represented formally by the transmittances numerically calculated by the algorithm described in Part 7.1, at a given wavelength $\lambda_\ell$ and as a nonlinear function of the seven parameters $d_x, H_i, K_i$ ($i = 1, 2, 3$):

$$T_{NUM}(d_x, H_1, H_2, H_3, K_1, K_2, K_3 \mid \lambda_\ell) \qquad (39)$$

and which has to be tested for acceptance, after comparison against

$$T_{MEAS}(\lambda_\ell) \qquad (40)$$

This is a set of experimentally measured transmittances at corresponding wavelengths. Here $\ell$ is in fact the index scanning the set of measured transmittance data in correspondence of the various vacuum wavelengths.

In the present case: $\ell = 0, \dots, N$, with $N = 1400$, for the wavelength range $400 \div 1800$ nm, sampled with 1 nm steps. $N$ has not to be confused here with the number of layers in the multilayer as it was in indicated in Part 7.1. Here the layer number is particularized to a value of 3.

The basis of least squares analysis is the minimization of the following expression:

$$\sum_{\ell=0}^{N} \left[ \frac{T_{NUM}(d_x, H_1, H_2, H_3, K_1, K_2, K_3 \mid \lambda_\ell) - T_{MEAS}(\lambda_\ell)}{\sigma_\ell} \right]^2 \qquad (41)$$

representing the squared norm of the residuals as the components of a vector in the linear space $R^{N+1}$ (squared norm of the total residual), normalized by the standard deviations $\sigma_\ell$ of the various measured values.

That is to say, that the calculations are aimed to determine the parameter values $d_x, H_1, H_2, H_3, K_1, K_2, K_3$ for which such expression has a minimum. These will then be the "true" values which characterize the unknown layer.

To this end, one has to introduce the vector valued function $\vec{F}$ with $N + 1$ components, Eq. 42:

$$\vec{F}(d_x, H_1, H_2, H_3, K_1, K_2, K_3) = \begin{bmatrix} f_0(d_x, H_1, H_2, H_3, K_1, K_2, K_3) \\ \vdots \\ f_\ell(d_x, H_1, H_2, H_3, K_1, K_2, K_3) \\ \vdots \\ f_N(d_x, H_1, H_2, H_3, K_1, K_2, K_3) \end{bmatrix} \qquad (42)$$

where

$$f_\ell(d_x, H_1, H_2, H_3, K_1, K_2, K_3) \equiv \frac{T_{NUM}(d_x, H_1, H_2, H_3, K_1, K_2, K_3 | \lambda_\ell) - T_{MEAS}(\lambda_\ell)}{\sigma_\ell} \qquad (43)$$

for $\ell = 1, \dots, N$. To simplify the notation, it is convenient, from now on, to collectively call the parameters $d_x, H_1, H_2, H_3, K_1, K_2, K_3$ as a single vector argument (with seven components) $\vec{p}$ (and addressing each one of them by a subscript $m$: $p_m$ with $m = 0, \dots, 6$).

Then, one has to consider the Jacobian matrix of the vector valued function $\vec{F}$ with respect to these parameters:

$$J(\vec{p}) = \left[ \frac{\partial f_\ell(\vec{p})}{\partial p_m} \right] \qquad (44)$$

157

Where $\ell = 0, \ldots, N$ is row index and $m = 0, \ldots, 6$ a column index (i.e., the Jacobian is a $(N+1) \times 7$ matrix). The minimization procedure of the squared norm of the residuals has necessarily to be an iterative one due to the nonlinear dependence of $T_{MEAS}$ from the parameters $\vec{p}$ and as shown in the literature on optimization theory, for the calculation of the minimizing parameters, the successive corrections $\Delta\vec{p}$ of an initial guess $\vec{p}^0$ are found by solving the 7x7 linear system:

$$J(\vec{p}^k)^t J(\vec{p}^k)\Delta\vec{p} = -J(\vec{p}^k)^t \vec{F}(\vec{p}^k) \qquad (45)$$

$$\vec{p}^{k+1} = \vec{p}^k + \Delta\vec{p} \qquad (46)$$

In other words, there is a recursive procedure to follow for the determination of the parameter values.

For the present work the following observations are to be kept in mind:

(i) The standard deviations $\sigma_\ell$ are not known a priori and are put equal to 1 in the present application of the least squares regression fit. The error in the measurements is calculated a posteriori after the parameters $\vec{p}$ have been calculated at the end of the recursive procedure; (ii) The evaluation of the Jacobian matrix elements, requiring derivatives with respect to the parameters $\vec{p}$, has been made by means of finite differences after some small increments are added to the actual values of $\vec{p}$ themselves (this a possible source of interference with the convergence during the recursive calculation of the corrections $\Delta\vec{p}$s); (iii) The initial guesses for the parameters $\vec{p}$, relatively to $m = 1$ to 6, are chosen as a mixing of the corresponding ones for Silica ($SiO_2$), and previously reported, and those for Hafnia ($HfO_2$), which have instead of the following values:

$$A_1 = 1.9558$$
$$A_2 = 1.345$$
$$A_3 = 10.41$$

$$B_1 = 0.15494 \ \mu m^2$$

$$B_2 = 0.0634 \ \mu m^2$$

$$B_3 = 27.12 \ \mu m^2$$

and which have been taken from the web site RefractiveIndex.INFO at:

http://refractiveindex.info/?shelf=main&book=HfO2&page=Wood

The coefficients in the linear combination add up to 1, with a discretely varying percentage of each of the materials (if $\alpha$ is the percentage of Silica, the $(1 - \alpha)$ is the percentage of Hafnia). Also, a given thicknesses range is spanned discretely to give the initial guesses for the parameter $p_0$.

The measured transmittance data obtained with Varian Cary 5000 UV-Vis-NIR Spectrophotometer for a physical realization of the three-layer system previously described and which served for the least squares regression analysis which is reported in the following graph (data are sampled with increments of 1 nm, for a total of 1400 data points).
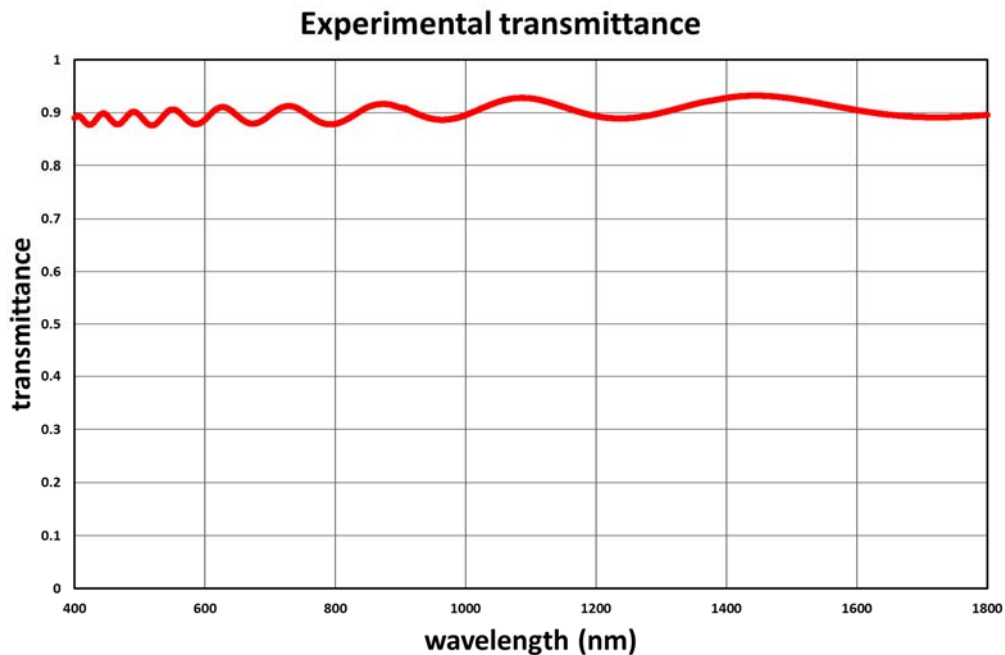


**Figure 7.2.2.** Experimentally obtained transmittance of the waveguiding system.

There is a smoothing effect of the measurement apparatus which can also be interpreted as noise in the data, because the curve is not jagged as expected for a

substrate thickness of 1 mm. The measure is non ideal also because there is some not expected loss in the transmittance.

The least squares analysis above described and applied to the mentioned three-layer system, does not give a neat global minimum associated with a specific thickness. Probably such a nonlinear problem may have a large number of local minimum solutions and finding the global minimum can be difficult. Otherwise, if there are several local minimum solutions with acceptable data fits, then it may be difficult to select a single "best" solution. A parameter measuring the goodness of a fit is the norm of the total residual after the completion of the recursive procedure (which is stopped by setting a tolerance below which the iterative corrective adjustments of the parameters $\vec{p}$ are interrupted). De facto, it can be considered the common value of the a posteriori normal standard deviations of the various experimental transmittance values (remembering that it has been previously pointed out that the prior independent Gaussian normal standard deviations $\sigma_\ell$ of the experimental data for $\ell = 1, \dots, N$ are not known and assumed equal to 1). In the Table 7.2.3 below are reported:

**Table 7.2.3.** Gaussian normal standard deviations of the experimental data.

| Total residual | 0.06159 | 0.06553 | 0.07047 |
|---|---|---|---|
| Thickness (nm) | 1460 | 1760 | 2440 |
| $H_1$ | 0.75990 | 0.79148 | 0.92957 |
| $H_2$ | 0.39917 | 0.44966 | 0.38392 |
| $H_3$ | 1.86776 | 1.98191 | 2.27679 |
| $K_1$ ($\mu m^2$) | 0.26824 | 0.25048 | 0.24761 |
| $K_2$ ($\mu m^2$) | 0.27297 | 0.26974 | 0.27522 |
| $K_3$ ($\mu m^2$) | 11.65299 | 11.85968 | 12.39362 |

The results for the Sellmeier parameter determination corresponding to three possible thicknesses of the a priori unknown material, obtained with the nonlinear regression procedure previously outlined. The smaller the total residual reported in

the first row of the Table 7.2.3, the better the corresponding least squares regression fit. Obviously the total residual cannot be exactly zeroed and the procedure gives a lot of such a values corresponding to local minimum of the total residual, being not able to discriminate the best. In fact, as the graphs below show, the Sellmeier parameter found are all able to give a transmittance curve interpolating the experimental data (blue tracks in the Figure 7.2.4, 7.2.5, 7.2.6). To mimic the smoothing effect of the measurement instrument, the analytic transmittance values obtained after the parameters $\vec{p}$ have been calculated via least squares regression are subjected to a spectral filtering/averaging procedure, to remove the jagging (see the grey tracks in the Figure 7.2.4, 7.2.5, 7.2.6) due to the jump in the transmittance behavior.
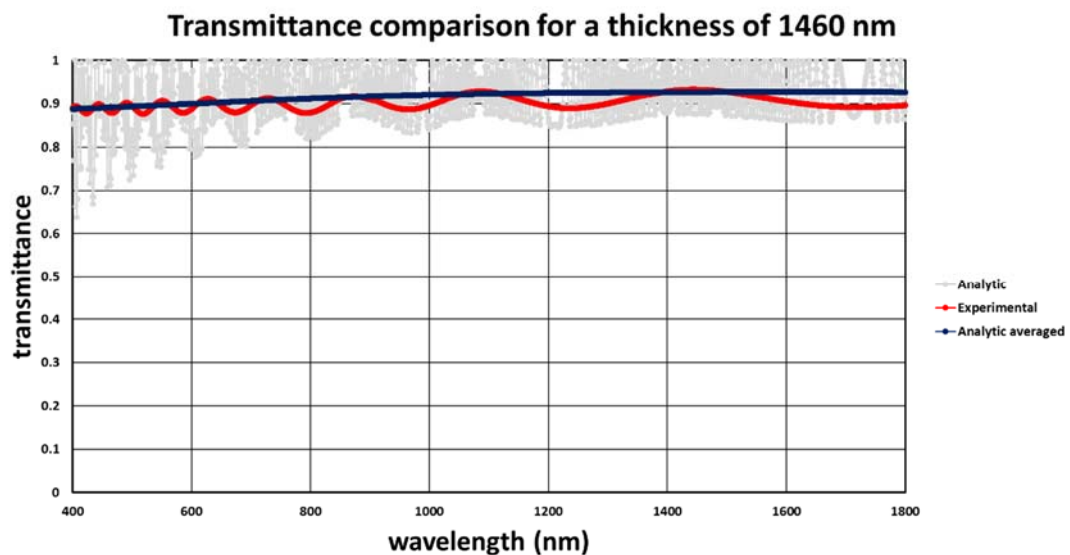


**Figure 7.2.4.** Simulated transmittance of the waveguiding structure with a thickness of 1460 nm.
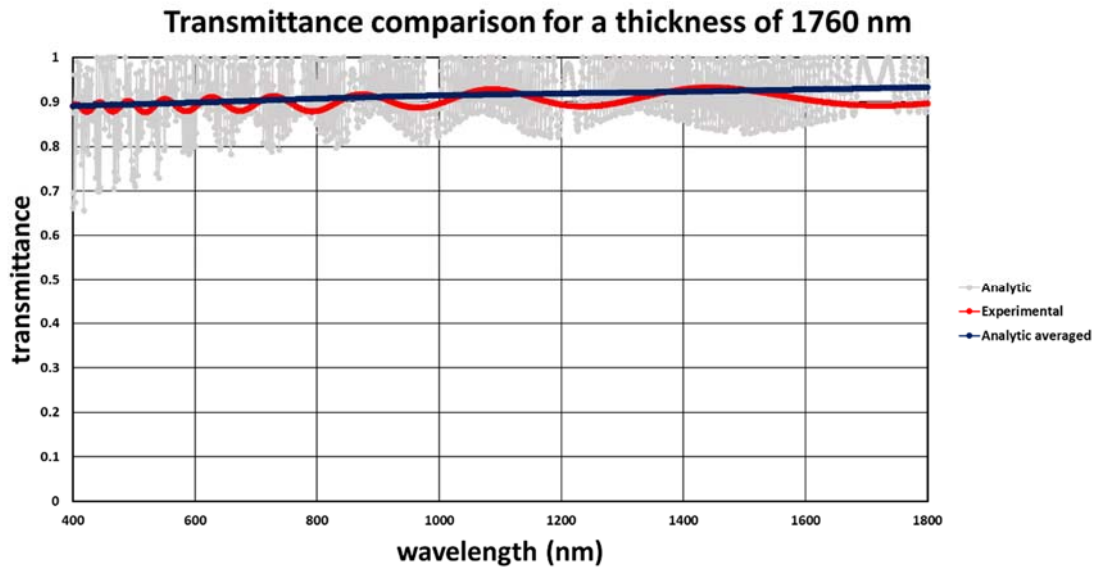
**Figure 7.2.5.** Simulated transmittance of the waveguiding structure with a thickness of 1760 nm.
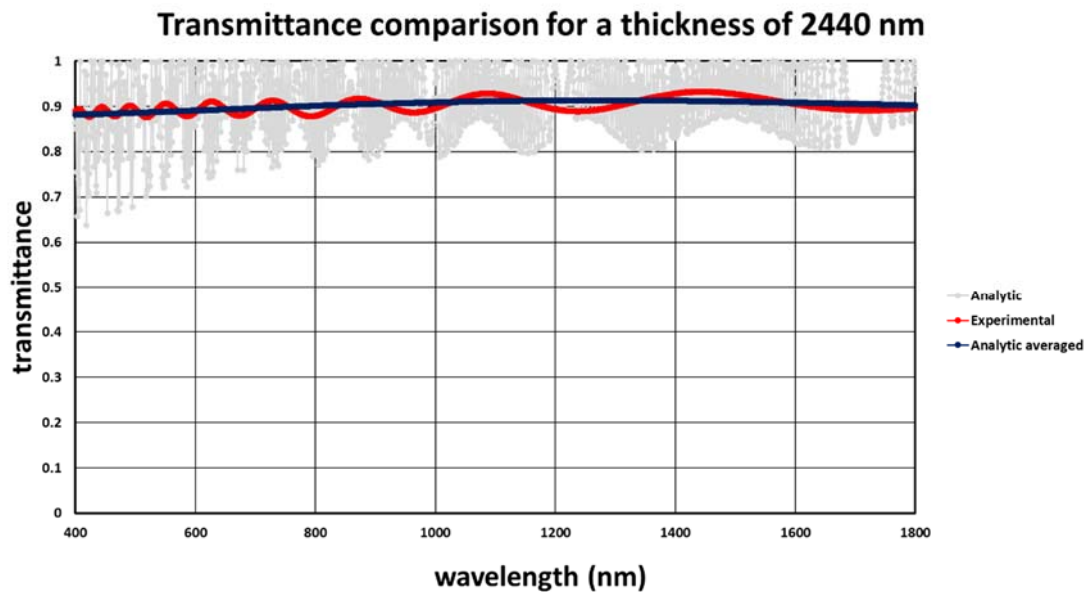


**Figure 7.2.6.** Simulated transmittance of the waveguiding structure with a thickness of 2440 nm.

The next two Figures show how the Sellmeier parameters reported in the second and fourth columns of the Table 7.2.3 are converted in the curve for the respective refractive indices in the chosen wavelength range (which are also used to calculate the transmittance curves in the previous Figures). These refractive indices are compared with those of the hafnia and silica, which were used as initial guesses

of the recursive procedure for the least squares regression. It is important to note that the weighted average between silica and hafnia was used as the starting guess, but from then the six Sellmeier parameters are adjusted in an individual fashion and not collectively through this weighted average.
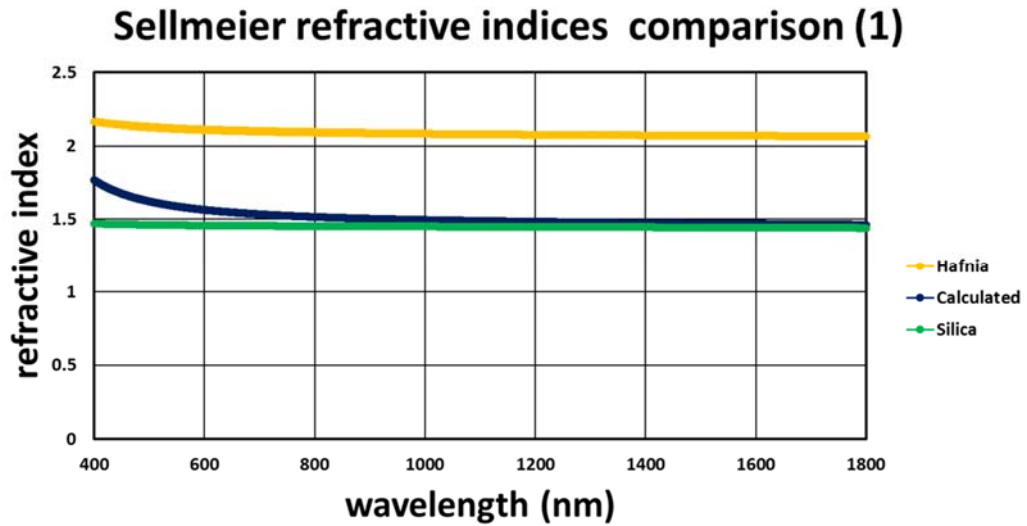


**Figure 7.2.7.** Calculated Sellmier curve of a waveguiding system.
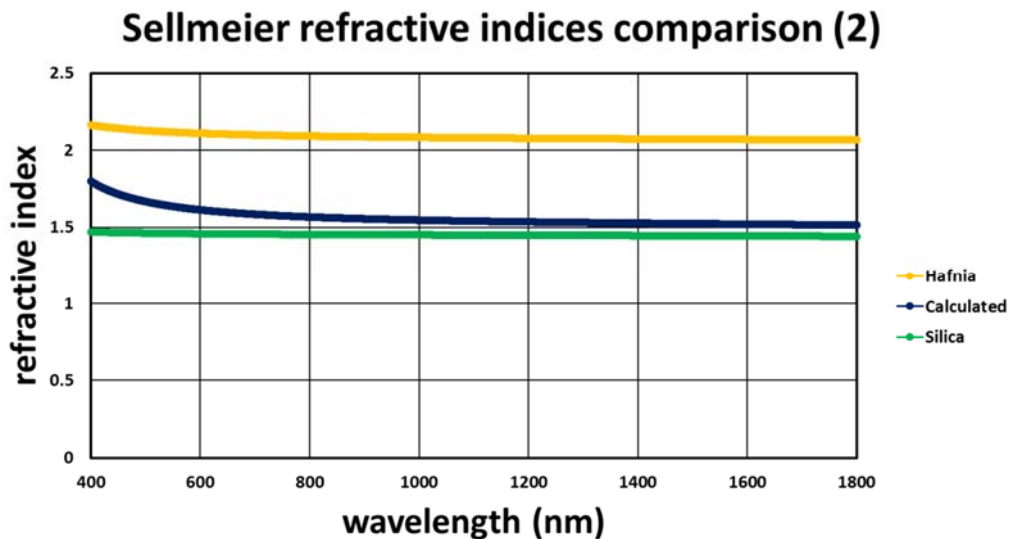


**Figure 7.2.8.** Calculated Sellmier curve of a waveguiding system.

With the given model (Sellmeier equations) and the given experimental data is not possible to perform a better fit and to get further significant reductions in the total residual. More accurate measures and/or more effective and accurate models are needed.

# Bibliography

[Aspnes 1982]  Aspnes, D.E. "Local-field effects and effective-medium theory: A microscopic perspective", Am. J. Phys. 50 (1982), pp. 704-709

[Belka 2014] Belka, R.; Płaza, M.; Suchańska, M.; Ferrari, M. "Optical properties of C-Pd films prepared on silica substrate studied by UV-VIS-NIR spectroscopy", Proc. of SPIE Vol., 9290 (2014), pp. 9290141-9290147

[Huang 1978] Huang, Y.Y.; Sarkar, A.; Schultz, P.C. "Relationship between composition, density and refractive index for Germania silica glasses", J. Non-Cryst. Solids, 27 (1978), pp. 29-37;

[Karpienko 2014] Karpienko, K.; Wróbel, M.S.; Jędrzejewska-Szczerska, M. "Determination of refractive index dispersion using fiber-optic low-coherence Fabry–Perot interferometer: implementation and validation", Opt. Eng., 53 (2014), pp. 0771031-0771038

[Mito 1997] Mito, T.; Fujino, S.; Takebe, H.; Morinaga, K.; Todoroki, S.; Sakaguchi, S. "Refractive index and material dispersion of multi-component oxide glasses", J. Non-Cryst. Solids, 210 (1997), pp. 155-162

[Tan 1998] Tan, C.Z. "Determination of refractive index of silica glass for infrared wavelengths by IR spectroscopy", J. Non. Cryst. Solid, 223 (1998), pp. 158-163

## 8. Stress and strain in a film

Nowadays it is complicated to find any application where sol-gel oxide films are not used: decorative coatings, automobile industry, protective coatings, coatings for photonics and optoelectronics. Sol-gel film could be produced by spin and dip coating techniques from appropriate organic or metal-organic precursors [Teodorescu 2014, Brinker 1990]. Spinned or dipped films are amorphous and soft because they still contain solvent and precursor species. In order to remove solvent drying is used. To complete removal of precursor residues and support densification of the structure is necessary to tailor a suitable heat treatment regime. In our case we have a dense amorphous structure with a high density of nanopores. For the formation of the final densified film nanostructure the annealing step at high temperatures has to be applied [Teodorescu 2014].

The morphology and the structure of thick multilayer sol-gel films, obtained by multiple depositions from sol-gel solutions are different for each deposited layer, because of different number of annealing time for each deposited layer.

Annealing temperature and atmosphere has influence on film porosity, surface morphology and stress development in the oxide lattice or at the interface between the substrate and layer. Also this stress can appear from the defects in the film or in the substrate, leading to cracking and film delamination [Teodorescu 2014].

Stress $\sigma$ is the force per unit area that is acting on a surface of a solid (Pa, $N/m^2$).
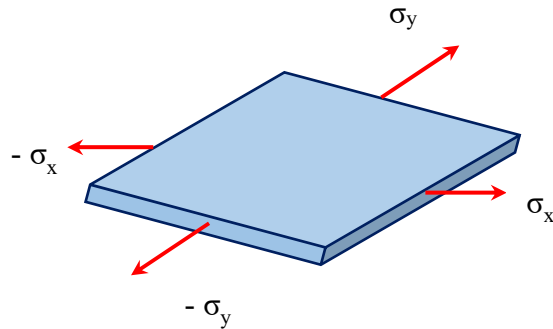
**Figure 8.1.** Stress on a differential volume in static equilibrium.

The state plane stress in thick films will not appear in $z$ direction, normal to the substrate, and the shear stress which appears along the surface can be eliminated. Any vertical deformations are freely moves in $z$ direction and will not affect stress in a substrate.

Suppose that the system is in static equilibrium and no significant external forces act on the system. The two elements of stress are shown in the Eq.47:

$$\sigma = \begin{pmatrix} \sigma_x & 0 \\ 0 & \sigma_y \end{pmatrix} \quad (47)$$

Thin films are stressed even without applications any force on it, what means that the residual (intrinsic) stresses are present in thin films always. Two types of residual stress can be indicated: compressive (minus sign) or tensile (positive sign). When any load applied for free body to push or pull it out of shape, a term "strain" is used for that deformation characterization. Strain $\varepsilon$ is a measure of this deformation. Strain is a nondimensional variable. Since strain is caused by stress in static equilibrium conditions and the same coordinates system can be used. Oxide materials as well as Silicon, nitrides are elastic (no plastic) and comply Hook's law. Practically it means that they deform linearly with load. Stress and strain are linearly related since load is proportional to stress and deformation is proportional to strain:

$$\begin{pmatrix} \varepsilon_x \\ \varepsilon_y \end{pmatrix} = \begin{pmatrix} H_{11} & H_{12} \\ H_{21} & H_{22} \end{pmatrix} \begin{pmatrix} \sigma_x \\ \sigma_y \end{pmatrix} = H \begin{pmatrix} \sigma_x \\ \sigma_y \end{pmatrix} \qquad (48)$$

Matrix $H$ has only two independent elements or two elastic constants: the elastic modulus or Young's Modulus E and the Poisson ratio $v$.

$$H = \begin{pmatrix} 1/E & -v/E \\ -v/E & 1/E \end{pmatrix} \qquad (49)$$

An isotropic material represents $\varepsilon = \varepsilon_x = \varepsilon_y$, where the in-plane or biaxial stress $\sigma = \sigma_x = \sigma_y$ is equal to the ratio $E/1 - v$ (biaxial modulus). In case when the film was subjected only to uniaxial stress (i.e. the film is restricted to move only in one direction), the stress can be determined from Eq.50:

$$\sigma = E \cdot \varepsilon \qquad (50)$$

This equation has some limitations and not used in presence of internal residual stress, because stress in this case is a sequence of thermal or growing effect in all directions and not arised under external load.

One more important parameter is the elastic modulus or Young's Modulus E. Elastic Modulus (Young's Modulus) means elongation of the material under a given load (Pa, N/m$^2$), characterizing material resistance to elastic deformation. The higher the material elastic modulus, the lesser it deforms for a given stress. When uniaxial tensile stress is considered, the material has an expansion in the direction of stress and shrinkage in perpendicular to the stress direction.

Another dimensionless parameter is the Poisson ratio that shows the ratio of the transverse to the axial strain, in other words the ratio between the shrinkage and the elongation.

The volume of the element is changing as a function of strain proportionally to $(1-2v)$.

Young's modulus and Poisson ratio derived from bulk samples and in some situations is not be perfectly suitable for materials in micromachined devices. To obtain Poisson ratio and Elastic modulus values the bending beam and resonant beam techniques may be used [Lu 2011, Puchegger 2005].

Using first method Young's modulus value is measured as the force displacement curve by loading the tip of a cantilever using a nanoindenter. Second technique is based on the measuring the resonant frequency of a beam under excitation. The Poisson ratio for thin films is more difficult to measure than the Young's modulus as thin films tend to bend out of plane in response to in-plane shear [Sharpe 1997, Qi 2005].

## 8.1 Stress and strain formation in thin films

In the thin films residual stress can be uniform or non-uniform through the depth. An average stress can be obtained if the stress is uniform. When the stress is proportional to the average relaxed strain, and in such a way the stress gradient will lead to relaxed strain gradient. Non-uniform stress arises when a difference of stress or stress gradient exists between the top and the bottom of the film. The stress gradient can be measured and considered as an average stress through the depth taking into account the vertical variation of stress. No relaxed strain will occur if a body is stressed and remain motionless, but deformation occurs. The body is under residual stress and residual strain, but no relaxed strain. When the stressed body is allowed to move, it will relax until equilibrium achieved and then will be deformed. There are two kinds of stresses exist: extrinsic and intrinsic.

The extrinsic stresses occur under such external factors such as temperature gradients. This kind of stresses is uniform through the depth and it is called thermal mismatch stress. Extrinsic stress occurs when material has inhomogeneous thermal expansion coefficients exposed to uniform temperature change.

To study the mechanism of thermal mismatch stress generation in thin films, consider the typical structure presented in Figure 8.1.1.
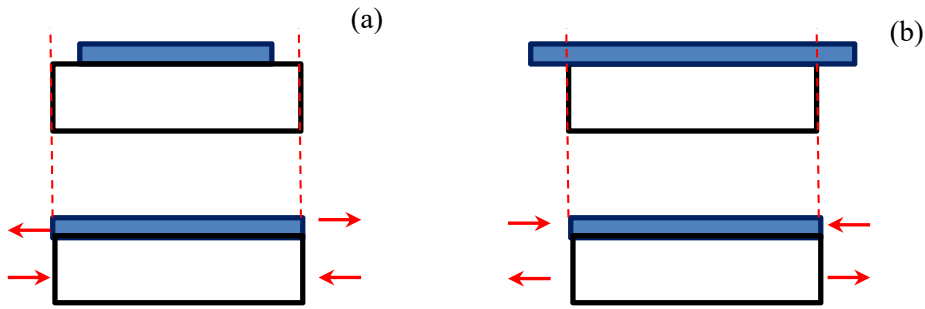
**Figure 8.1.1.** Occurrence of residual tensile stress in film; (b) residual compressive stress in film.

In Figure 8.1.1 (a) the growing film shrinks relative to the substrate. Assuming that the film and the substrate have the same length, the substrate undergoes slight shrinkage in the plane and the film is subjected significant shrinkage.

The thin film was deposited on the substrate at an elevated temperature. In general the thin film and substrate have different thermal expansion coefficients. The thermal expansion coefficient of a material can be defined as:

$$\alpha = \frac{d\varepsilon}{dT} \qquad (51)$$

Due to the fact that the thermal expansion coefficients depend on temperature, the strain caused by thermal expansion is given in Eq. 52:

$$\varepsilon\,(T) = \varepsilon\,(T0) + \alpha \cdot \Delta T \qquad (52)$$

The first part of this equation is practically negligible and the last part caused by thermal expansion. The causes of stress and strain occurrence in thin films because the thermal expansion coefficients mismatch of the film and substrate, when the film is much thinner than the substrate where it deposited on at elevated temperature, and cooled to ambient temperature.

The tensile forces developed in the film are compensated with the compressive forces in the substrate. To achieve mechanical equilibrium and eliminate any of the uncompensated end moments in the system forces (F) and bending moments (M) should be vanished on any film/substrate cross section. In motion free structure it will tend to oppose the unbalanced moments. In this case the film is bent to

the substrate concave upward. Internal compressive stresses, therefore, bend the substrate, Fig. 8.1.1 (b).

Since the substrate is thicker than the film, it is necessary to assume the substrate in the absence of the film:

$$\varepsilon_s = -\alpha_s \,.\, \Delta T \qquad (53)$$

where $\alpha_S$ is the coefficient of thermal expansion for the substrate and the minus sign, the compression of the film. The film then gets this same strain due to the fact that it is attached to the substrate.

$$\varepsilon_{f,attached} = -\alpha_s \cdot \Delta T \qquad (54)$$

When the film was unattached, the strain can be determined in Eq. 55:

$$\varepsilon_{f,free} = -\alpha_f \cdot \Delta T \qquad (55)$$

where $\alpha_f$ represents the coefficient of thermal expansion for the thin film.

The thermal mismatch strain is a difference between the strains film features with and without attachment to the substrate, Eq. 56:

$$\varepsilon_{f,mismatch} = \varepsilon_{f,attached} - \varepsilon_{f,free} = (\alpha_f - \alpha_s) \,.\, \Delta T \qquad (56)$$

Assuming that the thermal mismatch leads to stress in the film, the thermal mismatch can be rewritten for biaxial system:

$$\sigma_{f,mismatch} = \frac{E}{1-v} \cdot (\alpha_f - \alpha_s) \cdot \Delta T \qquad (57)$$

It is accepted that tensile stress is positive, compressive stress is negative. Therefore, if $\alpha_f < \alpha_s$, a compressive stress will be expected and if $\alpha_f > \alpha_s$, a tensile stress will appear.

In general, in thin and multilayered films three kinds of stresses could be marked out: intrinsic, thermal and mechanical. Intrinsic stresses arise during the deposition process of films fabricated by sputtering, spraying, painting, spin coating, vapor deposition, and electro-deposition. Intrinsic stresses include phase transition, grain growth, sintering, defects formation and not quantatively. Vacancy annihilation cause change in volume producing stresses due to the constraint of the substrate or other layer. As a result, a film on a substrate will have intrinsic tensile stress. Intrinsic stress result in a change in volume which then produces stresses

due to the constraint of the substrate or other layers. There is possibility that the residual stresses can comprise both thermal and intrinsic contributions when the temperature is different from the deposition temperature.

Generation of intrinsic stress is caused by internal structure of a material during the deposition process. Different factors during deposition can influence on intrinsic stress occurrence, such as deposition rate, deposition temperature, pressure, incorporation of impurities during growth, grain growth and their structure, fabrication process defects. Since intrinsic stress is usually non-uniform it causes the stress gradient generation. For instance, the Phosphorous doped polysilicon is expected to be more compressive than pure polysilicon because the Phosphorous atom is larger than Silicon [Krulevitch 1992, Biebl 1995]. Silicon doped with Boron exerts a tensile stress into the crystal lattice. When this occurs and the smaller Boron atom displaces the Silicon atom, therefore the lattice is contracted locally. After contraction the Silicon lattice will restrain and in the issue a local tensile stress appears.

Intrinsic stress can sometimes be removed during annealing at the high temperatures and may not be convenient for the production of micromechanical devices.

Stress can be measured using two techniques: For the stress measurements in thin films two kind of techniques are commonly used. First is a substrate curvature technique [Doerner 1986] and the second technique is based on micromachined microstructures of thin dielectric films.

Thermal stress as a kind of external stresses arise from the mismatch between film and substrate expansion coefficients as well as material transformations upon cooling from firing temperature leads to intrinsic stresses. A way to reduce thermal stresses is to lower a firing temperature. Especially in sol-gel derived films the importance of deposition technique is increased because some additional shrinkage and stresses due to densification process during the early deposition steps appears.

Formation of film stress can have a significant effect on mechanical, electrical, and optical properties, affecting the reproducibility of properties and the reliability of devices. For instance in electroceramic films their ferroelectric properties are dependent on the residual stress and thermal processing stages of film fabrication. Tuttle found that stress of PZT thin films during the firing affected the microstructure by regulating the relative populations of *a* versus *c* domains. Domains preferentially aligned either parallel (*c* or 180° domains) or perpendicular (*a* or 90° domains) to the substrate, depending on the magnitude and sign (tensile or compressive) of the in-plane stress as the film is cooled through the transition temperature [Tuttle 1996].

In the work of Lee and co-workers is showed that the piezoelectric response PZT films under compressive stress during the firing process was improved, while Lappalainen et al. found an improvement in the dielectric constant of PZT film with thickness increasing and residual stress decreasing [Lee 1992, Lappalainen 1994]. The importance of drying and densification steps for sol-gel films were proved in a number of studies

In the work of Scherer the drying process of PZT sol-gel films was presented as a complex interrelation between evaporation step, deformation of the solid phase and fluid flow in the gel network. PZT sol-gel films under heating are assayed shrinkage and densification. Starting from 100-130 °C solvents evaporation occurred and gel network squeeze [Scherer 1986, Scherer 1988].

Corkovic and Zhang studied residual stresses development in the sol-gel-derived ferroelectric thin films upon thermal treatment due to the thermal and elastic mismatch between the $Pb(Zr_x,Ti_{1-x})O_3$ (PZT) film and the substrate materials during cooling. Using the wafer curvature method after the deposition of multilayer PZT film on platinized (100) Silicon wafers residual stresses were determined. Higher residual stress was found in PZT films consisting of only rhombohedral crystallographic structure (PZT 60/40) [Corkovic 2007].

Bruchhaus performed detailed stress analysis of sputter deposited PZT films of various compositions [Bruchhaus 1999].

Fardad shows the shrinkage of $SiO_2$ sol-gel films as a function of annealing temperature for each used acid catalyst [Fardad 1995].

In the work of Cooney and Francis it was investigated sol-gel PZT films cracking and delamination depending on the heat treatment temperature. Cracks and delamination occurs as a result of stress development in the coating. Stress in the film arisses from strain developed from constrained shrinkage and thermal expansion mismatch. Stress concentration and distribution is different at the edges, external inclusions, vertical steps and surface irregularities stress concentration and distribution is different. They observed that cracks in sol-gel films arise during the final thermal treatment at 700 °C. During this heat treatment stress is higher because the coating has a high elastic modulus and the thermal expansion coefficient T mismatch stress strain is high due to the larger temperature range over which stress occurs [Cooney 1996].

During the film fabrication process the significant film shrinkage appears on the surface of the substrate. In most of cases shrinkage occurs during the solvent evaporation and morphological changes because of organic part removal and further crystallization step. For sol-gel films deposited on cold substrate (room temperature), the instantaneous residual stress, arised during the deposition and thermal treatment, is related to a thermo-elastic stress due to the difference between the thermal expansion coefficients of the film and its substrate. An intrinsic stresses occur with growth mechanisms, phase transformation and film crystallization. During the cooling process occurs the relaxation of residual stress.

Ong and co-workers studied the effect of the thickness and residual stress of sol-gel derived $Pb(Zr,Ti)O_3$ thin films on the dielectric and piezoelectric properties of the polarizable and deformable material. For that they used Ex-situ wafer curvature measurements, combined with cross-sectional scanning electron microscopy, allowed for the determination of residual stresses in the thin films calculated by the Stoney equation. Residual stress in the film explained due to constrained

shrinkage during drying, pyrolysis, crystallization, and thermal expansion mismatch between the film and substrate on cooling.  In this study the show the apparent change in calculated residual stress, with increasing film thickness. For the films with residual tensile stress and  an inseparable thickness component, they reached dielectric constant values increasing by up to 33 % as residual stress was reduced by  ~ 900MPa [Ong 2005].

Sengupta et al. study stress development in thin sol-gel layers of Lead titanate   by in situ laser reflectance measurements. The shrinkage normal to the rigid substrate was determined by in situ ellipsometry. They explained densification and stress development that occurred on drying and firing with evaporation and solvent/polymeric network interactions at lower temperatures, and thermal expansion mismatch between the substrate and the film. In the study they showed the importance of the choice of substrate material, deposition method and heat treatment conditions, in relation to stress development and dependent electrical properties [Sengupta 1995].

In multilayered coatings where the total coating thickness is much less than the substrate thickness, the total stress is affected by the stress developed in each layer, and if the stress response for each subsequent layer were identical to that of the first, the composite stress could easily be predicted for the multideposited coating. It was found that in multilayered coatings stress development depends on the structure of the coating.

For the coatings fabricated by magnetron sputtering Alagoz Arif and co-workers presents a method of residual stress reduction by stacking low and high material density layers of the same material. They prepared multilayered film by changing gas pressure between high and low allowing formation of nanostructured and dense layers. For the stress evaluation they fabricated Ruthenium films using a DC magnetron sputtering system at alternating Argon  pressures of 20 and 2 mTorr. For intrinsic stresses in thin film calculation of Ru multilayers    coatings as a function of film thickness Wafer's radius of curvature was measured. They were able to reduce film stress more than one order of magnitude in comparison

with the films produced at low working gas pressures. They explained the unusually low of the investigated samples by the model of compliant sublayers [Alagoz 2009].

Intrinsic stress appears with growth of thickness with sputtering of thin films. Researchers already tried to study dependence of residual stress on process parameters and microstructure.

Windischmann reported about correlation of intrinsic stress and Thornton's structure zone model (SZM) for sputtered thin films. They have almost zero intrinsic stress for low density thin films deposited at high Argon pressure and low temperature. They achieved these results by converting the tensile stress to compressive stress forming a dense film. This conversion is possible decreasing pressure. The drawback of fabrication such low stress films is that working pressure between tensile and compressive stress state is not feasible because the pressure window is too narrow [Windischmann 1992, Windischmann 1987, Karabacak 2004].

The work of Karabacak et al. showed the reduction of compressive stress in a film by interlacing high density sublayers with low density sublayers. They proposed that a rough compliant underlayer delays the development of compressive stress in the following dense layer over a thickness in the order of the underlayers roughness.

There are shown the significance of working pressure during the deposition on crystal orientation. High and low pressure leads to various crystals texturing in the film. In their work Ruthenium films were deposited by dc magnetron technique at room temperature. Depositions were performed under ultra pure Argon plasma. For deposition high density layers they set the pressure to 2 mTorr in order to and 20 mTorr for low density single layers. The films had different thickness- 15 nm low density films and 17 nm high density films [Karabacak 2005]. For the intrinsic stress calculations they used the Stoney equation [Stoney 1909].

A high compressive intrinsic stress arises in the film fabricated at a low Argon pressure.  After reaching 85 nm single layer  thick, layer peeled off from the substrate. At high Argon pressure is possible to grow 2 μm thick single layers with

tensile intrinsic stress close to zero. During the deposition process at high pressure the anisotropia of Ruthenium flux to the substrate reduced. The shadowing effect during the film deposition which is responsible for the columnar structure formation also enhanced [Ardigo 2014]. They reduced total intrinsic stress of Ruthenium films one order of magnitude compared to the conventional dense films. Very thick films with low stresses can be produced using this density modulation technique. It should be noted, the stress in multilayer film increases slowly as the total thickness increases. This observation can be explained by thermal stress evolution during long deposition times due to the thermal expansion coefficient mismatch between Si substrate (2.6 x$10^{-6}$ K$^{-1}$) and Ru (6.4x$10^{-6}$ K$^{-1}$) film. At thicker films thermal stress stabilized [Chu 1998**].**

## 8.2 Stress measurements. Experimental techniques.

## Stress measurements by substrate curvature method

We consider a composite plate film/substrate of width *w* [Kingery 1976] as in Fig. 8.2.1.
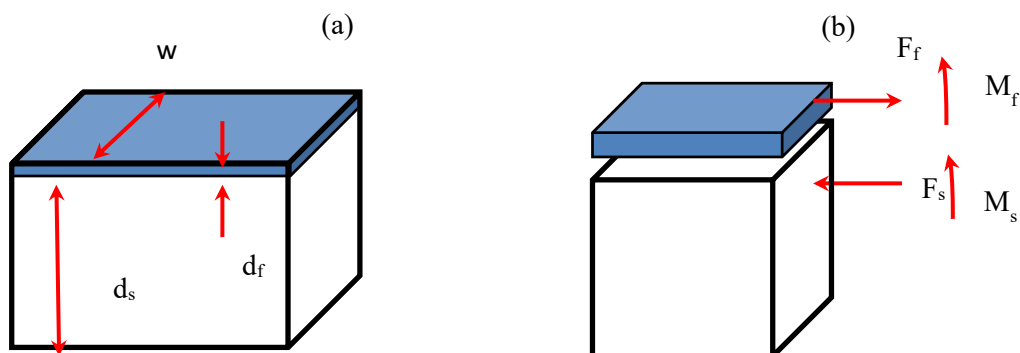


**Figure 8.2.1.** Stress analysis of film/substrate combination: (a) structure; (b) free-body diagrams of film and substrate with forces and end moments.

The film thickness and Young's modulus are $d_f$ and $E_f$, respectively. The corresponding substrate values are $d_s$ and $E_s$. As a result of internal stresses, mismatch forces arise at the film/substrate interface. Using static equivalent combination of a force and moment we can change each set of forces by $F_f$ and $M_f$ in the film, $F_s$ and $M_s$ in the substrate, where $F_f = F_s$ since film and substrate are sticked together. Force $F_f$ can be considered to act uniformly over the cross-sectional area $d_f$, $w$, or on the middle

$$F_f \cdot \frac{d_f}{2} = M_f \qquad (58)$$

or for the complete structure

$$F_f \cdot \frac{d_f + d_s}{2} = M_f + M_s \qquad (59)$$

Considering now an isolated beam segment bent by a moment $M$, the deformation is assumed to entirely consist of the extension or contraction of longitudinal beam fibers by an amount proportional to their distance from the central or neutral axis, which remains unstrained in the process. The stress distribution reflects this by varying linearly across the section from maximum tension $+\sigma_m$ on the top to maximum compression $-\sigma_m$ on the bottom [Kingery 1976].

The length of the neutral axis where the stress equals zero, is given by

$$L_{y=0} = R d\theta \qquad (60)$$

where $R$ is the radius of curvature of the beam segment and $d\theta$, the subtended angle. The length of the section at an arbitrary position $y$ is

$$L_y = (R + y) d\theta \qquad (61)$$

The strain along the $y$ axis is the difference between the length of the neutral axis and the length at position $y$

$$\varepsilon_y = \frac{L_y - L_{y=0}}{L_{y=0}} = \frac{(R+y)d\theta - Rd\theta}{Rd\theta} = \frac{y}{R} \qquad (62)$$

The axial stress is then given by:

$$\sigma_y = E \frac{y}{R} \qquad (63)$$

and the maximum stresses on the top and bottom of the beam are therefore equal to

$$\sigma_m = \pm E \frac{d}{2R} \qquad (64)$$

showing that compressive stress on the top is negative and tensile stress on the bottom is positive.

We can now calculate the bending moment of the beam segment by integrating the stress over the beam section.

$$M = 2 \int_0^{d/2} \sigma_y wy\,dy = E\frac{d^3}{12R}w = \frac{E}{R}I \qquad (65)$$

where $I = \frac{wd^3}{12}$ is called the moment of inertia of a rectangular beam with respect to the center of the beam in a direction perpendicular to one of the sides. By extension of this result, we have

$$M_f = Ef\frac{d_f^3}{12R}w \quad \text{and} \quad M_s = E_s\frac{d_s^3}{12R}w \qquad (66)$$

Finally, in order to account for actual biaxial-stress distribution in films, rather than the uniaxial stresses assumed for ease of integration, it is necessary to replace $E_f$ by $E_f/1-v_f$ and similarly for $E_s$.

$$F_f\frac{d_f+d_s}{2} = E_f\frac{d_s^3}{12R(1-v_f)}w + E_s\frac{d_s^3}{12R(1-v_s)}w \qquad (67)$$

Since $ds$ is normally much larger than $df$, the equation becomes

$$F_f\cdot\frac{d_s}{2} = E_s\frac{d_s^3}{12R(1-v_s)}w \qquad (68)$$

Furthermore, since $\sigma_f$ is equal to the force $F_f$ acting on the area $wd_f$ or $\sigma_f = F_f/wd_f$, the film stress $\sigma_f$ can be then given by:

$$\sigma_f = \frac{E_s d_s^2}{6(1-v_s)}\cdot\frac{1}{d_f}\cdot\frac{1}{R} \qquad (69)$$

Above mentioned formula called the Stoney equation. Stress values obtained by Stoney approach are an average stress calculated as integral of stress over the section (over the thickness of the beam). This method is useful to measure residual stress in a thin film when their elastic properties unknown. On the contrary, if strain in the thin film must be extracted, its Young's modulus and Poisson ratio must be known. For the film with intrinsic stress or stress gradient, stress calculated by Stoney equation will be the average stress at the middle of the beam. In

curved substrate stress is relaxed when bending, compressive and tensile stresses vanished. The stress is replaced by relaxed strain expressed in this case by the curvature of the substrate.    Thanks to the simplifications ($d_s$        $d_f$ ), only silicon Young's modulus and Poisson ratio must be known to extract the residual stress in any kind of thin films whatever the elastic properties of the film ($E$, $v$ and $\alpha$ values). If strain in the thin film must be extracted, its Young's modulus and Poisson ratio must be known. Without the previous simplification, Stoney could be more rigorously written as

$$\sigma_f = \frac{1}{6R(d_f + d_s)d_f} \left[ \frac{E_f d_f^3}{(1 - v_f)} + \frac{E_s d_s^3}{(1 - v_s)} \right] \qquad (70)$$

requiring to know the complete elastic properties of the thin film.

The Stoney equation assumes substrate with transversal isotropic elastic properties. Validity of the Stoney equation implies that the substrate has transversal isotropic elastic properties with regard to the thin film. Single crystal of Silicon satisfy this  transverse isotropy argument (100 oriented wafers) [Kingery 1976]. Films must also be uniform in thickness and stress must be homogeneous and equibiaxial over the entire substrate. Moreover, films prepared by LPCVD or PECVD characterized not high uniformity compared to homogeneous sputtered films [Kingery 1976].

The Stoney equation is a suitable approximation for thickness ratio $d_f/d_s$ smaller than 10 % [Kingery 1976].In the reference [Kingery 1976] presented modified Stoney formula without information on the layers modulus, to improve calculations for thickness ratios up to 40 %. For a laminated  ($n$ layers) continuous films of thickness $d_{fi}$ on a substrate with athickness $d_s$ always greater than the total films thickness $\sum_1^n d_{fi}$

The total curvature is a sum of each layer contribution because the moments are additive. Each layer independently interacts with the substrate without accounting other layers in laminate [Kingery 1976]. The stress $\sigma_{fi}$ in the film number $i$ therefore yields

$$\sigma_{fi} = \frac{E_s d_s^2}{6(1-v_s)} \cdot \frac{1}{d_{fi}} \cdot \frac{1}{R_i} \qquad (71)$$

and the total stress $\sigma_{total}$ in the $n$ stacked films is

$$\sigma_{total} = \frac{E_s d_s^2}{6(1-v_s)} \cdot \frac{1}{\sum_{i=1}^{n} d_{fi}} \cdot \sum_{i=1}^{n} \frac{1}{R_i} \qquad (72)$$

This formula shows that the total substrate curvature consists of a linear superposition of the bending effects from each of the layer. In other words, the stress in each layer is proportional to the partial curvature in the substrate due to this particular film [Kingery 1976].

Substrate curvature method is a simple estimation of the average stress in the multilayered films. Moreover, this technique doesn't need any photolithographic step and knowledge of Young's modulus and Poisson ratio of the film. An average stress obtained by Substrate curvature method gives an average stress including the presence of the stress gradient. The drawbacks of this method provides the average stress value over the entire test wafer and does not take into account the local fluctuations on the wafer and the fluctuations from one wafer to. In order to get the average strain an elastic properties must be known. Curvature method provides an average stress integrated over the whole thickness of a layer but aside the stress gradient in the film.

## 8.3 Strain measurements using micromachined structures

Substrate curvature method allows getting an average wafer level value of the stress without considering the local values. Local stress is doesn't mean the same as stress measured by substrate bending technique, since stress is defined microscopically, while deformations are mostly induced macroscopically [Kingery 1976]. Residual stress can vary across a wafer or a test wafer to a processed wafer. After wafer processing it is necessary to access local residual stress values [Kingery 1976].

For local film strain measurements used in situ micromachined structures method. Removing underlying Silicon stress thin film relaxed and the residual stress is converted into a deformation of the structure dimensions. This defor-

mation is the relaxed strain proportional to the stress in the thin film before its relaxation. The proportionality is the uniaxial Young's modulus [Kingery 1976]. Young's modulus is therefore required to extract the final average stress from the measured strain.

For in-plane measurements is possible to use Scanning electron microscopy (SEM) or optical microscopy. Optical microscopy has some restrictions that it requires focal plane adjustments are not precise enough for small deflections. Buckling can be investigated by a microscopic interferometry as more sensitive technique [Kingery 1976].

## 8.4 Clamped-clamped beam and ring-and-beam structures analysis Theory

Under compressive stress a double supported beam under compressive will buckle when it is released. This type of structures with different length can be used for compressive strain determination when it is buckled at a given stress level [Kingery 1976]. For this case using the Euler equation for a critical buckling beam of $L_{cr}$ length, the critical starin critical strain $\varepsilon_{cr}$ can be estimated:

$$\varepsilon_{cr} = \frac{\pi^2 h^2}{3L_{cr}^2} \quad (73)$$

where $h$ is the beam thickness, and $L_{cr}$, the critical beam length (i.e. the shorter beam at which buckling occurs).

For each layer thickness, high stress level leads to a shorter critical buckling beam and reverse. The critical buckling length $L_{cr}$ decreases if the layer thickness $h$ decreases.

Residual strain for each buckled beam can be determined from

$$\varepsilon_C = \frac{\pi^2}{12L^2}(2A^2 + 4h^2) \quad (74)$$

where $A$ is the amplitude of the buckling deflection, $L$ is the beam length and $h$ is the beam thickness. The buckling beam has a sinusoidal shape [Kingery 1976]. A and h were determined by interferometry and ellipsometry measurements, L is obtained from the layout dimensions.

The Equation 74 allows to calculate the residual strain in very thin films with short buckling length for a given critical strain measurement using large beam length than critical Euler buckling length $L_{cr}$ [Kingery 1976].

To study the effect of the strain gradient on clamped beam deflection, the full deflection curve should be compared [Kingery 1976] with a two-dimensional finite difference model. The gradient affects the evaluation of the transition and prebuckled beams [Kingery 1976].

In our research we for stress calculations we used Kingery formula.
If σ (1 and 2 is the volume fraction of two different phases, respectively) is the stress, V- the volume fraction (equal to the cross sectional area fraction), α is a thermal expansion coefficient, E- elastic modulus and ε the actual strain:

$$\sigma_1 V_1 + \sigma_2 V_2 = 1$$

$$\left(\frac{E_1}{1-\mu_1}\right)(\varepsilon - \varepsilon_1)V_1 + \left(\frac{E_2}{1-\mu_2}\right)(\varepsilon - \varepsilon_2)V_2 = 0$$

If $E_1 = E_2$, $\mu_1 = \mu_2$ and $\alpha_1 = \alpha_2 = \Delta\alpha$

$$\Delta\alpha\Delta T = \varepsilon_1 - \varepsilon_2$$

then

$$\sigma = \left(\frac{E}{1-\mu}\right) V_2 \Delta\alpha\Delta T \quad (75)$$

In order to use the Equation 75 we need to calculate the thermal expansion coefficient of the film with given composition of silica hafnia waveguide. Quartz glass was used as substrate and has a well-known thermal expansion coefficient value presented in the Table 8.4.1.

**Table 8.4.1.** Thermal expansion coefficient.

| Oxides | Thermal expansion coefficient, $\alpha \cdot 10^{-6}$, grad$^{-1}$ |
|---|---|
| SiO$_2$ | 0.55 |
| HfO$_2$ | 3.6 |
| | 5.6 |

| | 5.8 |
|---|---|
| $P_2O_5$ | 0.67 |

**Table 8.4.2.** Compounds of the planar waveguides and their physical-chemical properties.

| Compounds | Molecular weight of compounds | Molecular weight | Thermal expansion coefficient, $\alpha \cdot 10^{-6}$, grad$^{-1}$ | Percentage |
|---|---|---|---|---|
| $Si(OC_2H_5)_4$ | 208.328 | 60.0848 | 0.55 | 70 |
| HCl | 36.461 | | | |
| $H_2O$ | 18.015 | | | |
| $CH_3CH_2OH$ | 46.068 | | | |
| $HfOCl_2 \cdot 8H_2O$ | 409.39 | 210.4888 | 5.8 | 30 |
| **$Er(NO_3)_3 \cdot 5H_2O$** | **443.35** | **382.5182** | | **0.3** |
| **$ZrO_2$** | | **123.2188** | **10.6** | **1.5** |
| | | | | |

For the thermal expansion coefficient calculations of the film it is necessary to transform percentage to mol:

$$\text{Oxide} = \frac{\text{Molar percentage of Oxide}}{\text{Molecular weight of Oxide}}, \text{ mol} \quad (76)$$

Using this equation we obtain mol value for each oxide.

$SiO_2$= 70/60.08= 1.1651 mol

$HfO_2$=30/210.49=0.1423 mol

$ZrO_2$=1.5/123.22=0.0122 mol

$Er_2O_3$=0.3/382.52= 0.000784 mol

The concentration of $ZrO_2$ and $Er_2O_3$ are very low and therefore is not used for calculations.

*Total oxides mol value, m:*

$m$SiO$_2$ + $m$HfO$_2$ =1.1651+0.1423= 1.3074 mol

SiO$_2$=1.1651/1.3074=0.891

HfO$_2$=0.1423/1.3074=0.109

ZrO$_2$=0.0122/1.3204=0.0092

Er$_2$O$_3$=0.000784/1.3204=0.00059

*Total sum of oxides= 1*

Using the literature value of thermal expansion coefficient for silica and hafnia oxide and knowing the mol percentage of each oxide in the composition we obtain $\alpha_m$ silica hafnia matrix thermal expansion coefficient from the Eq. 77:

$$\alpha_m = m_1\alpha_1 + m_2\alpha_2 + m_n\alpha_n \qquad (77)$$

Silica hafnia matrix has a thermal expansion coefficient $1{,}12 \cdot 10^{-6}$

By the same of calculations we obtain the thermal expansion coefficients for the different Silica Hafnia compositions.

**Table 8.4.3.** Thermal expansion coefficient of different silica hafnia matrices.

| Waveguide | Thermal expansion coefficient, $\alpha \cdot 10^{-6}$, grad$^{-1}$ |
|---|---|
| 70SiO$_2$ – 30HfO$_2$ | 1,12 |
| 75SiO$_2$ – 25HfO$_2$ | 1,01 |
| 80SiO$_2$ – 20HfO$_2$ | 0,89 |
| 90SiO$_2$ – 10HfO$_2$ | 0,71 |

Results of stress calculations of silica hafnia waveguides is given in a Table 8.4.4.

**Table 8.4.4.** Thermo-mechanical characteristics of $70SiO_2$-$30HfO_2$ waveguide

| Waveguide | Thermal expansion coefficient, $\alpha \cdot 10^{-6}$, $grad^{-1}$ $\alpha_f$ Film | Elastic modulus for Quartz glass, E $kG/cm^2$ | Poisson's ratio for Quartz glass,$\mu$ | $T_0$, °C | T, °C | $\Delta T$, °C | Volume fraction,V, Film | Thermal expansion coefficient, $\alpha \cdot 10^{-6}$, $grad^{-1}$, $\alpha_s$ Substrate | Stress $\sigma$, MPa |
|---|---|---|---|---|---|---|---|---|---|
| $70SiO_2$-$30HfO_2$ | 1,12 | $0.74 \cdot 10^6$ | 0.17 | 20 | 400 | 380 | 0.00025 | 0.55 | 0.004828 |

1 micron=0.0001 cm=0.001 mm

Volume fraction (film): $\dfrac{Film\ thickness}{Film\ thickness + Substrate\ thickness}$=0.0005/2,0005=0.00025

Considering Volume fraction and thermal expansion coefficient we may calculate stress in the film:

$$\sigma = (\frac{E}{1-\mu})V_2\Delta\alpha\Delta T \qquad (78)$$

$\alpha$=(0.74·$10^6$/1-0.17)·0.00025·0.57·$10^{-6}$·380=0.04828 $kG/cm^2$

**Table 8.4.5.** Stress values in the films of different thickness and substrate.

| Waveguide | Thickness of the film, mm | Volume fraction of the second phase | $T_0$, °C | T,°C | $\Delta T$,°C | Stress, Mpa |
|---|---|---|---|---|---|---|
| **Film** | | | | | | |
| $70SiO_2$-$30HfO_2$ | 0.0005 | 0.00025 | 20 | 400 | 380 | 0.004828 |
| | | | | 500 | 480 | 0.00609 |
| | | | | 600 | 580 | 0.00737 |
| | | | | 700 | 680 | 0.00864 |
| | | | | 800 | 780 | 0.00991 |
| | | | | 900 | 880 | 0.01118 |
| | 0.0007 | 0.00035 | 20 | 400 | 380 | 0.00676 |

| | | | | 500 | 480 | 0.00854 |
|---|---|---|---|---|---|---|
| | | | | 600 | 580 | 0.01032 |
| | | | | 700 | 680 | 0.01209 |
| | | | | 800 | 780 | 0.01387 |
| | | | | 900 | 880 | 0.01565 |
| | 0.001 | 0.0005 | 20 | 400 | 380 | 0.00966 |
| | | | | 500 | 480 | 0.01219 |
| | | | | 600 | 580 | 0.01474 |
| | | | | 700 | 680 | 0.01728 |
| | | | | 800 | 780 | 0.01982 |
| | | | | 900 | 880 | 0.02236 |
| | 0.0015 | 0.0007 | 20 | 400 | 380 | 0.01352 |
| | | | | 500 | 480 | 0.01708 |
| | | | | 600 | 580 | 0.02063 |
| | | | | 700 | 680 | 0.02419 |
| | | | | 800 | 780 | 0.02775 |
| | | | | 900 | 880 | 0.03130 |
| **Substrate** | | | | | | |
| $SiO_2$ glass | 2 | 0.999 | 20 | 400 | 380 | 9.646 |
| | | | | 500 | 480 | 12.185 |
| | | | | 600 | 580 | 14.723 |
| | | | | 700 | 680 | 17.262 |
| | | | | 800 | 780 | 19.800 |
| | | | | 900 | 880 | 22.338 |

Stress development in the film of different thickness is given in the Figure 8.4.6.
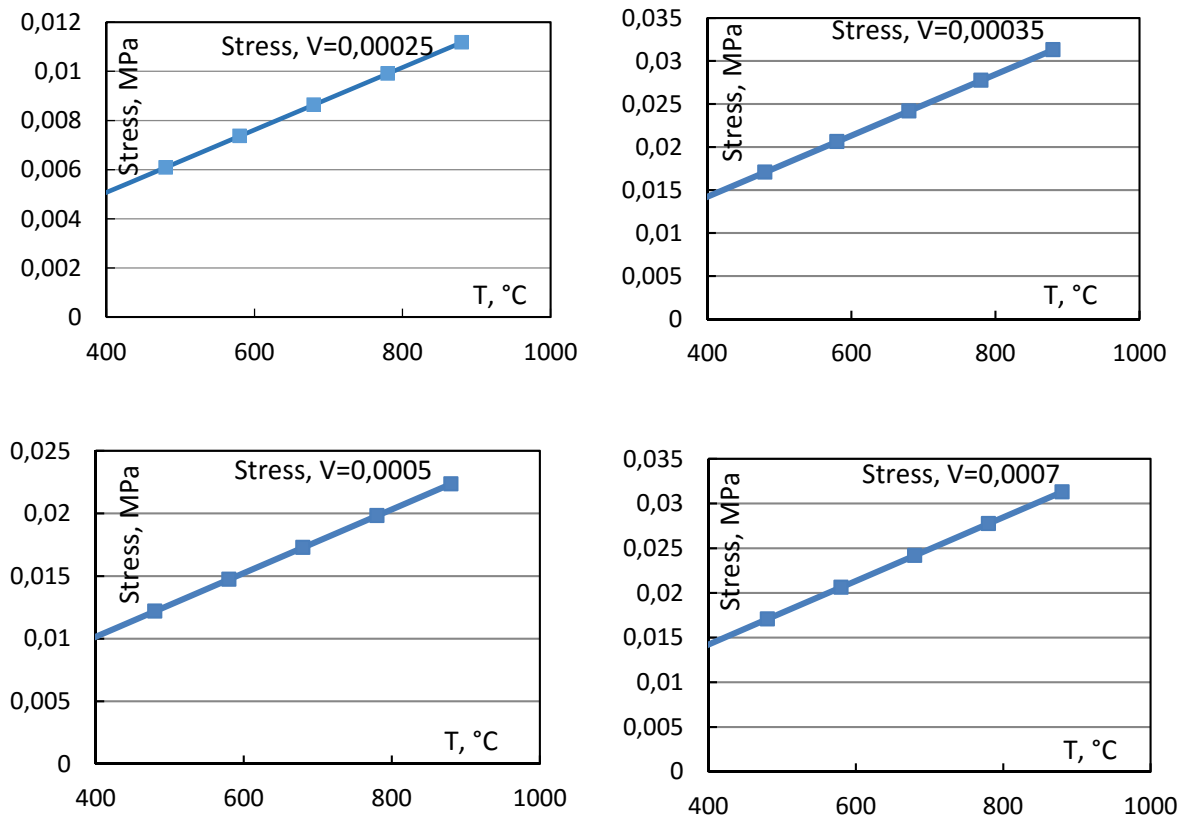
**Figure 8.4.6.** Stress development in films with different thickness.

Form the graph we observe constant raising in the stress level at increasing temperatures that is due to thermal expansion coefficient mismatch between the the film and the substrate, α for silica hafnia system is $1.12 \cdot 10^{-6}$ and for quartz substrate α is $0.55 \cdot 10^{-6}$.

In practice it means for the thermal annealing procedure it is necessary to apply slow cooling up to 500 °C, because after the stress value is double, that can be explained a huge difference for the thickness of the film and the substrate, as a consequence he substrate is cooling slower than a very thin film.
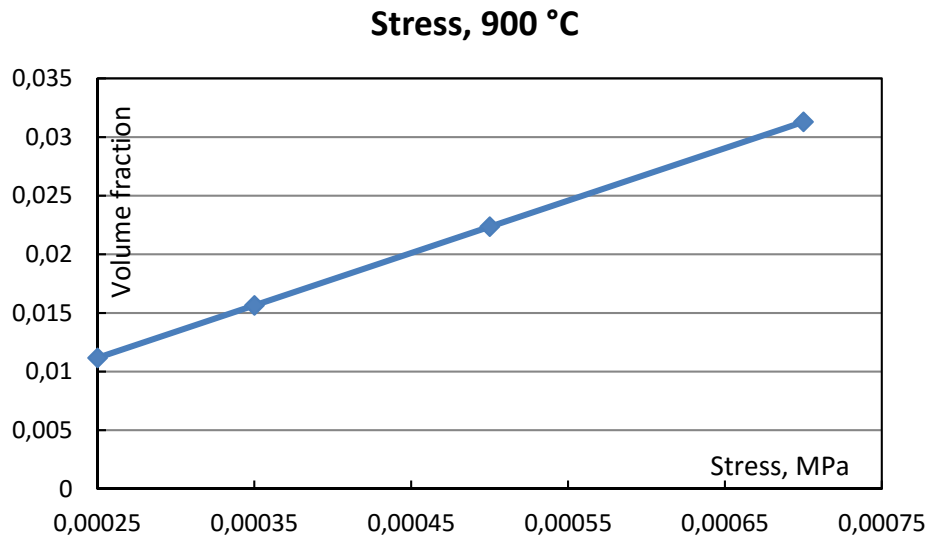
**Figure 8.4.7.** Stress development for the films with different thickness at the working temperature.

Figure 8.4.7 shows the stress level at the working temperature for the films with increasing thickness value. We can see that increasing the film thickness with have an increase in stress value.

The deformation that substrate is undergo during the heat treatment has an influence on the overall stress development of multilayered structure. The calculated stress in the substrate is given below.

Volume fraction (substrate): $\dfrac{Substrate\ thickness}{Film\ thickness+Substrate\ thickness}$=1/1,0005=0.999

$\sigma = (\frac{E}{1-\mu})V_2\Delta\alpha\Delta T$

$\sigma =(0.74\cdot10^6/1\text{-}0.17)\cdot0.999\cdot0.57\cdot10^{-6}\cdot380=192{,}92$ kG/cm$^{2}$[1]

**Stress, substrate V=0,999**
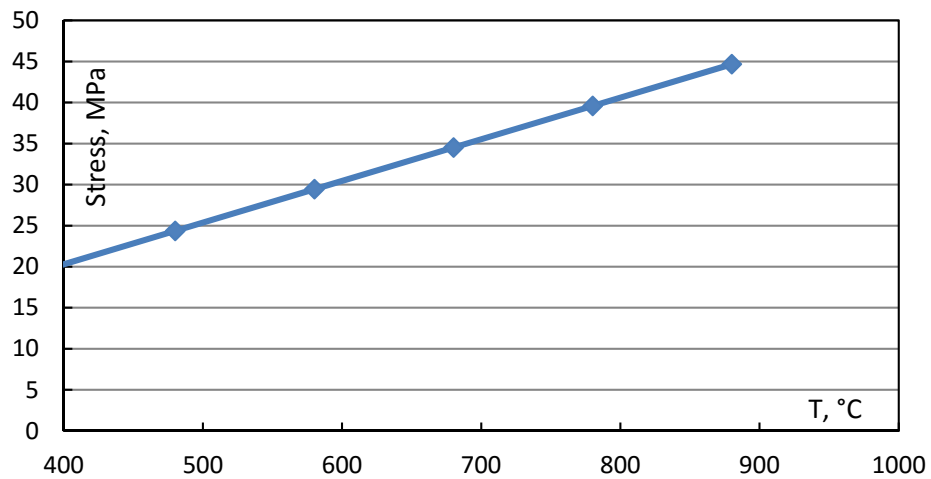
**Figure 8.4.8.** Stress development in the substrate.

The stress generation in the substrate shows the same tendency that for case of the interface between film and substrate - increasing of the stress value with the temperature. That shows that the annealing and post annealing steps during thin film fabrication has a strong influence and importance on cracks and defects formations in thin films, at the worst leading to failure, therefore annealing regime must be properly developed.

# Bibliography

[Alagoz 2009] Alagoz, A.S.; Kamminga, J-D.; Grachev, S.Y.; Lu, T.M.; Karaba-cak, T. "Residual Stress Reduction in Sputter Deposited Thin Films by Densi-ty Modulation", Materials Research Society, 1224 (2009), pp. 27-32

[Ardigo 2014] Ardigo, M.R.; Ahmed, M.; Besnard, A. "Stoney formula: Investiga-tion of curvature measurements by optical profilometer", Advanced Materials Research, 996 (2014), pp. 361-366

[Biebl 1995] Biebl, M.; Mulhern, G.T.; Howe, R.T. "In situ phosphorus doped polysilicon for integrated MEMS", IEEE, (1995), pp. 198-201

[Brinker 1990] Brinker, C.J.; Scherer, G.W. 'Sol-Gel Science: The physics and Chemistry of sol-Gel Processing', Academic Press, (1990)

[Bruchhaus 1999] Bruchhaus, R.; Pitzer, D.; Primig, R.; Schreiter, M; Wersing, W., "Sputtering of PZT thin films for surface micromachined IR-detector ar-rays", INTEGR FERR, 25 (1999), pp. 341-351

[Chu 1998] Chu, S.N.G. "Elastic Bending of Semiconductor Wafer Revisited and Comments on Stoney's Equation", J. Electrochem. Soc., 145 (1998), pp. 3621-3627

[Cooney 1996] Cooney, T.G.; Francis, L.F. "Processing of sol-gel derived PZT coatings on non-planar substrates", Journal of Micromechanics and Microen-gineering, 6 (1996), pp. 291-300

[Corkovic 2007] Corkovic, S.; Zhang, Q.; Whatmore, R.W. "The investigation of key processing parameters in fabrication of Pb(Zr Ti-x(1-x))O-3 thick films for MEMS applications", Springer, (2007), pp. 295-301

[Doerner 1986] Doerner, M.F.; Gardner, D.S.; Nix, W.D. "Plastic Properties of Thin Films on Substrates as Measured by Sub-Micron Indentation Hardness and Substrate Curvature Techniques", J. Mater. Res., 1 (1986), pp. 845-851

[Fardad 1995] Fardad, M.A.; Yeatman, E.M.; Dawnay, E.J.C.; Green, M.; Horowitz, F. "Effects of $H_2O$ on structure of acid-catalyzed $SiO_2$ sol-gel films", Journal of Non-Crystalline Solids, 183 (1995), pp. 260-267

[Karabacak 2004] Karabacak, T.; Picu, R.C.; Senkevich, J.J.; Wang, G.-C.; Lu, T.-M. "Stress reduction in tungsten films using nanostructured compliant layers", Journal of Applied Physics,96 (2004), pp. 5740-5746

[Karabacak 2005] Karabacak, T.; Senkevich, J.J.; Wang, G.-C.; Lu, T.-M. "Stress reduction in sputter deposited films using nanostructured compliant layers by high working-gas pressures", J. Vac. Sci. Technol. A, 23 (2005), pp. 986-990

[Kingery 1976] Kingery, W.D.; Bowen, H.K.; Uhlmann, D.R. "Introduction to ceramics", Wiley-Interscience, 2 (1976), p. 1056

[Krulevitch 1992] Krulevitch, P.; Johnson, G.C.; Howe, R.T. "Stress and microstructure in phosphorus doped poly-crystalline silicon", Mater. Res. Soc. Symp. Proc., 276 (1992), pp. 79–84

[Lappalainen 1994] Lappalainen, J.; J. Frantti, J.; Leppävuori, S. "Characterization of Post - Annealed PZT Thin Films Deposited Using Pulsed Laser Ablation", Materials Research Society , 361 (1994), pp. 581

[Lee 1992] Lee, H.M.; Chuang, T.J.; Chiang, C.K.; Cook, L.P.; Schenck, P.K. "Crack Development in Pulsed Laser-Deposited Pzt Thin Films", Materials Research Society, 285 (1992), pp. 409-414

[Lu 2011] Lu, K.H.; Ryu, S-K.; Zhao, Q.; Hummler, K; Im, J.; Huang, R.; Ho, P.S. "Temperature-dependent thermal stress determination for through-silicon-vias (TSVs) by combining bending beam technique with finite element analysis", IEEE, (2011), pp. 1475-1480

[Ong 2005] Ong, R.J.; Berfield, T.A.; Sottos, N.R.; Payne, D.A. "Sol-gel derived Pb(Zr,Ti)O3 thin films: residual stress and electrical properties", J. of the Europ. Ceram. Soc., 25 (2005), pp. 2247-2251

[Puchegger 2005] Puchegger, S.; Loidl, D.; Kromp, K.; Peterlik, H.; Weiß, R. "Extension of the resonant beam technique to highly anisotropic materials", Journal of Sound and Vibration, 279 (2005), pp. 1121-1129

[Qi 2005] Qi, H-y.; Zhou, L-Z.; Yang, X-g. "Measurement of Young's Modulus and Poisson's Ratio of Thermal Barrier Coatings", Chinese Journal of Aeronautics, 2 (2005), pp. 180-184

[Scherer 1986] Scherer, G.W. "Drying gels: I. General theory", Journal of Non-Crystalline Solids, 87 (1986), pp. 199-225

[Scherer 1988] Scherer, G.W. "Aging and drying of gels", Journal of Non-Crystalline Solids, 100 (1988), pp. 77-92

[Sengupta 1995] Sengupta, S.S.; Roberts, D.; Li, J.F.; Kim, M.C.; Payne, D.A. "Field-induced phase switching and electrically driven strains in sol-gel derived antiferroelectric (Pb,Nb)(Zr,Sn,Ti)O3 thin layers", J. Appl. Phys., 78 (1995), pp. 1171 -1177

[Sharpe 1997] Sharpe, W.N.; Yuan, B.; Vaidyanathan, R. "Measurements of Young's modulus, Poisson's ratio, and tensile strength of polysilicon", IEEE, (1997), pp. 424-429

[Stoney 1909] Stoney, G.G. "The tensions of metallic films deposited by electrolysis", Proc. R. Soc. Land.. A82 (1909), pp. 172-175

[Teodorescu 2014] Teodorescu, V.S.; Blanchin, M-G. "TEM study of the sol-gel oxide thin films", (2014), pp. 903-908

[Tuttle 1996] Tuttle, B.A.; Schwartz, R.W. "Solution deposition of ferroelectric thin-films", MRS bulletin, 21 (1996), pp. 49-54

[Windischmann 1992] Windischmann, H. "Intrinsic stress in sputter deposited thin films", Crit. Rev. Solid State Mater. Sci., 17 (1992), pp. 547-596

[Windischmann 1987] Windischmann, H. "An intrinsic stress scaling law for polycrystalline thin films prepared by ion beam sputtering" ,J. Appl. Phys. 62 (1987), pp. 1800-1807

# Conclusions and Perspectives

This work shows that it is possible to fabricate phosphate-based planar waveguides activated by rare earth ions both by sol-gel and RF-sputtering techniques.

Some important points should be put in evidence:

- In the sol-gel process the role of kinetics of reactions is crucial to have transparent solution. The strength of my research in this sense is that we have evidenced the more important critical points and show-stoppers concerning fabrication of $SiO_2$-$P_2O_5$-$HfO_2$ waveguide by sol-gel technology. Although the sol-gel procedure was not consolidated, and this is a weakness of the study, we can claim that the effect of an important number of different $P_2O_5$ precursors on the optical and morphological properties of the waveguide has been assessed. This is really a positive result of the research allowing to start now from a solid base in chemistry.

- Spectroscopic and optical measurements indicate that we are on the right track to improve luminescence efficiency of sol-gel derived waveguide although the more important drawback is related to devitrification of the structure leading to high propagation losses. However the sol-gel technique allows to prepare $SiO_2$-$HfO_2$-$P_2O_5$ planar waveguides with a good transparency.

- Another important problem, typical of composite materials, is the dispersion curve determination. The topic is clearly of great interest for waveguiding system and especially in the case of $P_2O_5$-$HfO_2$ codoping, where the effect of codoping on the refractive index could be different from the single $P_2O_5$ and $HfO_2$ doping. The more exciting results of this part is the numerical approach that I developed in collaboration with Dr. Alessandro Vaccari allowing to determine the dispersion curve by the transmittance spectra. It is true that the procedure was tested only for silica hafnia, due to the necessary number of available data for a reasonable statistic, but the results are impres-

sive. This kind of measurement and analysis still remain a non-trivial task and the situation is much more complicated in the case of dip-coated waveguides due to the fact that the active film is multilayered and deposited on both the side of the substrate. The presented solution has a general validity allowing the determination of the refractive index of an unknown material from a measured transmittance spectrum.

- RF-sputtering deposition technique allowed us to fabricate low losses waveguides of composition $SiO_2$-$P_2O_5$-$HfO_2$-$Al_2O_3$-$Na_2O$-$Er_2O_3$. It is worthy to note as the RF-sputtering process allow to improve the solubility of the rare earth in the amorphous matrix and probably the amount of defects. The physical clustering reduction is evident by the important differences in the lifetime between the parent glass and the waveguide. Surely the increased quantity of silica play right but the deposition technique sounds very efficient.

- Last but not least you have found in this manuscript several pages related to the description of the techniques employed as well as several information of general interest for the research activity. I believe that this tutorial character is another important strength of my research. In fact, to perform this research multidisciplinary skills have been necessary and this is evident from the convergence of chemistry, optical spectroscopy, simulation and morphologic analysis to succeed in the fabrication of $P_2O_5$-based waveguides. I introduced detailed presentation of the different points referring to the more important papers available in the literature to give a solid base to my colleagues for the future work.

- Regarding this tutorial approach let me mention the chapter regarding stress and strain. In this chapter is presented a detailed description of the effect of fabrication protocol on the mechanical features of the devices. Several analysis techniques and modeling are discussed and specific calculation is performed in the case of silica hafnia system. I'm aware that could be considered a weakness of the research because the analysis was not performed on

phosphate systems due to lack of waveguides with high $P_2O_5$ content. However, the obtained results really fit with the sol-gel fabricated waveguides.

In conclusion the objective of this thesis has been to evaluate various methodologies for fabrication Phosphorous-based planar waveguides. In this context sol-gel and RF-sputtering techniques for planar waveguides fabrication has been investigated. RF-process has been optimized. In case of sol-gel technique a further thermodynamical study is required. Each of technique has drawbacks, in sol-gel method the principal question is related to the kinetics of the reaction, since it is too fast, to better control of the reaction rates, and better adjustment of the technological films fabrication, which effects on spectroscopic properties of the waveguiding systems: losses, refractive index. In case of RF-sputtering is noticeable that the refractive index is low, and the losses are less than 0.2 dB/cm, however the multicomponent target material increase the complexity of the structure.

It's evident that on the basis of the obtained results and collected information the key point for the sol-gel technique is to choice the correct $P_2O_5$ precursor. We have covered the first step of this long walk thanks to the study of different precursors. The immediate next step will be a detailed study of the kinetics of the sol gel solution. Another important issue to be completed concerns the thermal properties of the fabricated film and glasses and this is true both for sputtering and sol-gel. Another interesting point that we have to consider is the role of $P_2O_5$ and of $xP_2O_5$-$yHfO_2$ on the refractive index of a silica-based glass. This means that we should be able to fabricate the binary $SiO_2$-$P_2O_5$ system, surely a not trivial task with sol gel technology and asking for time consuming in the case of RF-sputtering.

My research was performed in the framework of several international projects (see below) and we are looking to prepare a proposal for the Photonics KET 2017. I have already mentioned in the introduction as phosphate glasses are crucial for the development of novel photonic devices especially for light confinement. The more important among them are planar waveguides, fibers and microresonators. All of them are inside our interest and when we will succeed in developing suitable coating fabrication protocols we will exploit the mechanical, structural and

optical properties of binary or ternary phosphate system to improve and tailor the features of the above mentioned photonic systems.

My research activity allowed me to interact with several colleagues with different skills also thanks to my involvement in the international projects:

- CNR-PAS joint project "Nanostructured systems in opal configuration for the development of photonic devices" (2014-2016)
- COST Action MP1401 "Advanced fibre laser and coherent source as tools for society, manufacturing and life science"
- Brazilian Scientific Mobility Program "Ciências sem Fronteiras"
- MAE "Smart optical nanostructures for green photonics" (2013–2015)
-

The following papers and communication are related to my research activity

## Publications

1. Chiappini, A.; Lukowiak, A.; **Vasilchenko**, I.; Ristic, D.; Normani, S.; Chiasera, A.; Boulard, B.; Dorosz, D.; Scotognella, F.; Vaccari, A.; Taccheo, S.; Pelli, S.; Nunzi Conti, G.; Ramponi, R.; Righini, G.C.; Gonçalves, R.R.; Abd Rahman, M.K.; Ferrari. M.
   "Glass-based Confined Structures Enabling Light Control", American Institute of Physics (AIP) Conference Proceeding, 1657 (2015), pp. 0300051-03000518

2. Dorosz, D.; Kochanowicz, M.; Zmojda, J.; Miluski, P.; Marciniak, M.; Chiasera, A.; Chiappini, A.; **Vasilchenko**, **I**.; Ferrari, M.; Righini, G.
   "Rare-Earth Doped Materials for Optical Waveguides", Invited paper Proceedings ICTON 2015, 17th International Conference on Transparent Optical Networks, Budapest, Hungary, July 5-9, (2015), pp.1-5

3. Lukowiak, A.; Chiappini, A.; Chiasera, A.; Ristic, D.; **Vasilchenko**, **I**.; Armellini, C.;Carpentiero, C.; Varas, S.; Speranza, G.; Taccheo, S.; Pelli, S.;

Battisha, I.K.; Righini, G.C.; Strek, W.; Ferrari, M. "Sol–gel-derived photonic structures handling erbium ions luminescence" Optical and Optical and Quantum Electronics, 47 (2015), pp.117-124

4. **Vasilchenko**, **I**.; Carpentiero, A.; Chiappini, A.; Chiasera, A.; Vaccari, A.; Łukowiak, A.; Righini, G.C.; Vereshagin, V.; Ferrari, M.
"Influence of phosphorous precursors on spectroscopic properties of $Er^{3+}$-activated $SiO_2$-$HfO_2$-$P_2O_5$ planar waveguides", Journal of Physics: Conference Series, 566 (2014), pp. 0120181-0120181

5. Chiappini, A.; Armellini, C.; Carpentiero, A.; **Vasilchenko**, **I**.; Lukowiak, A.; Ristić, D.; Varas, S.; Normani, S.; Mazzola, M.; Chiasera, A.
"Glass-based confined structures fabricated by sol-gel and radio frequency sputtering", Optical Engineering, 53 (2014), pp. 0718041-0718046

6. Chiappini, A.; Chiasera, A.; Armellini, C.; Carpentiero, A.; Lukowiak, A.; Mazzola, M.; Normani, S.; Ristic, D.; Valligatla, S.; **Vasilchenko**, **I**.; Varas, S.; Righini, G.C.; Ferrari, M. "Glass-based Photonic Crystals: from Fabrication to Applications", Advances in Science and Technology, Vol. 90 (2014), pp.121-126

7. Łukowiak, A.; **Vasilchenko**, **I**.; Normani, S.; Chiappini, A.; Chiasera, A.; Armellini, C.; Duverger, C.; Boulard, B.; Wiglusz, R.; Pelli, S.; Battisha, I.; Righini, G.; Marciniak, M.; Ferrari, M. "Glass-ceramics for photonics: advances and perspectives"
**Invited paper** Proceedings ICTON 2014, 16th International Conference on Transparent Optical Networks, Graz, Austria, July 6-10, (2014), pp. 1-4

8. Ristic, D.; Chiappini, A.; Chiasera, A.; **Vasilchenko**, **I**.; Armellini, C.; Lukowiak, A.; Carpentiero, A.; Mazzola, M.; Varas, S.; Nunzi Conti, G.; Pelli, S.; Speranza, G.; Ivanda, M.; Duverger Arfuso, C.; Ngoc, K.T.; Boulard, B.; Righini, G.C.; Ferrari, M.

"Glass-Based Sub-Wavelength Photonic Structures", Proceedings ICTON 2013 Invited paper 15th International Conference on Transparent Optical Networks Cartagena, Spain, June 23-27, (2013), pp.1-5

9. **Vasilchenko Y.O**. "Sol-gel process application for glass materials production"/ Conference Proceedings of XIII-th All-Russia scientific-practical conference of graduate students and students of "Chemistry and Chemical Engineering in the XXI century", Tomsk, Russia (2012), pp.312-314

**Communications**

1. **Vasilchenko, I.**; Valligatla, S.; Tran Thi Thanh, V.; Ristic, D.; Chiasera, A.; Goyes, C.; Boulard, B.; Dorosz, D.; Gonçalves, R.R.; Lukowiak, A.; Righini, C.G.; Ferrari, M. "Transparent glass-ceramics for photonics" **Invited lecture** at 7th International Symposium on Optical Materials (IS-OM7 2016) February 29th to March 4th 2016, Lyon, France

2. Goyes, C.; Valligatla, S.; Tran Thi Ngoc, L.; Meneghetti, M.; Armellini, C.; Varas, S.; Zur, L.; **Vasilchenko, I**.; Chiasera, A.; Gonçalves, R.R.; Lukowiak, A.; Boulard, B.; Righini, C.G.; Ferrari, M. "Glass-ceramics for photonics" Poster presentation at IFN Day, Roma, 21-22 January 2016

3. **Vasilchenko, I.** Welcomes the International Year of Light, poster presentation "Sol-gel fabrication of $Er^{3+}$- activated $SiO_2$-$HfO_2$-$P_2O_5$ planar waveguides", January 2015, Italy Presenting author

4. Lukowiak, A.; Armellini, C.; Chiappini, A.; Chiasera, A.; Valligatla, S.; **Vasilchenko**, **I**.; Gonçalves, R.R.;Strek, W.; Ferrari. M. "Sol-gel derived Photonic structures" , **Invited talk** XIV Brazilian MRS meeting, September 2015, Brazil

5. Lukowiak, A.; Chiappini, A.; Chiasera, A.; **Vasilchenko, I**.; Armellini, C.; Battisha, I.; Dorosz, D.; Righini, G.; Marciniak, M.; Strek, W.; Ferrari, M. "Sol–gel as a useful technique for fabrication of erbium-activated photonic structures" **Invited talk** at E-MRS 2014 Fall Meeting: Advances on functional doped glasses: technologies, properties and applications, September 15-19 (2014), Warsaw, Poland

6. Boulard, B.; Normani, S.; Łukowiak, A.; **Vasilchenko, I**.; Chiappini, A.; Chiasera, A.; Duverger, C.; Pelli, S.; Battisha, I.; Prudenzano, F.; Righini, G.; Marciniak, M.; Ferrari, M. "RED activated glass-ceramics: advances and perspectives in photonics", Oral communication at E-MRS 2014: Advances on functional doped glasses: technologies, properties and applications, September 15-19 (2014), Warsaw, Poland

7. Chiappini, A.; Chiasera, A.; Lukowiak, A.; Ristic, D.; **Vasilchenko, I**.; Boulard, B.; Duverger Arfuso, C.; Armellini, C.; Carpentiero, A.; Varas, S.; Normani, S.; Battisha, I.K.; Cibiel, G.; Righini, G.C.; Ferrari, M. "Photonic Glasses and Confined Structures", **Invited Lecture** at OFTA 2014, 15th Conference on Optical Fibers and Their Applications, January-February (2014), Białystok – Lipowy Most, Poland

8. Chiappini, A.; Chiasera, A.; Armellini, C.; Carpentiero, A.; Lukoviak, A.; Mazzola, M.; Normani, S.; Ristic, D.; Valligatla, S.; **Vasilchenko, I**.; Varas, S.; Righini, G.C.; Ferrari, M. "Glass-based Photonic Crystals: from Fabrication to Applications", Oral communication at 13th International Ceramic Congress CIMTEC 2014 Symposium CL - Inorganic Materials Systems for Optical and Photonics Applications June 8-13 (2014), Montecatini Terme, Italy

9. **Vasilchenko**, **I**.; Carpentiero, A.; Chiappini, A.; Chiasera, A.; Vaccari, A.; Lukowiak, A.; Righini, G.C.; Vereshagin, V.; Ferrari. M. "Influence of phosphorous precursors on spectroscopic properties of $Er^{3+}$-activated $SiO_2$-$HfO_2$-$P_2O_5$ planar waveguides", Oral communication at 5th Young Researcher Meeting, July 2014, Trieste Presenting author

10. Boulard, B.; Normani, S.; Łukowiak, A.; **Vasilchenko**, **I**.; Chiappini, A.; Chiasera, A.; Duverger, C.; Pelli, S.; Battisha, I.; Prudenzano, F.; Righini, G.; Marciniak, Ferrari, M. "RED activated glass-ceramics: advances and perspectives in photonics", Oral communication at E-MRS 2014 Fall Meeting, Symposium FALL 14 P: Advances on functional doped glasses: technologies, properties and applications, September 15-19 (2014), Warsaw University of Technology, Poland

11. **Vasilchenko**, **I**.; Normani, S.; Piotrowska, A.; Chiappini, A.; Chiasera, A.; Lukowiak, A.; Ristic, D.; Armellini, C.; Mazzola, M.; Carpentiero, A.; Varas, S.; Zonta, D.; Marciniak, M.; Righini, G.C.; Gonçalves, R.R.; Ferrari, M. "Photonic Glasses and Confined Structures", **Invited talk** at Annual Meeting of the Brazilian Materials Research Society (B-MRS), Symposium "Sol-Gel Materials: From Fundamentals to Advanced Applications" Sept 28th to Oct 2nd 2014 João Pessoa, Paraíba State, Brazil

12. **Vasilchenko**, **I**.; Normani, S.; Piotrowska, A.; Chiappini, A.; Chiasera, A.; Lukowiak, A.; Ristic, D.; Armellini, C.; Carpentiero, A.; Varas, S.; Zonta, D.; Marciniak, M.; Pelli, S.; Nunzi Conti, G.; Righini, G.C.; Gonçalves, R.R.; Ferrari, M. "Photonic Glasses and Confined Structures", **Invited lecture** at 3rd International Workshop on Fundamentals of Light-Matter Interaction, October 05-08, 2014, Recife Brazil

13. Chiappini, A.; Łukowiak, A.; **Vasilchenko**, **I**.; Ristic, D.; Normani, S.; Chiasera, A.; Boulard, B.; Dorosz, D.; Righini, G.C.; Abd Rahman, M.K.; Ferrari, M. "Glass-based confined structures enabling light control", **Invited talk** at PERFIK-2014 National Physics Conference 2014, , 18-19 November 2014, Kuala Lumpur, Malaysia

14. Lukowiak, A.; Chiappini, A.; Chiasera, A.; Ristic, D.; **Vasilchenko**, **I**.; Armellini, C.; Carpentiero, A.; Varas, S.; Speranza, G.; Taccheo, S.; Pelli, S.; Battisha, I.K.; Righini, G.C.; Strek, W.; Ferrari, M. "Sol–gel-derived photonic structures", Guest Lecture IP2013 Information Photonics 2013 Conference, 16-19 September 2013, Warsaw, Poland